UPPER AND LOWER BAKKEN SHALE PRODUCTION CONTRIBUTION TO THE MIDDLE BAKKEN RESERVOIR

by

Sanyog Kumar

A thesis submitted to the Faculty and the Board of Trustees of the Colorado School of Mines in partial fulfillment of the requirements for the degree of Master of Science (Petroleum Engineering).

Golden, Colorado

Date: _____

Signed: _____
Sanyog Kumar

Approved: _____
Dr. Todd B. Hoffman
Thesis Advisor

Golden, Colorado

Date: _____

Signed: _____
Dr. William Fleckenstein
Professor and Head
Department of Petroleum Engineering

ABSTRACT

There is an uncertainty over the Upper and Lower (U&L) Bakken Shale production contribution to the Middle Bakken reservoir. For the Bakken system, a reliable degree of accuracy in the reservoir studies involving the fluid flow and recovery mechanism cannot be achieved without resolving this uncertainty. Performance anomalies in the gas-oil ratio (GOR) trends of the production history of the Middle Bakken wells in the Reunion Bay, Sanish, Parshall and the Elkhorn Ranch fields indicate the possibility of the anticipated contribution.

Quantifying the U&L Shale contribution requires knowledge of the mechanism of fluid storage and flow in the liquid rich shale systems. For the U&L Shale, adsorption is considered as the primary mode of fluid storage, and the process of diffusion is considered crucial for the matrix-to-fracture fluid transfer. The governing mathematical equations for desorption and diffusion was adopted for shale gas systems. These equations are incorporated in Computer Modeling Group's (CMG™) compositional simulator GEM™ to propose a reservoir simulation-based quantification scheme for the U&L Shale contribution.

Through the sensitivity analyses, the effect of variation in the parameters of the U&L Shale, the Middle Bakken layer and the hydraulic fracture is investigated. Utilizing the surveyed numerical value-ranges of these parameters, the U&L Shale layers are found to contribute in the range of 12 to 52% of the cumulative production from a Middle Bakken well. Whereas, utilizing the mean numerical values of the parameters, the contribution is quantified as 40%. Relative sensitivity study suggested that the U&L Shale production contribution is the most sensitive to the U&L Shale matrix parameters, such as total organic carbon (TOC, wt.%) and molecular diffusion coefficients. The TOC controls the desorption-parameters; therefore, the findings suggest that the phenomena of desorption and diffusion are expected to play a crucial role in the anticipated production-contribution.

TABLE OF CONTENTS

LIST OF FIGURES

LIST OF TABLES

ACKNOWLEDGEMENTS

First, I would like to express gratitude to my thesis advisor Dr. Todd B. Hoffman for his great support, motivation and guidance. He is owed my special thanks for sponsoring and funding this MS program. I extend my sincere thanks to my committee members Dr. Steve Sonnenberg, Dr. Hossein Kazemi and Dr. Manika Prasad for their invaluable time, input and comments.

I thank my temporary MS advisor Dr. Erdal Ozkan, for supporting me in securing admission in the MS program and guiding me during the first semester.

In addition, I deeply appreciate contributions from following people to make this thesis complete:

- My wife Dipanwita Nandy for her constant support and valuable suggestions throughout my involvement in this project.
- My parents for being a constant source of motivation and setting an example of perseverance for me.
- Denise Winn-Bower (Program Assistant in Petroleum Engineering Department) for graduate program guidance, including scheduling and planning to meet the thesis timeline.

Finally, Thanks to all faculty, staff and friends for their great education, support and assistance during my academic program.

To my Father

CHAPTER 1

INTRODUCTION

1.1 Bakken Resource Play

The Bakken Formation lies within the oil-window of the vast Williston Basin, which extends over the regions of North Dakota, Montana and the Canadian province of Saskatchewan (Figure 1.1). While, the actual quantity of recoverable oil in the Bakken is an issue of debate, the U.S Geological Survey estimated that the mean technologically recoverable reserve to be 3.65 billion barrel of oil, 1.85 TCF of dissolved natural gas, and 148 million barrel of natural gas liquids (Figure 1.2). These staggering reserve figures have elevated Bakken's stature as a leading petroleum system, and today it is ranked as the biggest oil accumulation in the Lower 48 states of the US.

The production history of the Bakken wells in Figure 1.3 suggests that before year 2000, most Bakken wells provided marginal economic success, partially because of extremely low matrix permeability (0.0001-.01 md) and meager chances of exploiting the many localized natural fractures with a vertical well. Commercial production and development activities have become increasingly economically viable in recent years with the advances in horizontal drilling and the use of multi-stage fracture stimulation. Year 2000 witnessed a remarkable turnaround for the Bakken play when oil was successfully produced from the Middle Bakken reservoir of the Elm Coulee Field in Montana. Buoyed by the success, many additional areas were also evaluated, especially in the North Dakota extensions of the play, and the real breakthrough came with the landmark discovery of Parshall Field in year 2006. Chart in Figure 1.3 depicts the comprehensive development activity in North Dakota after the discovery of Parshall Field in 2006, which has resulted into an exponential increase in daily oil production. In the month of March 2013, the North Dakota Bakken play produced with an average daily rate of 0.71 million BOPD and 681 MMSCF of gas per day.

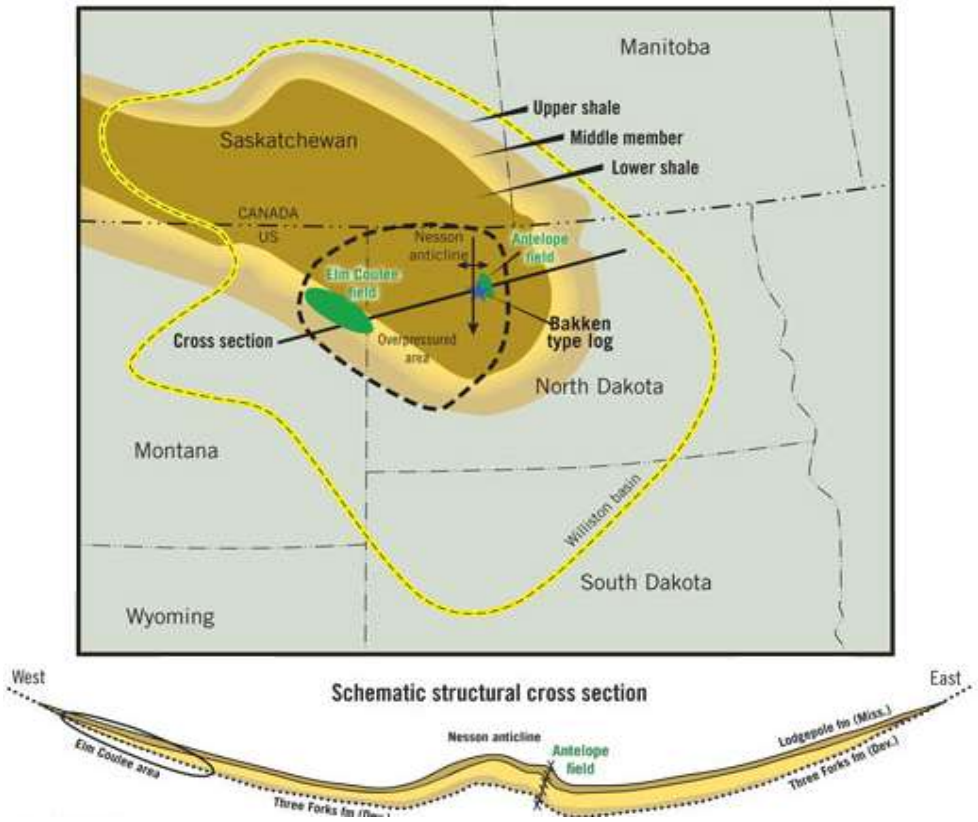

Figure 1.1: The geographical extent and location of the Williston Basin and the Bakken formation (USGS 2008).

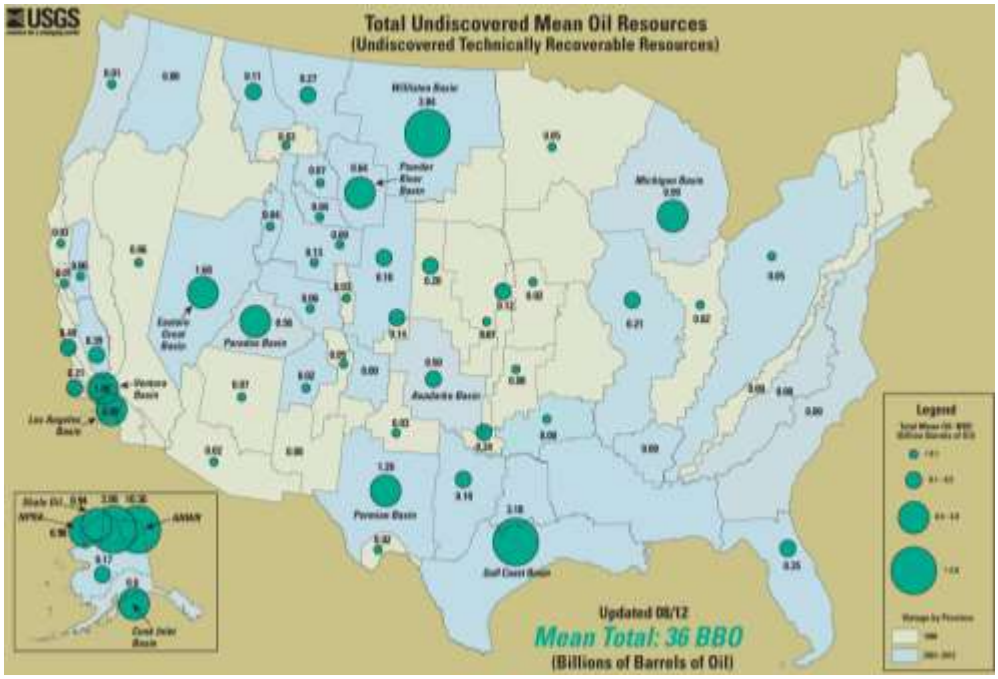

Figure 1.2: Bubble map plotting leading oil accumulation in US (USGS 2012).

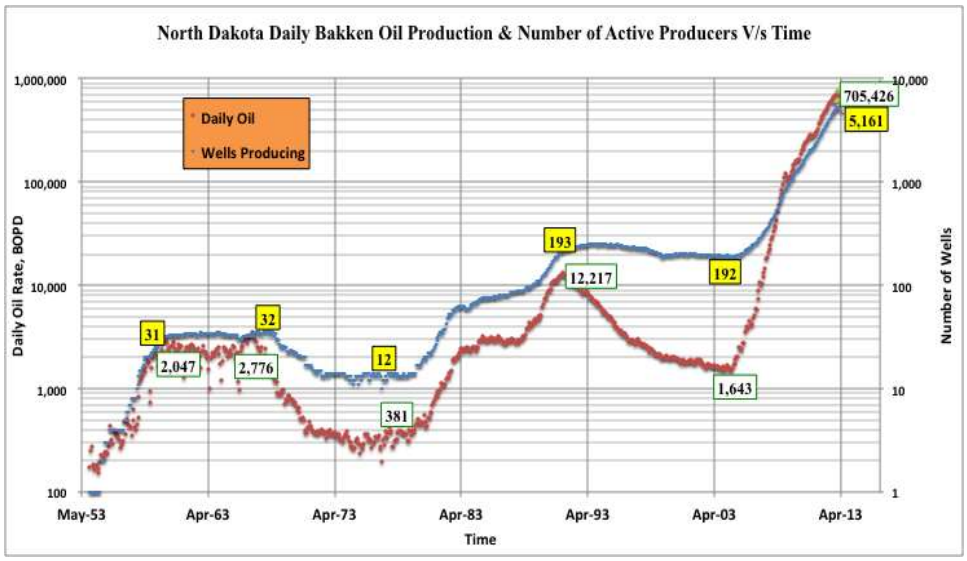

Figure 1.3: Chart showing historical daily oil production rate and number of active producing wells producing from Bakken, Sanish, Three Forks, and Bakken/Three Forks pools.

In the current surge of unconventional shale plays, the tight Bakken play is commonly referred to as shale, but it has a dolomitic siltstone lithology. The Bakken Formation is divided into three main members: 1) Upper organic-rich black shale, 2) Middle silty dolostone to fine-grained sandstone, and 3) Lower organic-rich black shale. The U&L organic-rich shale members are believed to be the source rock, which have expelled oil into the low-porosity and low-permeability Middle Bakken member. The tight Middle Bakken reservoir with extensive horizontal drilling operations is the focus of the current production and development activities. The horizontal laterals are drilled to multi-mile length and stimulated using multistage hydraulic fracturing, thus ensuring a better reservoir connection and interlinking of the naturally existing localized fractures (Figure 1.4).

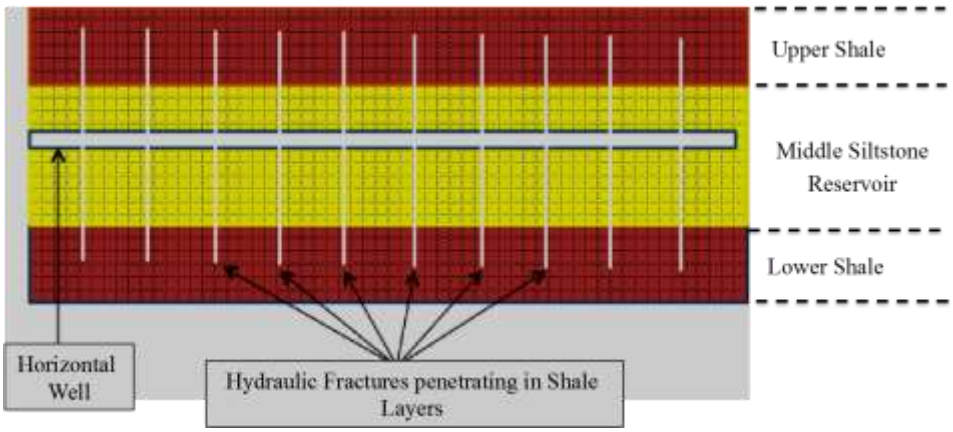

Figure 1.4: A schematic representation of the current completion strategy for Bakken.

1.2 Project Objectives

The project is aimed at addressing the basic, but critical, issue of the U&L Shale's production contribution to the Middle Bakken reservoir. The following three main steps summarize the aim of this research:

1) Understanding the mechanism: How does the proposed contribution take place?
2) Fact-finding: Does the Middle Bakken reservoir get production contribution from the U&L Shale? If it does so, then;
3) Quantifying the contribution using reservoir simulation: How much do they contribute?

In the first step of the project, existing literature on the physical phenomena, which are considered crucial for this project, were reviewed. The next stage involved finding the evidence and clues, which would indicate the proposed U&L Shale contribution. The production history of the wells should reflect this contribution in forms of a certain signature or anomaly. In the final step of the project, quantification of the proposed contribution was performed through a proposed simulation-scheme.

1.3 Advantages of project findings

The project findings improve the existing understanding of the Bakken reservoir system in the following contexts:

- **Recovery mechanism:** The contribution from the U&L Shale would require a significant overhaul of the present understanding of the recovery mechanism for the Middle Bakken reservoir. The project proposes a possible mechanism through which the U&L Bakken shale layers might contribute to the Middle Bakken production.

- **Factors affecting the U&L Shale contribution:** Through the parametric-sensitivity analysis on the proposed simulation scheme for the Bakken system, the factors affecting recovery would be investigated. It will help in designing an optimum completion as well as in identifying a suitable drilling location.

1.4 Organization of the Thesis

Chapter 1 briefly introduces the Bakken resources play and the objective of the research.

Chapter 2 is about the literature review and background research on the physical phenomena, which would be pivotal in explaining the mechanism through which the U&L Shale might be contributing.

Chapter 3 covers the second step of the project to investigate the evidences and clues indicating the proposed U&L Shale production contribution.

Chapter 4 covers the proposed quantification scheme for the U&L Shale production contribution. Reservoir simulation on CMG's GEM module was used for the quantitative prediction in this project. This chapter also elaborates on the modeling aspects for the discussed physical phenomenon in Chapter-2.

Chapter 5 covers the findings and results of this work in terms of the parametric-sensitivity analysis on the proposed quantification scheme. The chapter further ponders on the physical interpretations and explanations for the derived results.

Chapter 6 finally concludes this work and suggests the scope of further improvement with some potential future areas of study.

CHAPTER 2

LITERATURE REVIEW

This chapter provides an overview of the physical phenomena, which were considered crucial in explaining the mechanism through which the U&L Shale layers might be contributing in the production of the Middle Bakken reservoir. The previous work on the following core concepts will be reviewed in the subsequent sections of this chapter:

1. Pore-scale fluid storage and fluid flow in shale
2. Dual porosity media in the Bakken
3. Molecular desorption: Langmuir isotherm
4. Desorption in liquid-bulk
5. Langmuir parameters from Total Organic Carbon (TOC, weight %)

2.1 Pore Scale Fluid Storage and Fluid Flow in Shale

Unconventional organic rich shale (ORS) reservoirs are often referred to as self-resourcing shale (SRS). SRSs are those source-rocks in which the generated hydrocarbon somehow got trapped and could not migrate. The physics of fluid flow and storage in SRS is radically different from that in conventional sandstone or carbonate reservoir. SRS as a reservoir rock is usually affected by its pore-size distribution and pore-types. Pore size distribution is widely studied in the laboratory using mercury intrusion or by an NMR study. For the pore-types, Loucks et al. (2009) suggested that there could be three main types of matrix-related pores in the shale (Figure 2.1): 1) Interparticle (interP) mineral pores, 2) intraparticle (intraP) mineral pores, and 3) intraP organic-matter (OM) pores.

2.1.1 Fluid Storage in Self Resourcing Shale

Not much contribution on the mechanism of fluid storage in liquid rich SRS could be found in the literature. Its analogy to gas SRS may be rudimentary, but at this juncture it could prove to be a good starting point. Ambrose, et al. (2010) proposed a comprehensive gas storage

scheme for SRS. The author suggested four gas storage components: free gas, adsorbed gas, solution gas dissolved in oil and solution gas dissolved in water were suggested. Swami and Settari (2012) considered dissolved or sorbed gas in the kerogen-bulk to be significant and added a new component for it.

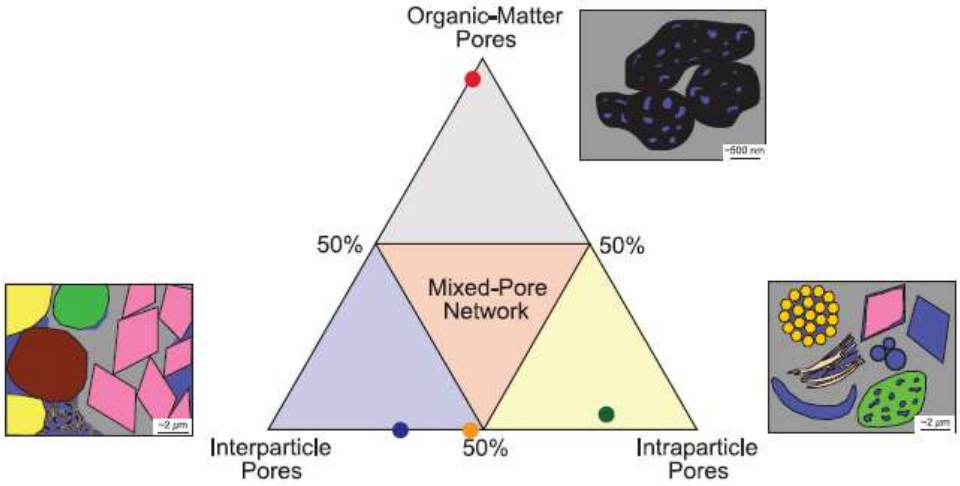

Figure 2.1: Matrix Pore components in Shale and Mudstone (Loucks, et al. 2009).

This research uses the term 'fluid' instead of 'gases in the context of SRS, because the liquid-gas phase distinction might lose its essence in the nanopores (which will be discussed to have dimensions comparable to those of gas or liquid molecules). With that, the number of Ambrose's storage components could be reduced to two, namely: free fluid and adsorbed-fluid. However, there could be a third component to it as well, dissolved or sorbed fluid in kerogen-bulk, as suggested by Swami and Settari (2012).

Wang, et al. (2009) rated OM pores of SRS as its characteristic feature, which differentiates it from the other ordinary non-productive shales. It was suggested that the OM pores of the SRS could have an exceptionally large storage capacity, which might be up to five times greater than the non-organic matrix pores. It was also cited that most of the adsorption-sites and the OM pores resided within the kerogen (matured organic content). It could be noted here that the hydrocarbon fluid can be stored in both adsorbed and free states in the 5-100nm sized OM nanopores, which might often rival the size of some of the stored hydrocarbon molecules.

Loucks, et al. (2012) suggested that the OM pore originates from the process of thermal maturation of the buried organic matter. It was assumed that the voids in the matured organic matter or kerogen were associated with the hydrocarbon generation and migration. The SRS serves as both source and reservoir rock, and their generated hydrocarbons were assumed to occupy the OM pores. The authors also suggest that the OM pores could make up to 40% of the total intraparticle porosity within the kerogen, and they might have irregular, bubble-like, elliptical cross-section. While, these pores might appear isolated in a two-dimensional SEM picture (Figure 2.2), they were actually interconnected when viewed in the three-dimensional view. It was also cited that not all the kerogens are equally capable of generating OM porosity. The type II kerogen might be more prone to the development of OM pores than the type III kerogen. Bakken shale organic matter consists of type II and type I kerogens, so the expectation of finding OM pores should be fairly high there.

Most notably, the nanopores of SRS would expose its fluid to an extremely large interactive pore-surface area, in comparison to the macro-pores of conventional reservoirs. Therefore, for SRS, fluid storage may be dominated by the interaction between pore-surface and individual fluid molecule.

2.1.2 Fluid Transfer in SRS

The physics of fluid transportation in the liquid rich SRS is not well understood. As mentioned earlier, the gas-liquid phase distinction might lose its essence in the nanopores and the molecular flow might be the dominating flow mechanism (Figure 2.3). Limited analogies for fluid flow can be drawn to the liquid SRS from its gas counterpart, for which different fluid transportation mechanism has been comprehensively studied. Most studies modified the Darcy equation to include the contribution of the molecular-flow through the pores of SRS. The Klinkenberg slippage effect (Klinkenberg, 1941) was included in Ertekin, et al. (1986). Ozkan, et al. (2010) proposed a concentration-difference-driven diffusive-flow component. Javadpour (2009) derived an expression based on the theoretical parameters in which he considers both slippage and Knudsen diffusion in nanopores. Swami and Settari (2012) suggested inclusion of flow contributed by diffusion of gases dissolved or sorbed in kerogen (Figure 2.4).

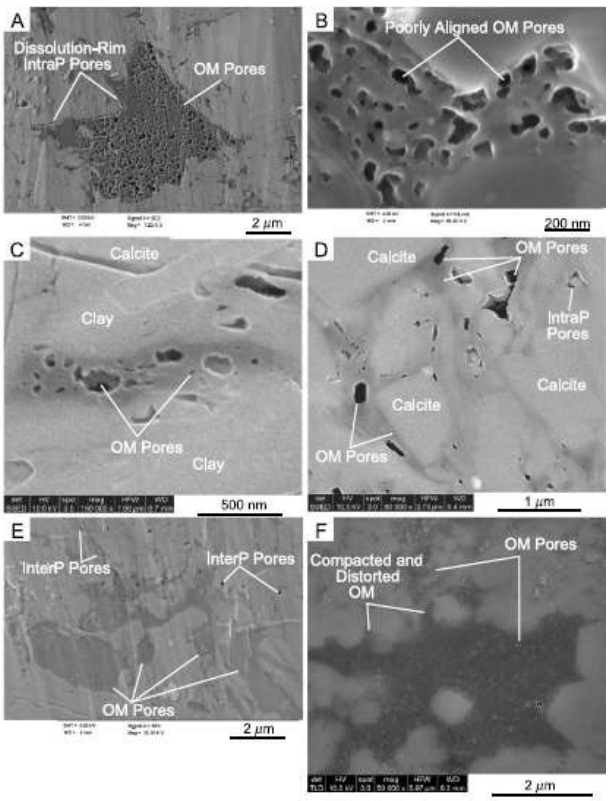

Figure 2.2: OM Pores in Shale as seen from a scanning electron microscope (Loucks, et al. 2009).

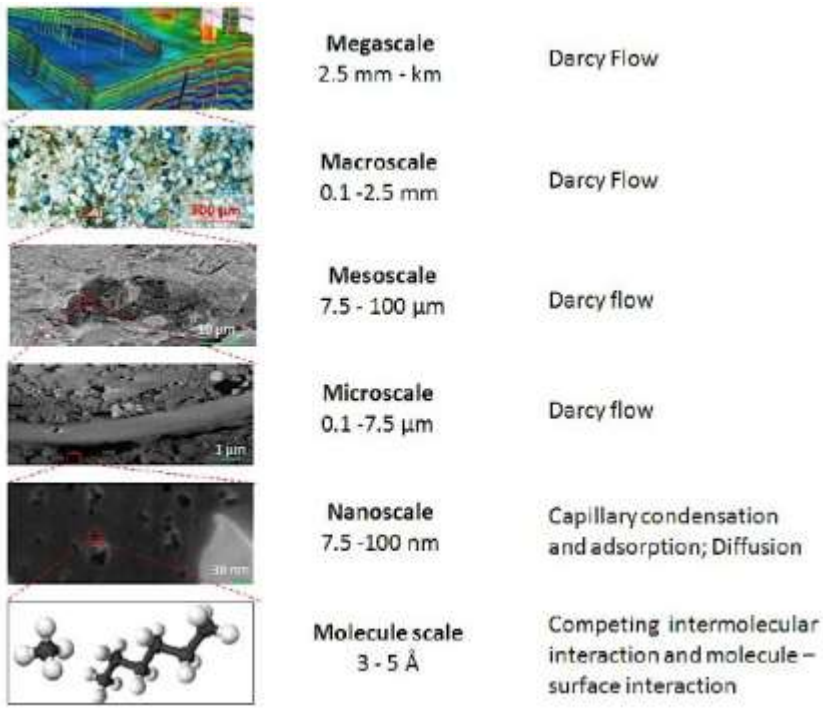

Figure 2.3: Various pore-size and associated physics for fluid storage and transportation (Chen, et al. 2012).

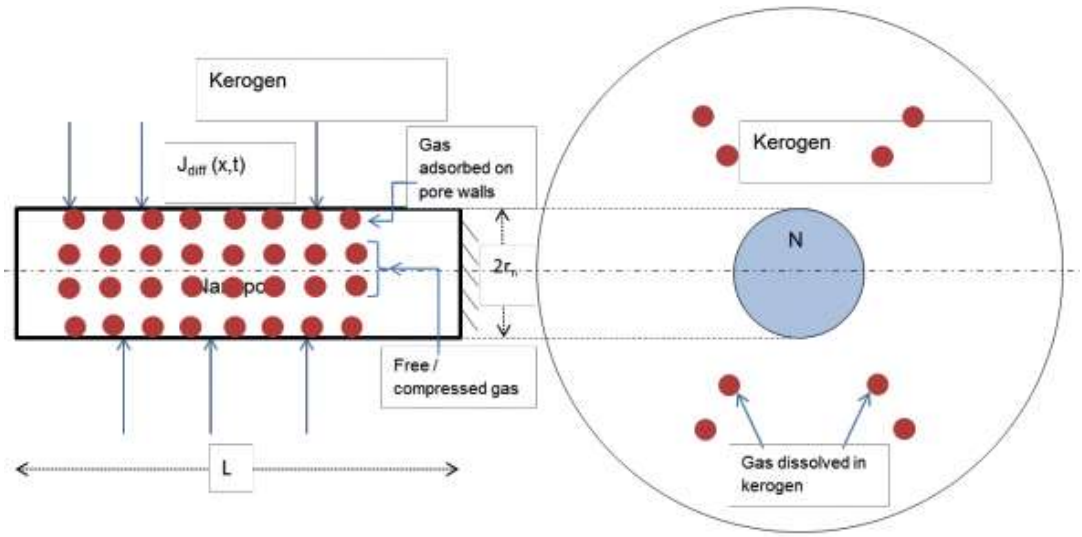

Figure 2.4: Schematic diagram showing components of gas flow at pores-scale (Swami and Settari, 2012).

2.2 Dual-porosity media in the Bakken

The following three criteria need to be fulfilled to justify dual-porosity media in a given reservoir:

- Fluid storage in the matrix
- Mechanism for matrix-to-fracture fluid transfer
- Interconnected fracture-network

The possibility of having a dual-porosity flow media in the three layers of the Bakken is investigated below:

2.2.1 U&L Shale Dual-porosity Media

Organic richness of the U&L Bakken Shale has been reported and quantified by much research in the past. Schmoker and Hester (1983) reported 6-20 Wt% TOC for 59 U&L Bakken sample from 39 wells in North Dakota. So, the shale layers must be rich in OM pores to provide plenty of active adsorption-sites in the shale matrix. As discussed in the previous section, OM pores' adsorption-sites are the most crucial fluid storage component of SRS. Thus, the U&L Bakken shale can be concluded to have plenty of fluid storage capacity in their matrix.

Nanopores of the shale could inhibit a Darcy kind of fluid flow; therefore diffusion might be the exclusive mode of fluid transfer for the desorped molecules from the matrix to fractures.

Meissner (1978) associated the oil generation and migration in the U&L Shale to the abnormal pressure gradients, which may be as high as 0.73 psi/ft (Figure 2.5) in Antelope Field. This abnormal pressure regime might be responsible for the frequent occurrence of the natural macro-fractures and micro-fracture in the U&L Shale Layers. Moreover, in this project it was assumed that the hydraulic fractures penetrate all of the three Bakken layers. For the U&L Bakken Shale, the natural macro-fractures and micro-fractures combined with the hydraulic fractures form the fracture-network for the assumed dual-porosity media.

2.2.2 Middle Bakken Dual-porosity Media

The Middle Bakken layer is essentially a tight dolomitic siltstone. Most of the oil in this layer resides within the pores of natural fractures and the associated micro-fracture, with a minimum contribution reported from its tight matrix (Pitman, et al. 2003). It was assumed that these natural micro-fractures would act like the matrix-porosity of the dual-porosity media. The hydraulic fractures and the natural macro-fractures act together as the fracture network to complete the Middle Bakken reservoir as a dual-porosity flow media. The matrix-to-fracture fluid transfer was considered to follow the principles of conventional advective or Darcy flow.

The presence of naturally existing fractures is a widely accepted fact for the Bakken formation. The extremely low matrix permeability of the Middle Bakken matrix also suggests that other porosity and permeability enhancing mechanisms, such as the natural fractures, are present to allow for oil migration. Pitman, et al. (2003) analyzed and described the importance of detrital mineralogy and the diagenetic alterations for secondary and fracture porosity in the Middle Bakken layer. It was also noted that the fractures were present throughout the Bakken formation at macroscopic as well as microscopic scale. The majority of fractures were suggested to be horizontal, open (non-mineralized) and discontinuous with aperture widths commonly exceeding 30 microns (Pitman, et al. 2003).

2.3 Single Component Desorption

Desorption of fluid from the OM pores and its subsequent transfer from the matrix-to-fracture must be included in flow calculations. For that, a mathematical scheme is required to characterize the desorption process. The Langmuir isotherm is one such scheme which has extensively been used to characterize a variety of processes involving molecular desorption.

Langmuir's approach might not be accurate, but it is robust and simple to model, which explains its variety of applications in reservoir engineering related studies of SRS. For a single component desorption case, it can be represented mathematically with the equation 2.1.

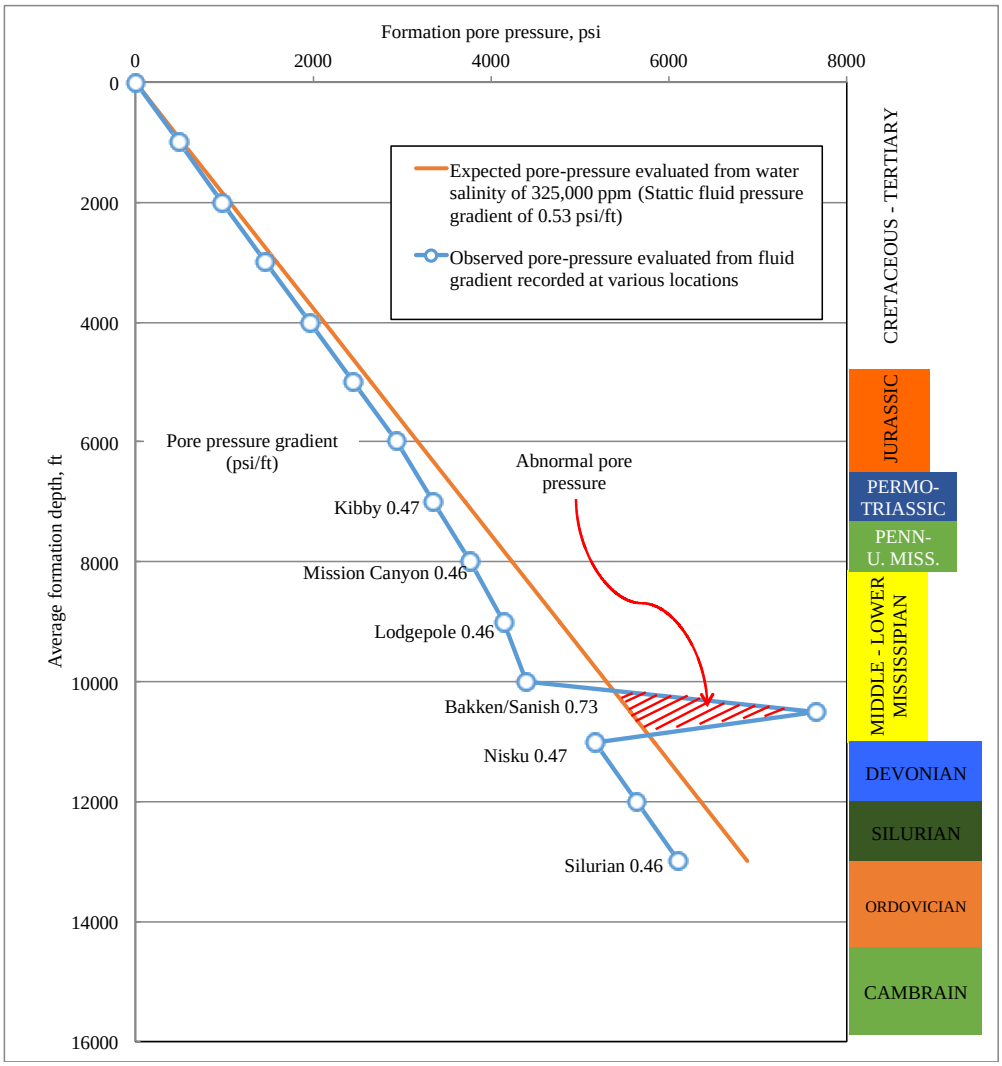

Figure 2.5: Formation pressure gradients of the Bakken and adjacent formations (Modified from Meissner, 1978).

$$\left[V_p = V_{max} * KP/(1 + KP)\right]_{T=constant} \quad (2.1)$$

The two parameters V_{max} and K in the above equation are generally referred to as the adsorption-capacity in$(SCF\,of\,gas/ton)$, and the Langmuir-constant in $(1/psi)$ respectively. V_p is the adsorped volume in $(SCF\,of\,gas/ton)$ corresponding to an ambient pressure (P). It could be noted that the knowledge of the two parameter are sufficient to include desorption in a mathematical formulation.

The processes that use the Langmuir formulation must assume instantaneous equilibrium between the sorptive surface and desorped free-gas. From a modeling perspective, it means that there is no transient time lag between the pressure-drop and the desorption-response. Gao, et al. (1994) suggested that flow through the nano-sized OM pores of tight shale-matrix to be too slow to disturb the equilibrium between the adsorptive kerogen surface and the desorped free gas in the pores.

The following equation shows another mathematical form of the Langmuir isotherm:

$$V_P = pV_L/(p + p_L) \tag{2.2}$$

Thus, desorption isotherms as proposed by Langmuir are characterized in equation 2.2 by the V_L and P_L terms. While V_L is the total storage at infinite pressure, and P_L is the pressure at which half of the volume V_L is adsorped.

The two schemes are essentially the same and can be rearranged into another from by elementary algebra, which follows:

$$V_P = {pV_L}/{p + p_L} = ({p}/{p_L})V_L/\{({p}/{p_L}) + 1\} = V_L\, p({1}/{p_L})/1 + p({1}/{p_L}) \tag{2.3}$$

Therefore, $V_L = V_{max}$ and ${1}/{p_L} = K$ in equation 2.1

Also, at $p = p_L$:

$$V_P = pV_L/(p + p_L) = p_L V_L/(p_L + p_L) = p_L V_L/2p_L = V_L/2 \tag{2.4}$$

2.4 Multi-component Desorption

The U&L Bakken Shale layers are expected to have multi-component desorption scenario. Therefore, the single-component formulation discussed in the previous section must be extended to a multicomponent case before it could be used in this research. The following multicomponent Langmuir formulation could serve as an extended empirical means to model the multi-component desorption (Arri, et al. 1992):

$$G_i = V_{L,i}K_i py_i/\left(1 + \sum_j K_j py_j\right) \tag{2.5}$$

Where i is the component-index, $V_{L,i}$, b_i and y_i are the adsorption capacity (SCF of gas/ton), Langmuir-constant (1/psi) and the mole-fraction for the i^{th} component. In a pressure transient analysis application, Freeman, et al. (2012) used the multicomponent desorption data listed in Table 2.1, which is represented as the isotherm-curves in Figure 2.6. It could be noted that among all the other hydrocarbons, methane has the highest adsorption capacity. It appears that the adsorption capacity is inversely proportional to the size of the hydrocarbon-molecules.

Table 2.1: An example of Multi-component adsorption Langmuir Parameter (Freeman, et al. 2012)

Component	Y_i,	b_i, 1/psi	V_{Li}, scf/ton
Methane	0.80	2.08×10^{-6}	3.45×10^{4}
Ethane	0.07	2.11×10^{-4}	3.88×10^{2}
Propane	0.05	7.02×10^{-4}	1.9×10^{2}
Butane	0.05	3.84×10^{-4}	2.5×10^{2}
Pentane	0.02	8.10×10^{-5}	3.1×10^{2}
Hexane	0.01	1.21×10^{-5}	3.71×10^{2}

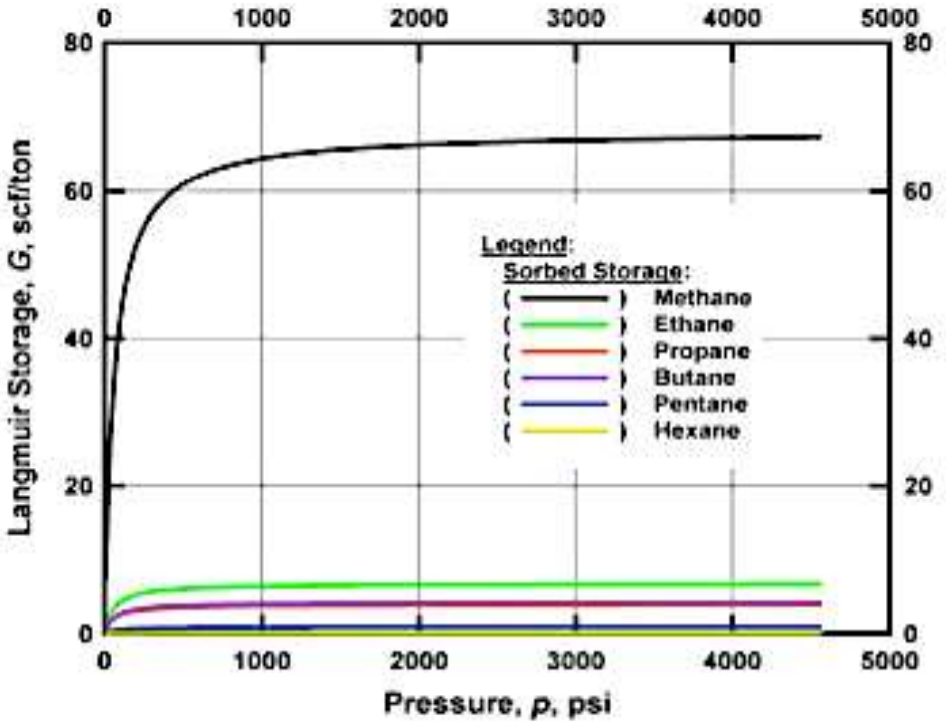

Figure 2.6: An example of Langmuir multi-component adsorption curve with the given parameters in the Table 2.1 (Freeman, et al. 2012).

2.5 Desorption in Liquid-bulk

As discussed in the previous section, phenomenon of adsorption is considered as a significant mode of fluid storage in the SRS, and U&L Shale should not be exceptions. Characterizing desorption and deriving a mathematical model for it is essential in this research. Desorption isotherms have been derived in the laboratory for many gas SRS systems, as it has diverse applications including in the flow calculations. However, these laboratory experiments explicitly pertain to the gas-desorption in the gas-bulk, and no work or data could be found in the literature for desorption taking place in liquid rich SRS such as Bakken or Niobrara.

By drawing analogies from the gas molecule desorption in gas-bulk, this research proposes a new schematic explanation to the phenomenon of molecular desorption taking place in the oil (liquid) bulk. The scheme would assume that there exists a gas buffer zone between the adsorptive-site (kerogen-surface) and the liquid continuum. The kerogen surface is thought to be desorping the molecules in this gas buffer zone. Now, depending upon the PVT conditions, these desorped molecules in the gas buffer zone either dissolve into the liquid continuum or they continue to exist as a separate gaseous-phase (Figure 2.7). While this scheme may or may not accurately represent the physics of the process, this scheme allows modeling the process in liquid-rich SRS.

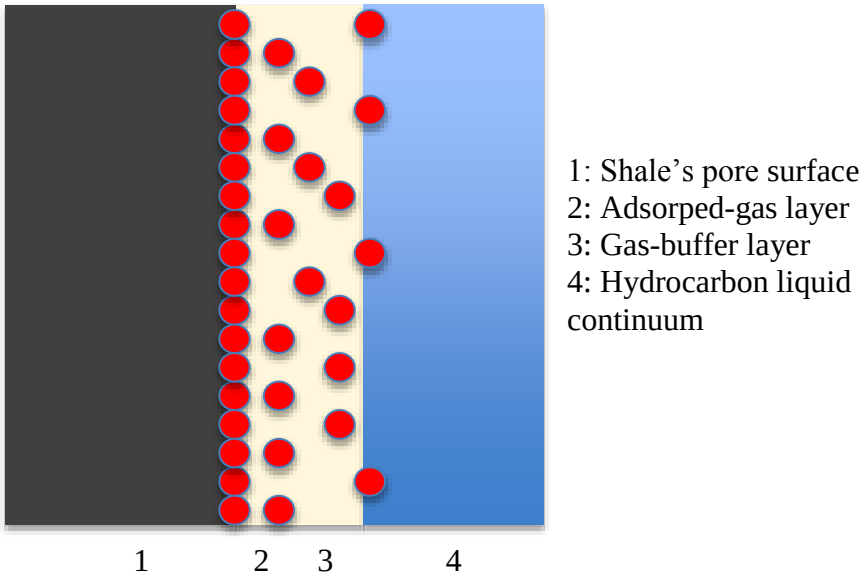

Figure 2.7: Scheme for desorption taking place in liquid-bulk.

2.6 Langmuir parameters from TOC

Laboratory experiments are the standard procedure to generate Langmuir isotherm or alternatively, empirical relationships can also be used to generate them. The adsorption capacity of a porous-media is known to be directly proportional to the active surface-area offered by the shale matrix-contents. Dehydrated kerogen, owing to their hydrophilic nature, is considered favorable to bond with hydrocarbon molecules. Therefore, the TOC concentration in the SRS is thought to be directly affecting its adsorption capacity. Lewis, et al. (2004) discussed the evaluation of the two Langmuir parameters (V_{max} and K) from TOC using empirical relationships--originally developed for CBM applications.

Kerogen type of the organic-content of SRS has also been found to affect its adsorption capacity. Zhang et al. (2012) conducted an extensive study to investigate the effect of organic-matter (OM) type and thermal maturity on their adsorption capacity for methane. For the study, multiple adsorption experiments were conducted on a wide variety of kerogen and shale oil samples. Langmuir isotherms generated from the experiments were in turn used to derive empirical relationships between temperature and K, and between TOC and V_{max} for different kerogen types. For this project, the following steps were followed to generate Langmuir-parameters:

1. Kerogen types at its maturity affects the Langmuir's constant K. The formulae for K for different kerogen types are as follows (Zhang et al., 2012):
   - For type I kerogen:

$$\ln\left({}^{\mathrm{K}}/_{145.5}\right) = \left({}^{1241}/_{\mathrm{T}} - 5.89\right) \tag{2.6}$$

   - For type II kerogen, $\mathrm{R_o} < 1.41$:

$$\ln(\mathrm{K}) = {}^{2628}/_{\mathrm{T}} - 9.75 \tag{2.7}$$

   - For type II kerogen, $\mathrm{R_o} > 1.41$ and type III kerogen:

$$\ln(\mathrm{K}) = {}^{3366}/_{\mathrm{T}} - 11.06 \tag{2.8}$$

   Where, T (in °Kelvin) is isotherm-temperature and R_o is the Vitrinite reflectance.

2. The Bakken OM is a mix of type-I and type II kerogen and the Vitrinite-reflectance is often found to be below 1.0 (Price, 1984). So, equations 2.4 and 2.5 should be used to determine the Langmuir's constant K.
3. Zhang et al. (2012) proposed the following general equation for V_{max} determination by regressing the available V_{max} versus TOC (weight %) data points (Figure 2.8):

$$V_{max} = 724 \times (0.0134 \times TOC + 0.0148); \text{in SCF/ton} \quad (2.9)$$

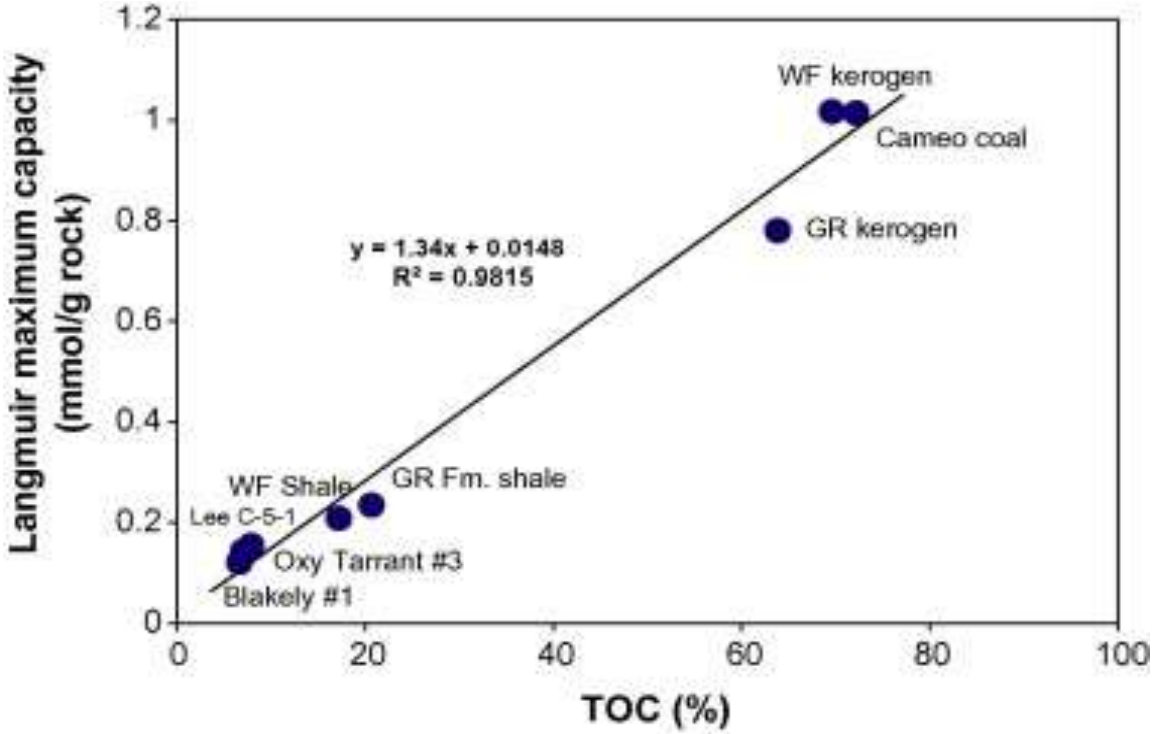

Figure 2.8: Regression line-fitting to deduce a general formula for adsorption capacity of methane as a function of Total Organic Carbon (Zhang, et al. 2012).

4. V_{max} is determined at a specific temperature (65°C). Correlation from Lewis, et al. (2004) work was used to complete this evaluation by extrapolating these parameters to the Bakken reservoir-temperature of 115 °C. The following equations, originally developed for coal-bed-methane reservoirs, represent the correlation used by Lewis, et al. 2004:

$$V_{LT} = 10^{(-c3 \cdot T + c4)} \quad (2.10)$$

$$P_{LT} = 10^{(-c7 \cdot T + c8)} \quad (2.11)$$

$$c4 = \log V_L + (c3 \cdot T_i) \quad (2.12)$$

$$c8 = \log P_L + (c7 \cdot T_i) \quad (2.13)$$

Where,

T_i = Isotherm temperature (in °C, laboratory conditions)

V_L = Adsorption capacity at , T_i, Equation 2.2

P_L = Langmuir's constant at , T_i, Equation 2.2

T = Reservoir temperature in °C

V_{LT} = Adsorption capacity at temperature T, Equation 2.2

P_{LT} = Langmuir's constant at temperature, T, Equation 2.2

c3 = 0.0027

c7 = 0.005

CHAPTER 3

EVIDENCE AND CLUES

The production contribution from the U&L Shales, if there is any, should be reflected in the production-performance of the Bakken wells. During the onset of the project, efforts were made to investigate any evidence or clues to support the idea of production support from the U&L Shales. Reservoir engineering principles suggest delving into the field monitoring approaches, which include investigating the well production history and the shut-in and/or flowing pressure data. In the lack of available pressure data, the available production-history data proved to be the only option for this work. The well-organized database of the North Dakota Industrial Commission's (NDIC) oil & gas division website was extensively used to extract production history for different wells and fields.

Subsequent sections of the chapter include a detailed account of the following four pieces of evidence that support the idea of the U&L Shale production contribution:

1) Anomaly in the gas-oil ratio (GOR) trends
2) Production trends of the Elkhorn Ranch Field
3) Material balance analysis results
4) Single-phase results for a Bakken-type system

3.1 Fluid Expansion Drive in the Bakken

The primary recovery mechanism of a reservoir can be identified with its production performance plots. Figure 3.1 shows one of the commonly utilized: GOR versus time plots for the three fundamental primary recovery mechanisms. In the Bakken, oil is extremely undersaturated, suggesting no primary gas-cap can be expected to overlie the reservoir. There is no aquifer underlying the reservoir, implying that the Middle Bakken is left with the only option of fluid expansion drive (FED), which O'Brien, et al. (2012) also have suggested. The GOR for a Bakken well producing with the FED is expected to remain constant, and ideally it should be equal to the solution gas oil ratio (R_s) until the reservoir has depleted to the bubble-point

pressure. After that, the GOR is expected to rise monotonously until the very point of well abandonment as shown through the curve annotated as Expected-trend in the. However, in Bakken the GOR trends, as discussed in the subsequent sections, consistently deviate from the expected trend. The diverse Bakken GOR response could be approximately represented with the three idealized curves annotated as 1, 2 and 3 in Figure 3.2. The true reason behind this unusual behavior is not well understood. However, at least two different attempts to explain the unusual GOR response for the Bakken wells exist in the literature. Later in this chapter, they are discussed and some logical thoughts are also presented, which might limit their ability to fully address the issue.

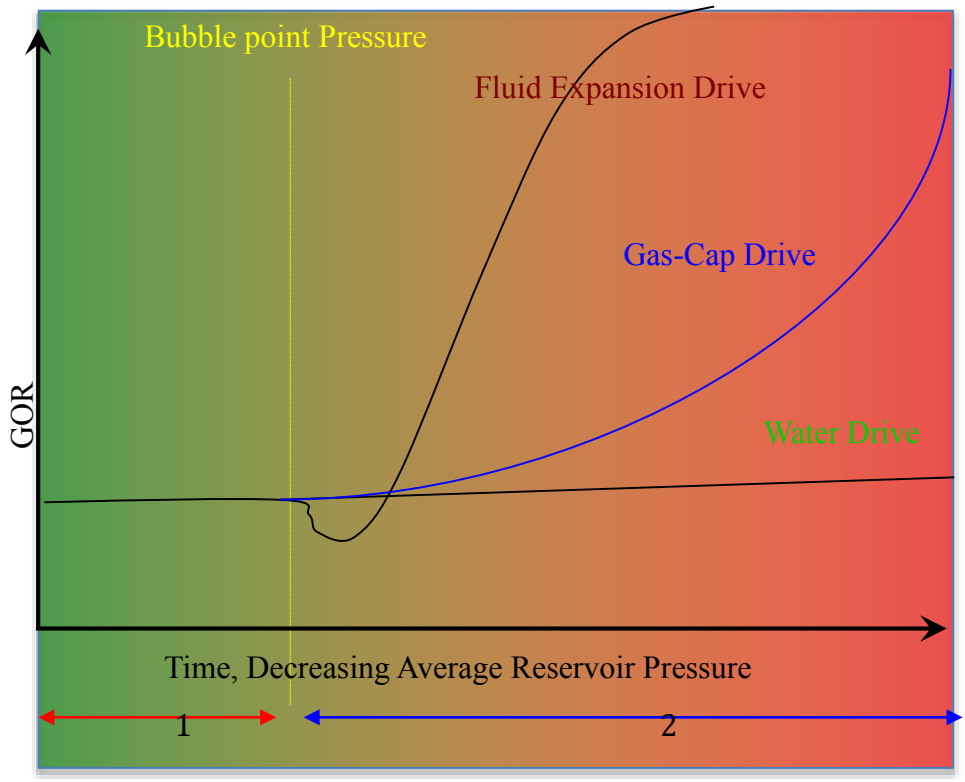

Figure 3.1: Well gas-oil ratio trends for different primary recovery mechanisms. Green to red gradient shows decreasing average reservoir pressure with recovery. Yellow broken line shows the bubble point pressure. Region 1 and region 2 across this line depict the two production-phases in which average reservoir pressure in above and below the bubble point respectively.

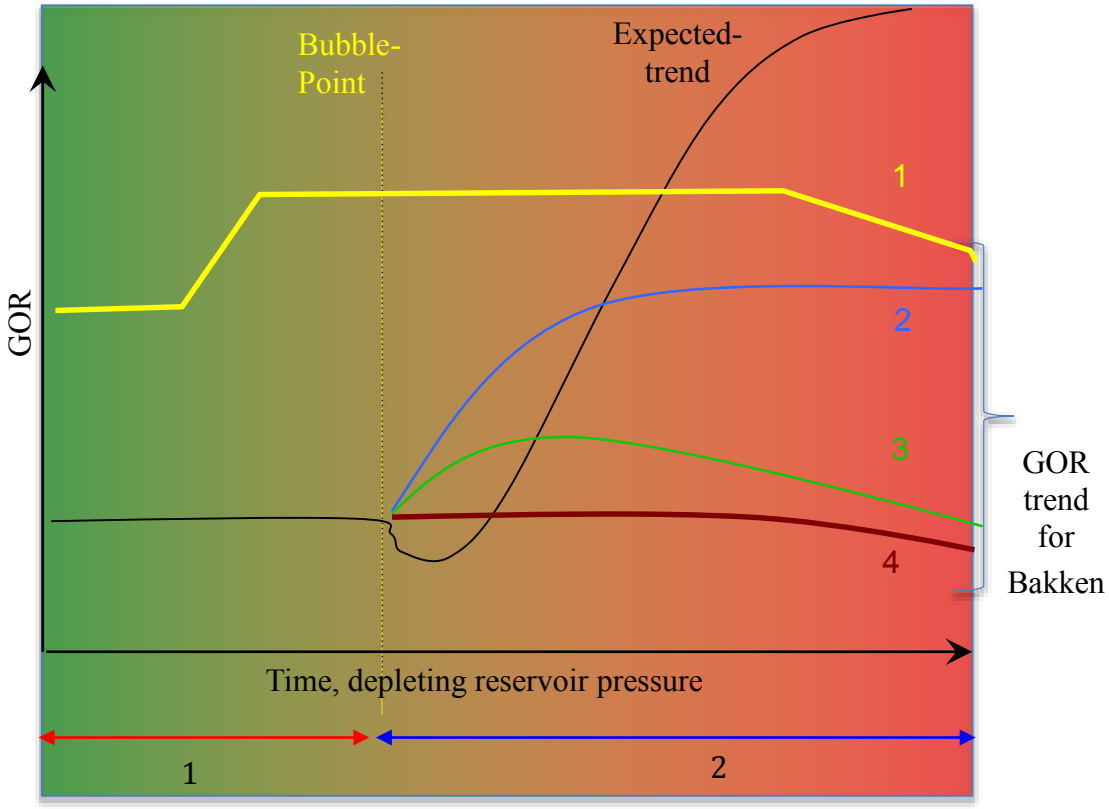

Figure 3.2: Expected and actual gas-oil ratio trends for the Bakken Wells.

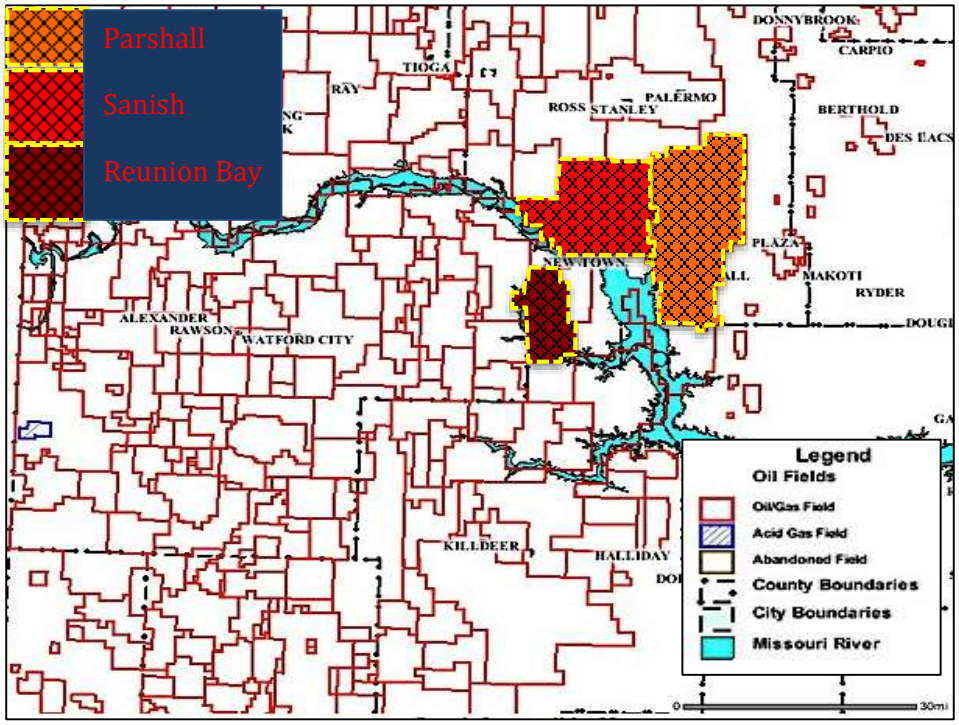

Figure 3.3: Location of Reunion Bay, Sanish, and Parshall fields in North Dakota Bakken Play (NDIC O&G Commission website).

3.2 Anomaly in the Gas-Oil Ratio

For this project, the gas-oil ratio (GOR) response for more than 500 horizontal wells of Reunion Bay, Sanish, and Parshall fields were plotted and collectively analyzed. The material-balance time (MBT) approach was used for time-scale normalization, and the cumulative GOR (CGOR) helped in minimizing the effect of short-lived rate fluctuations. A brief discussion on MBT and CGOR are enclosed in the Appendix A. Contrasts between the expected and the actual GOR trends were readily evident, which can be depicted through the illustration in Figure 3.2.

As illustrated in Figure 3.2, most of deviation from the expected trend was witnessed when the reservoirs seem to be operating below the bubble-point pressure. For the Bakken wells, in this production-phase, after a period of a steep rise, the GOR uncharacteristically became constant or in instances even dropped. The following is a field-wise analysis of the different GOR anomalies reported in selected representative example-wells:

3.2.1 Parshall Field

Figure 3.4 shows the GOR plot for few selected producing wells of the Parshall Field. Onset GOR for the wells consistently was within the 300-450 SCF/Bbl range, suggesting that they have behaved normally. The reservoirs around all the wells seemed to have depleted to the bubble point pressure at approximately 0.6 MBT, and after that a steep rise in the producing GOR was observed. In contrary to the expected monotonous ever-rising trend, the GOR uncharacteristically became constant after a while.

3.2.2 Reunion Bay Field

Figure 3.5 shows the GOR versus time plot for representative example-wells of the Reunion Bay Field. Relatively higher rate fluctuation during the initial monthly data was observed, which could be attributed to the water after-flow that follows the hydraulic fracture job in the wells. Initial CGOR for most of the wells lied within 800-1000 SCF/Bbl range. However, wells 16778 and 18088 have shown considerably lower initial CGOR of 450 and 650 SCF/Bbl respectively. Low initial GOR is certainly an anomaly as adjacent wells from the same undersaturated reservoir are producing with almost a double initial CGOR values. Alternatively, it can also be proposed that the wells with low GOR might be producing exclusively from the

middle layer. While, the wells with high initial CGOR (or high gas rate) might be getting the extra gas-volume from desorption taking place in U&L Shale.

For well 16778, which had lower initial GOR, it took considerably longer (0.7 MBT) time to reach the bubble-point pressure. As discussed earlier, this well was expected not to be getting desorped-gas from the U&L Shale; it might bear the actual PVT signatures of the reservoir fluid. For well 18088, 16686 and 16772, it took almost 0.5, 0.3 and 0.1 MBTs respectively to witness the characteristic steep-rise in CGOR. This CGOR rise might or might not be an indication of the bubble-point pressure attainment. The reason for this uncertainty is that the steep rise in CGOR could be happening because of the breakthrough of the desorped-gas from the U&L Shale.

After this point, an unusually diversified GOR trends were observed:

1. For wells 16778, 18088 and 16686, the GOR later became constant after a while.
2. For the well 16772, CGOR first rose, got stabilized, and later it even declined. The well 17771 seemed to have produced below the bubble point pressure since its inception.
3. For the well 16687, it had higher CGOR during initial above the bubble-point production phase than those during below the bubble point production-phase.

3.2.3 Sanish Field

Sanish field is located adjacent to the Parshall field in the to its western boundary. However, the GOR trends observed for the Sanish wells do not confirm with the Parshall field wells. For the Sanish Field, the GOR values seemed inconsistent throughout the production history of the wells (Figure 3.6). A contrast was expected between the production-phases separated by the time when bubble-point pressure is attained (Figure 3.2), which appeared not to have happened for the Sanish Field. For this reason, the bubble-points could not be identified from the GOR performance curve, and it seems as if the GOR has the similar trends throughout their production-life. Therefore, it is not easy to find the time at which the reservoir pressure has dropped below the bellow point.

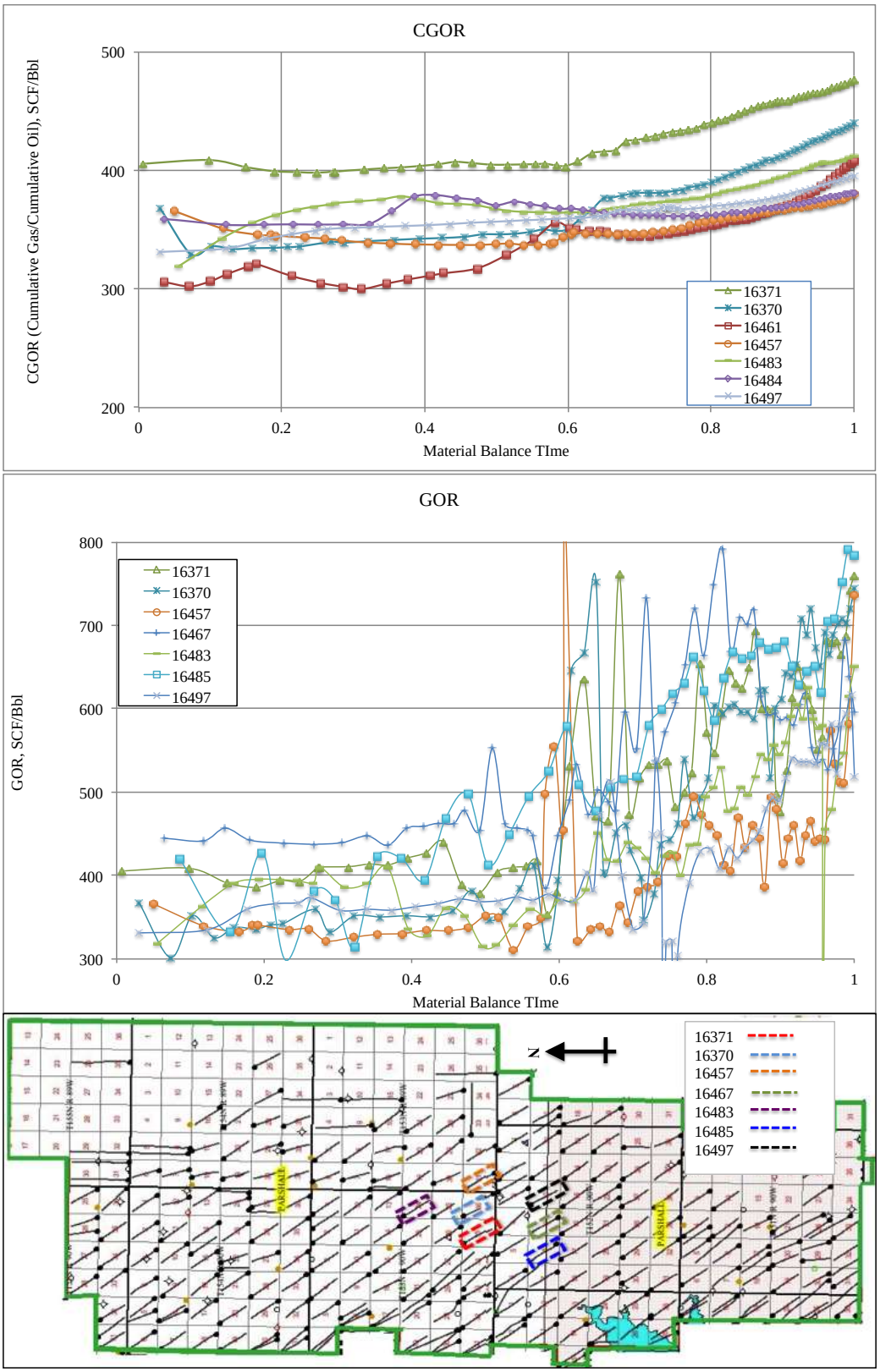

Figure 3.4: Gas-oil ratio versus material balance time and cumulative gas-oil ratio versus material balance time plotted for selected Parshall Field wells. The map shows well location in the field.

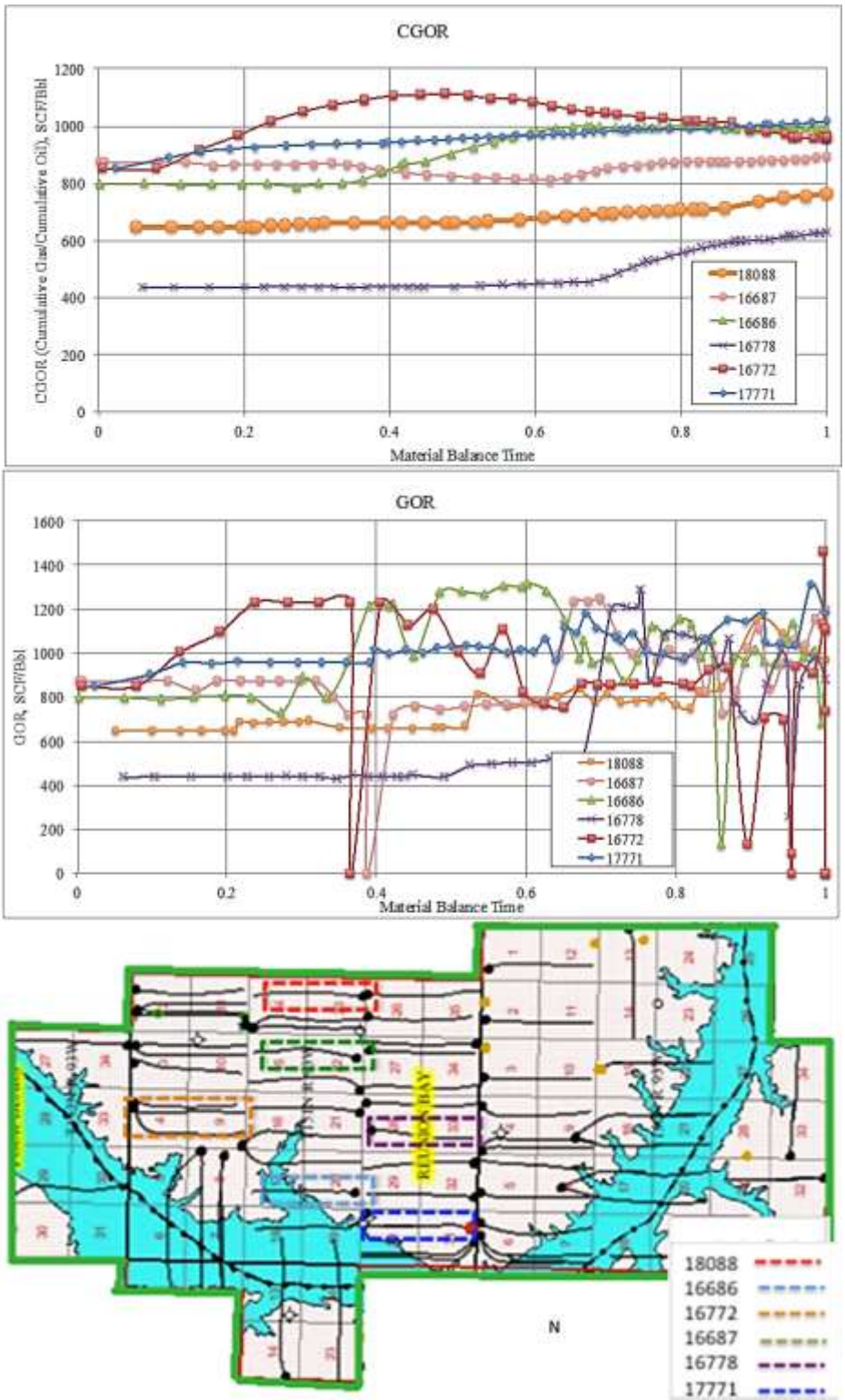

Figure 3.5: Gas-oil ratio versus material balance time and cumulative gas-oil ratio versus material balance time plotted for selected Reunion Bay Field wells. The map shows well location in the field.

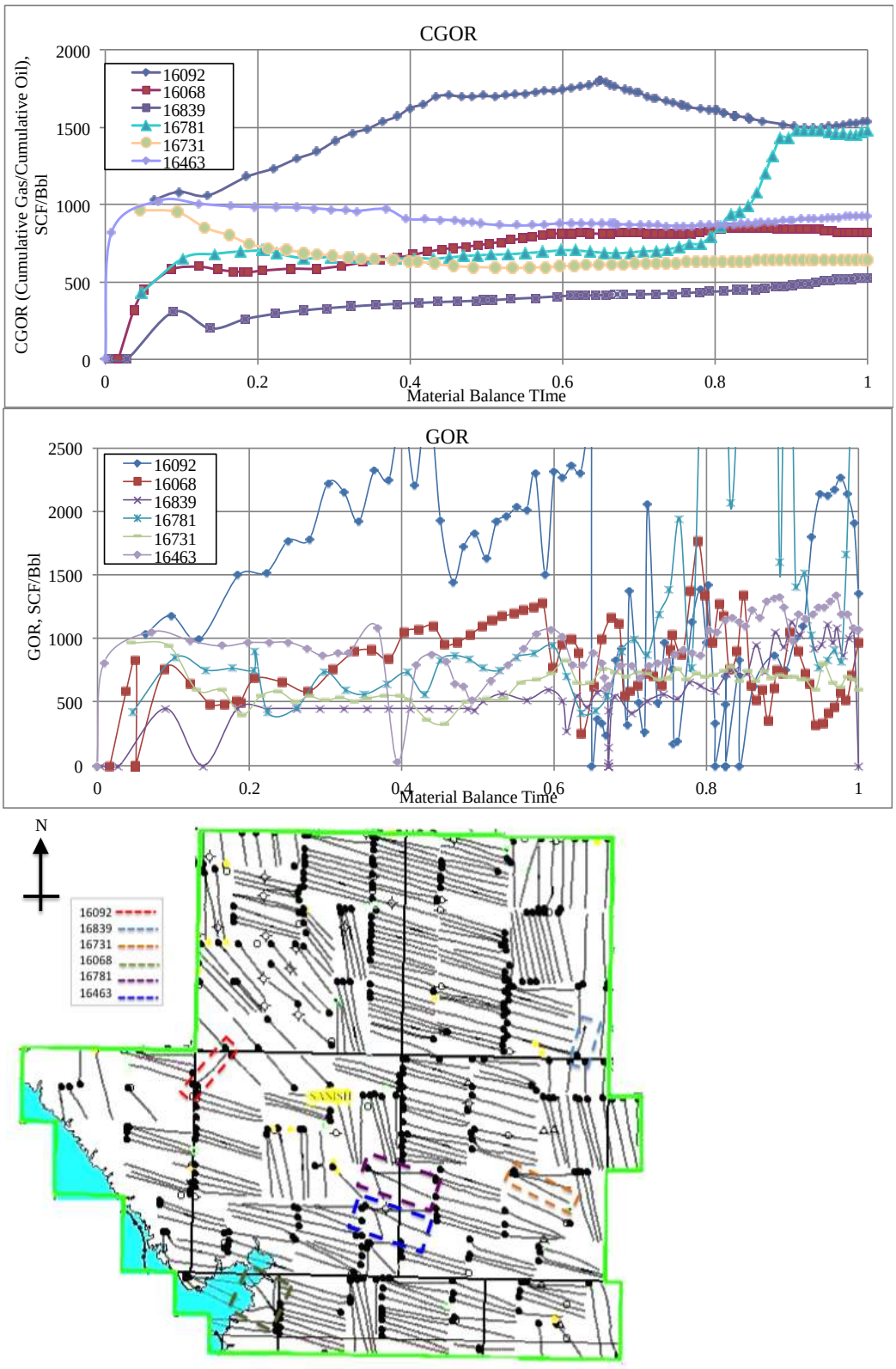

Figure 3.6: Gas-oil ratio versus material balance time and cumulative gas-oil ratio versus material balance time plotted for selected Sanish Field wells. The map shows the well location in the field.

3.3 Elkhorn Ranch Field

Located in the well-known Fairway area, the Elkhorn Ranch field is one of the oldest producing-field of the North Dakota Bakken play (Figure 3.7). In Year 1961, oil was accidentally discovered in the Upper Bakken Shale when Shell (operator of the field) tried this prospect as their secondary objective in a well. The well eventually produced consistently for many years. The field has been a marginal producer from the tight Upper Shale and to enhance the production hydraulic fracturing and horizontal drilling options were first tried in the year 1976 and 1987 respectively. This long history is marked by diversified results, which has limited commercial viability of the Upper Shale prospect in the region. After the year 2000, it was further pushed to the brim with the overwhelming evolution of the middle-Bakken prospect as the major producer.

The field was chosen for this study as it had offered analyzable production data from both: the Upper Shale and the Middle Bakken reservoirs. Cumulative-GOR (CGOR) versus cumulative produced oil (CPO) performance curve were plotted to investigate the production performance for all the wells from the field. Figure 3.8 shows the variety of the CGOR response for the wells. However, based on the nature of the performance-curves, the wells can be categorized in the following three-groups:

1. **Group-1** wells seemed to have achieved distinctly high CGOR in the early stages (Figure 3.8), and the enormous gas production might be the reason behind their early abandonments. Two wells: 13219 and 13256, in particular, produced with unusually high CGOR of 17,000 and 40,000 SCF/Bbl, which was up to 30-40 times higher than normal. Enormously high producing-GOR (PGOR) trends of the Group-1 wells are shown in Figure-3.8.
2. **Group-2** wells initially produced with subdued CGOR of around 1000 SCF/Bbl, but in later stages it has increased abruptly (Figure 3.8). The CGOR values might seem to have risen to moderate levels of 4000 SCF/Bbl, but these wells produced with high instantaneous PGOR values ranging up to 30000 SCF/Bbl (Figure 3.10).
3. **Group-3** wells produced with much-subdued CGOR and instantaneous PGOR values of around 1000 SCF/Bbl throughout their life (Figure 3.8 & Figure 3.11).

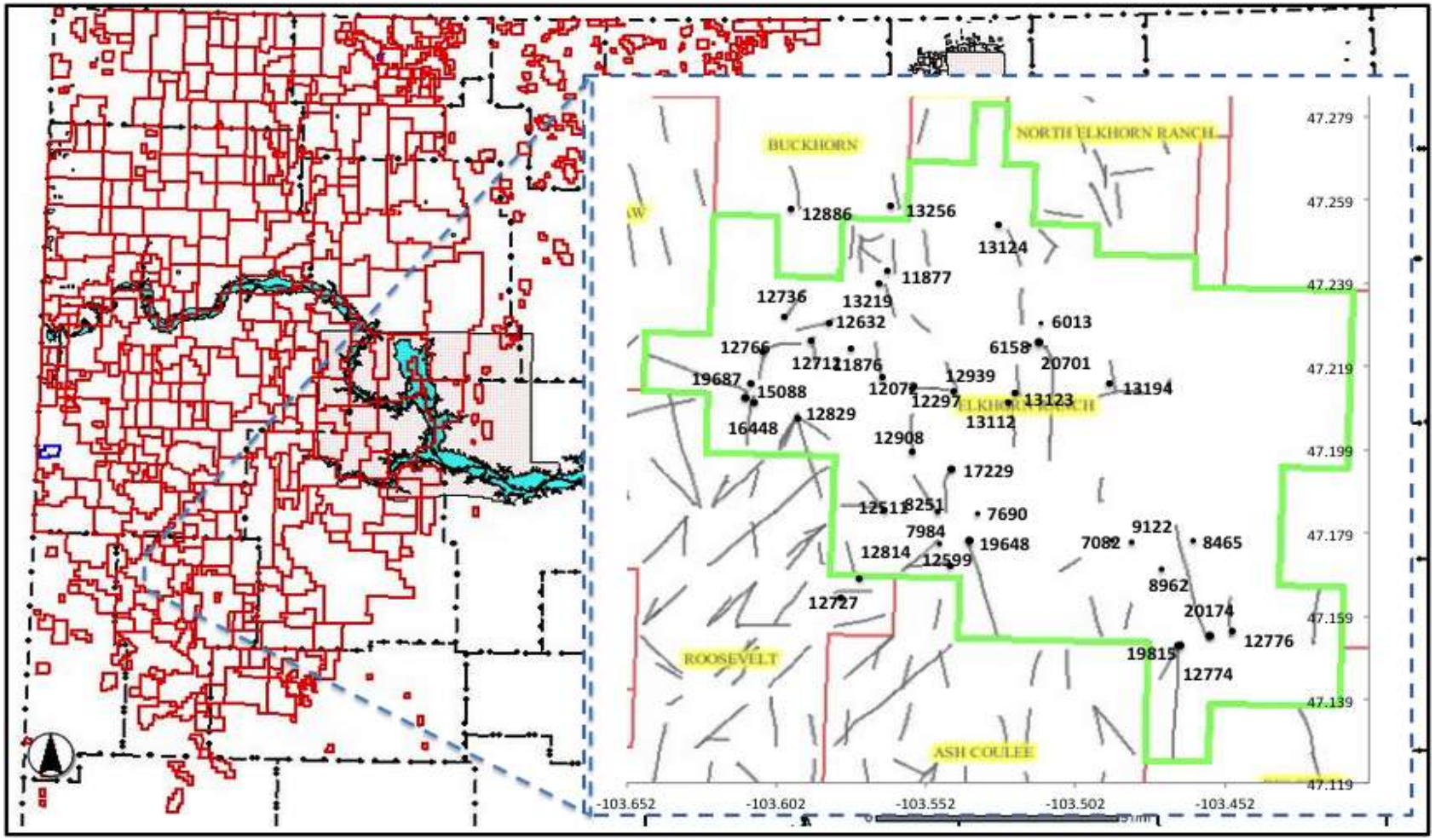

Figure 3.7: Location of the Elkhorn Ranch Field in North Dakota Bakken Play.

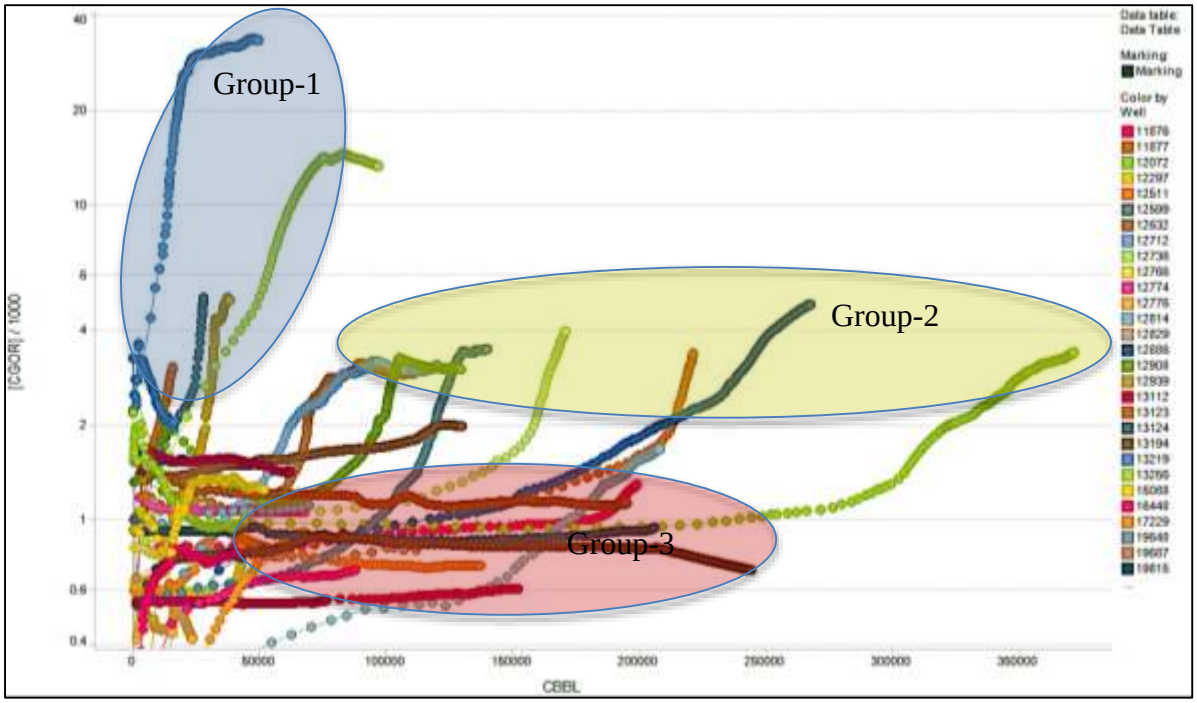

Figure 3.8: Chart showing the cumulative gas-oil ratio response of the wells plotted with the respective cumulative oil production in barrel.

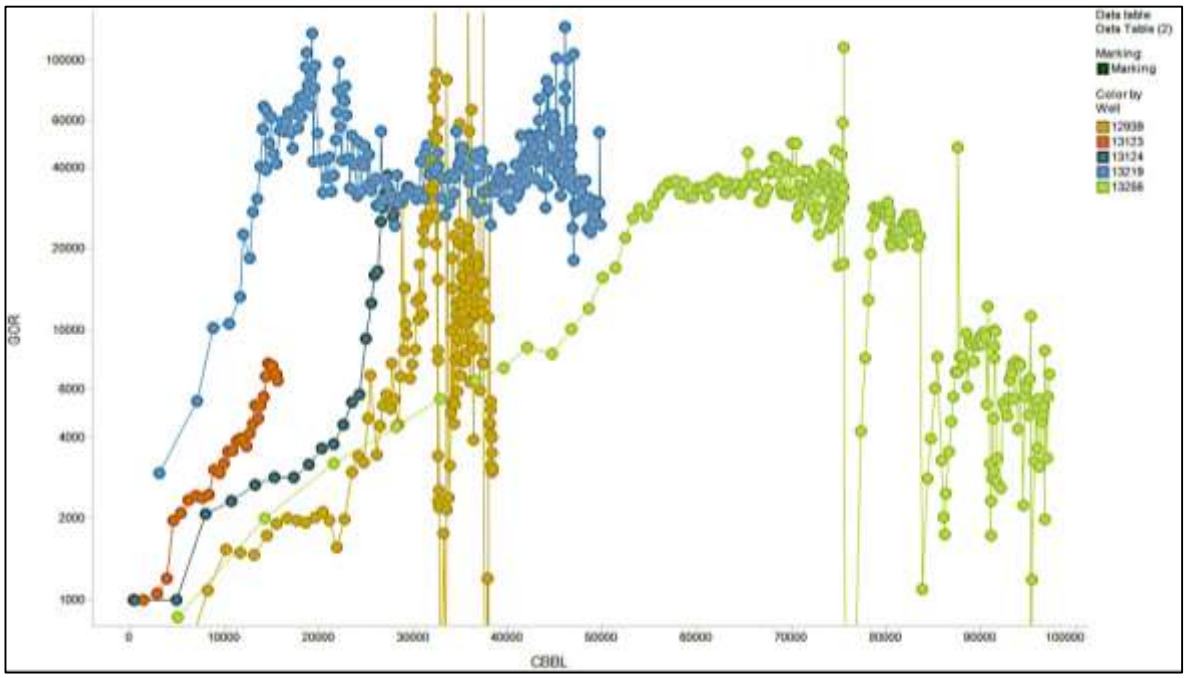

Figure 3.9: Producing gas-oil ratio of Group-1wells of the Elkhorn Ranch Field.

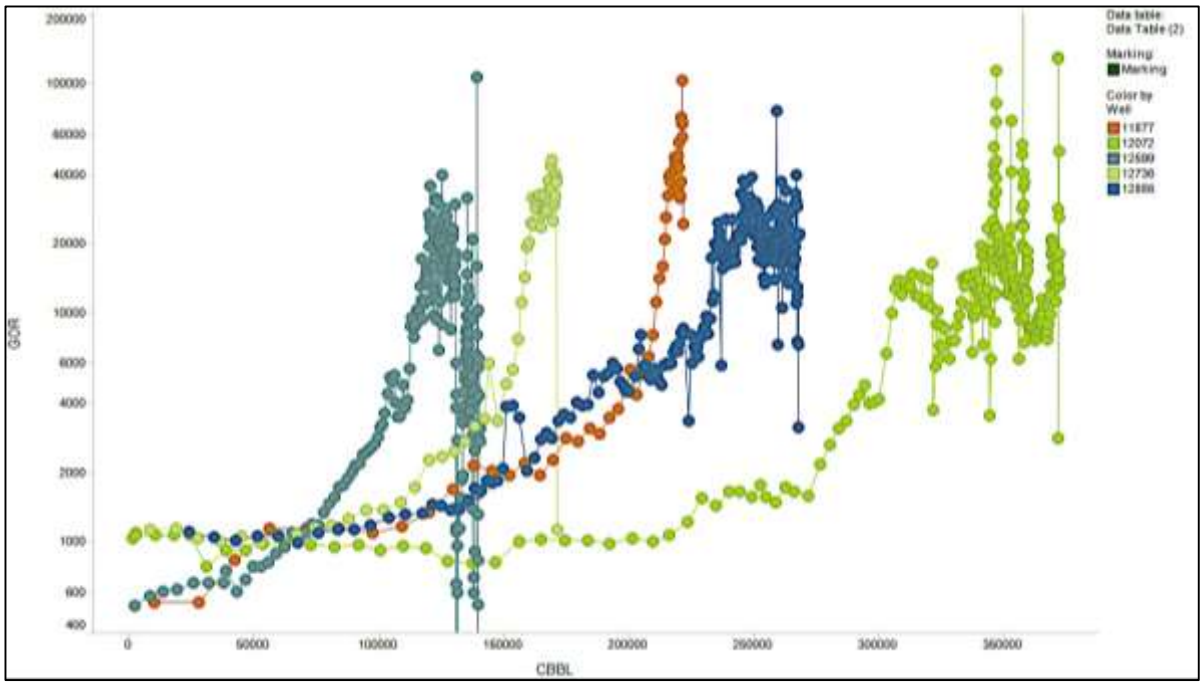

Figure 3.10: Producing gas oil ratio of the Group-2 wells of Elkhorn Ranch Field.

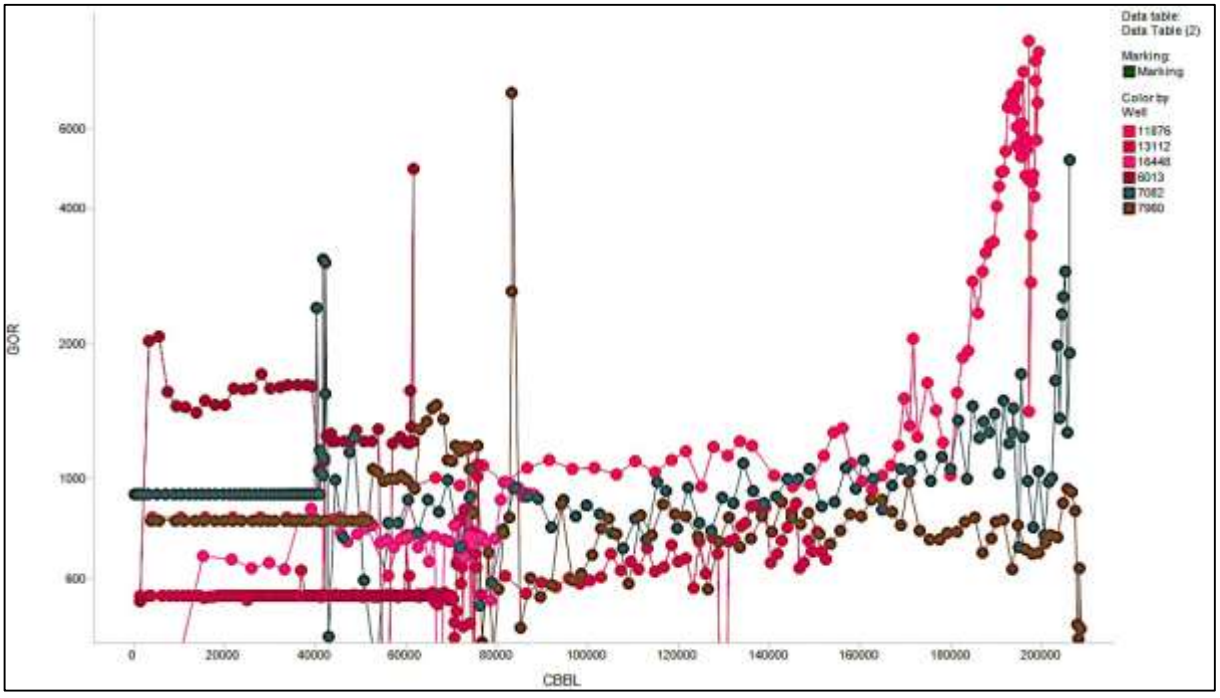

Figure 3.11: Producing gas-oil ratio of the Group-3 wells of Elkhorn Ranch Field.

Getting such a diversified GOR response for wells, producing from the same field can be dubbed as unusual. Varying degree of production support from the U&L Shale layers could be the reason behind this abnormality. To pursue this idea, production data of the wells and the

available geological information on the U&L Shale were collectively analyzed. Abandonment-CGOR and ultimate cumulative oil data (Appendix B) for all wells were traced on the areal TOC content distribution and isopach maps of the U&L Shale (Figure 3.12). The size of the bubble represents the CGOR, and the color scheme indicates the ultimate cumulative oil for the wells. It was assumed that all the three Bakken-layers are interconnected as all of them are marginally developed within a cumulative thickness of 50-60ft in this area of the Bakken.

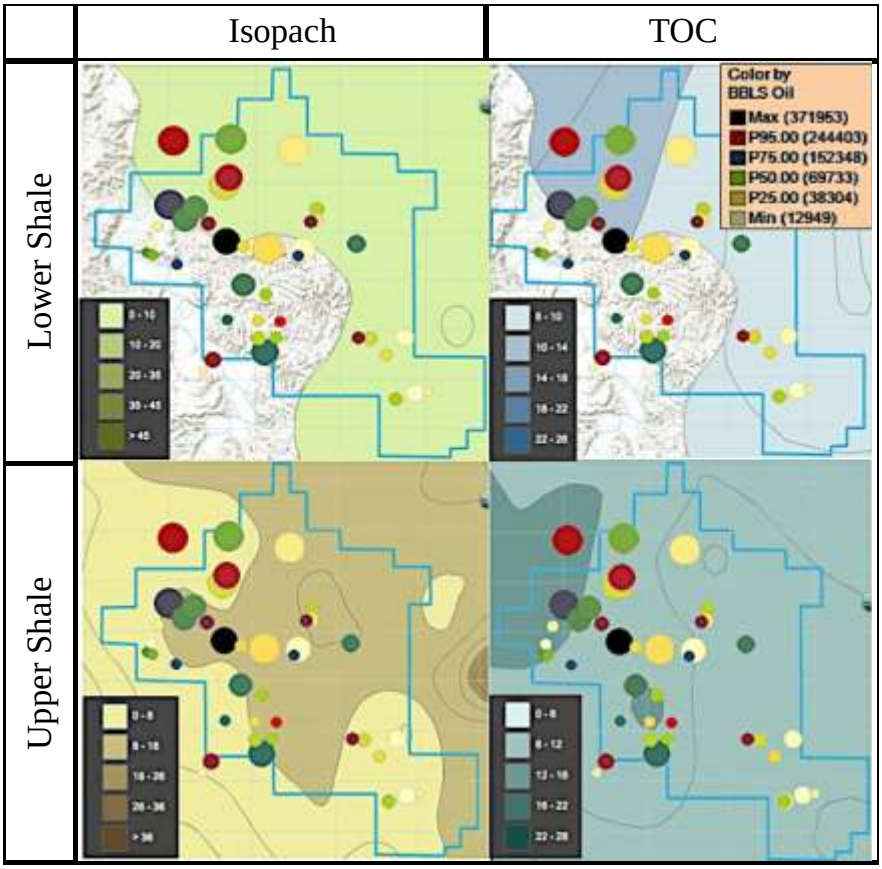

Figure 3.12: Cumulative gas-oil ratio and ultimate oil production plotted as bubble chart (Data Source: NDIC, Oil & Gas Division 2013) over the total organic carbon distribution and isopach maps (EERC 2013) for the Upper and Lower Shale layers.

The higher CGOR or PGOR for the wells could be associated with the higher degree of gas desorption taking place in the U&L Shale. As discussed in Chapter-2, gas adsorption capacity of SRS is directly proportional to its TOC content. Figure 3.12 suggests that the Lower Shale layer terminates within the field-boundaries, and several wells are located in the regions where this layer is absent. Such regions have smaller CGOR bubbles, suggesting that the extra gas in the larger bubbles across the layer-termination boundary may be attributed to the gas

desorption taking place in the Lower Shale. The argument was further substantiated by the fact that the wells located in the high TOC content (higher desorption) regions of the Lower Shale (Figure 3.12, dark blue shade) have a concentration of larger bubbles. Similarly, the thickness of the Upper Shale also seemed to have an effect the CGOR variation. The effect of Upper Shale's TOC content distribution was not that much prominent, although an increase in TOC content resulted in bubble-size increase in more than four instances.

3.4 Unusual GOR behavior: Views from the Literature

Unusual GOR behavior for Bakken wells has been investigated in the past, and the following two explanations for this abnormality exist in the literature.

3.4.1 PVT property alteration in nanopores

Nojabaei, et al. (2012) suggested that tiny nanopores, such as those in the tight Bakken reservoir might alter the hydrocarbon phase behavior. Theoretically, phase transitions at bubble-point or dew-point require an extra pressure-change, which is equal to the capillary pressure between the two transitioning-phases. In the macropores, the capillary pressure is considerably small in comparison to the usual phase transition pressures, so this effect can be ignored. However, in case of the nanopores, gas-oil capillary pressure becomes significant and the effect of capillarity on PVT properties cannot be ignored anymore. The effect is synergized by the recovery driven compaction as it results in a pore-size contraction. Figure 3.13 shows the effects of both pore-radius and compaction on the bubble-point pressure of a live-oil sample. Nojabaei et al. (2012) have reported anomaly for two Bakken producers (Figure 3.14), and suggested that the unusual behavior might be a repercussion of the PVT alteration in nanopores.

Potential limitation: However, there is a potential limitation to the above-discussed idea. Most of the tight reservoirs with nanopores are considered to have a dual-porosity flow media. In these systems, the nanopores of the matrix store the hydrocarbon, and most of the fluid transportation takes place through the macro-sized fracture-network. Thus, the hydrocarbon before getting produced would eventually pass through this macro-sized fracture-network. In such situations, the reservoir fluids can exhibit their normal PVT properties, and GOR response is expected not to deviate from the normal-trends.

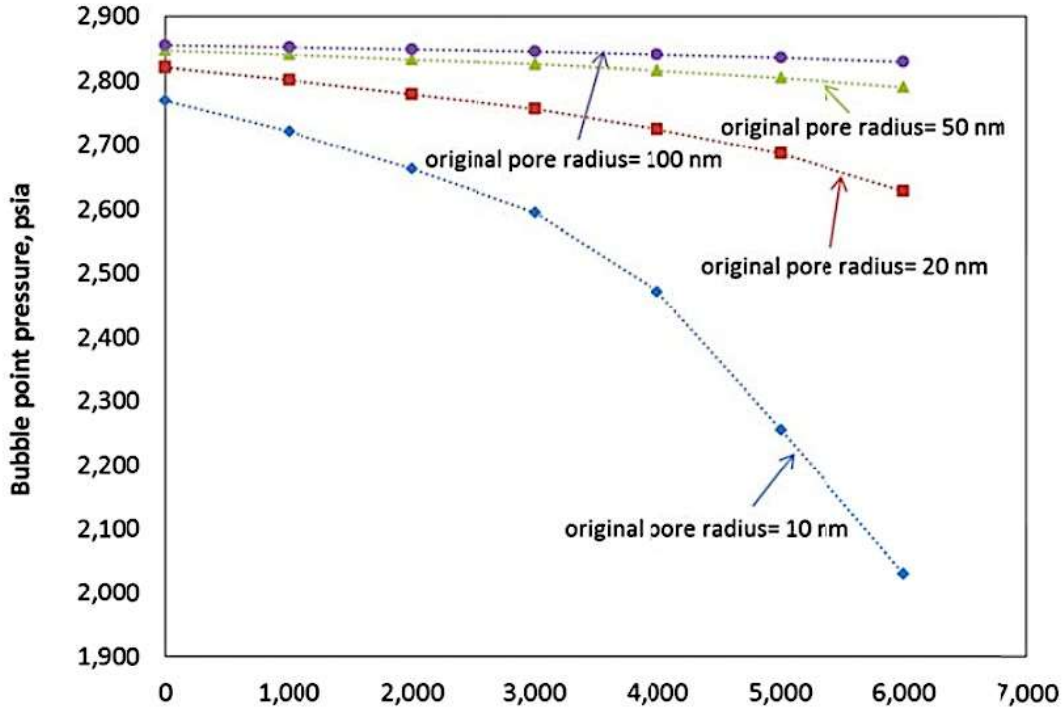

Figure 3.13: Effect of nanopores and compaction on the bubble point pressure (Nojabaei,et al. 2012)

3.4.2 Matrix Pressure Support to Fracture

Tran et al. (2011) have proposed the idea of matrix support to be the reason behind the flattening GOR response in the Bakken. It was shown that the well, which had produced with stabilized GOR similar to the Type 1 or 2 curves in Figure 3.2, had also registered a flat stabilized oil production rates. These wells were considered to be producing from reservoirs, with an active matrix-to-fracture fluid transfer. The matrix support was assumed to be eventually arresting the reservoir pressure decline and thereby inhibit the gas from coming out of the solution, which may stabilize of the GOR response. The other kind of wells, which had reported a sharp rise in the GOR, was associated rapid oil production decline. For this category of the wells, it was suggested that there is no matrix-to-fracture fluid-transfer taking place in the reservoir to arrest the reservoir pressure decline. As the pressure in the reservoir rapidly depletes, increasingly more amount of gas evolves out of the oil, which explains the sharp rise in GOR with time.

Potential limitation: In the Middle Bakken reservoir, most of the oil is assumed to reside within the natural horizontal-fractures and adjacent micro-fractures. Negligible fraction of oil is

located in the Middle Bakken matrix (LeFever, 2001), so not much support can be expected from their matrix. Thus, the concept of matrix the Middle Bakken matrix support to be the reason behind the GOR anomaly might have a limited-scope.

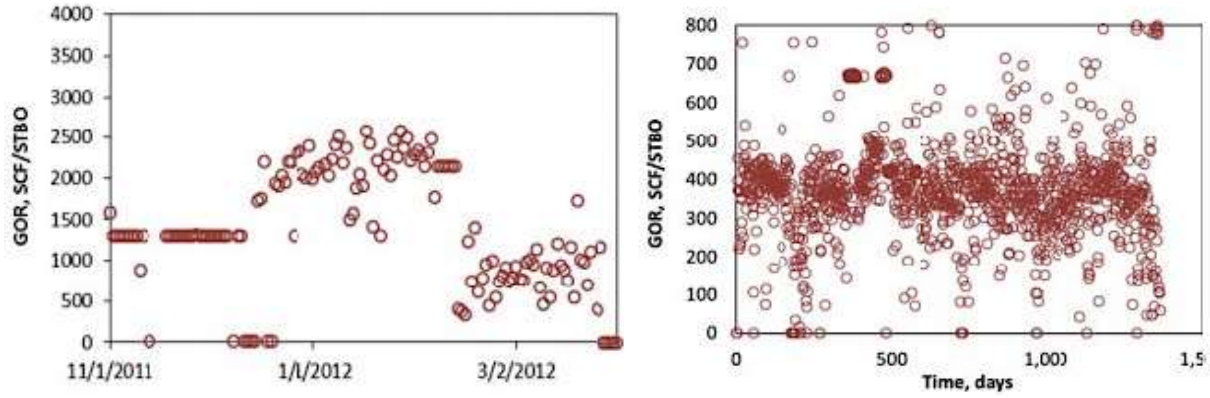

Figure 3.14: GOR anomaly for two Bakken wells (from Nojabaei et al., 2012). It could be noted here that similar gas-oil ratio anomalies were discussed in the previous section of this chapter.

3.4.3 GOR Anomaly and U&L Shale Contribution

As discussed in the previous chapter, TOC controls the adsorption-capacity of the self-resourcing shale (SRS). Desorped hydrocarbon volume from the U&L Bakken Shale layers is expected to vary in accordance with the respective areal TOC distribution map (Figure 3.15). With that, the diverse GOR response can be explained by considering the intermingling of the Middle Bakken oil with varying amount of desorped hydrocarbon contributed from the U&L Shale. This is expected to prompt alteration in reservoir fluid composition altogether and the effect is expected to correlate with the TOC of the U&L Shale layers.

The restrained GOR response for the wells could be attributed to the arrest in the pressure drop due to the production-contribution as desorption in U&L Shale take place. The desorped gas or liquid molecule could replenish the voidage created by production, which might act like a recovery drive. The higher GOR in some instances at the very early production-stages could be attributed to a situation when the predominant desorping molecule is methane, which bypasses the oil and break-through into well. This situation could be severe, especially when the some portion of the horizontal well is penetrating inside the Upper or the Lower Shale.

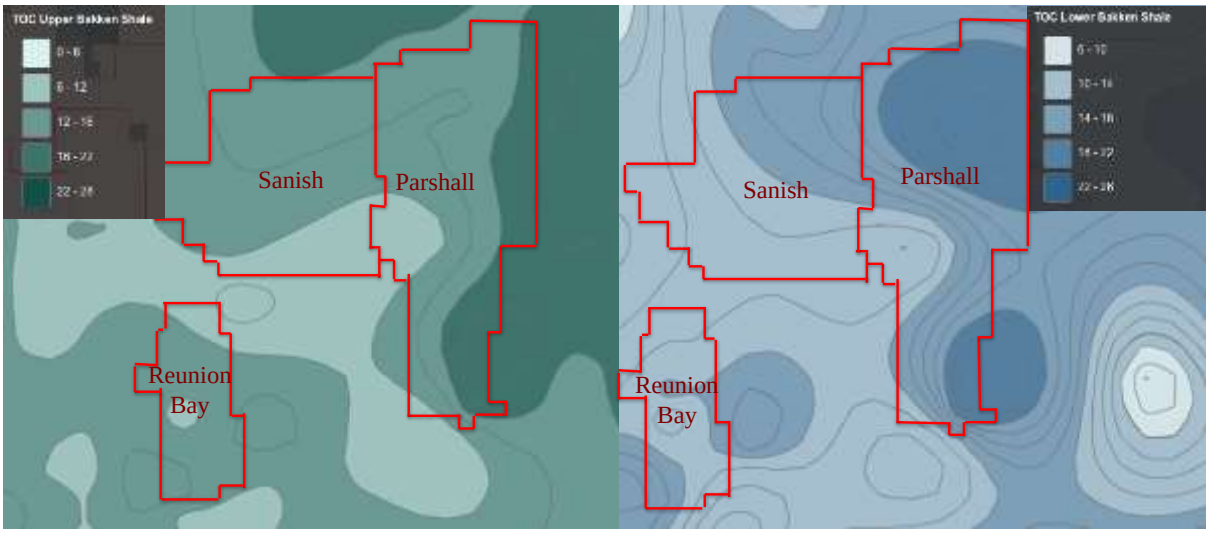

Figure 3.15: Total organic carbon areal distribution, Upper and Lower Bakken Shale.

3.5 Material Balance (MB) Analysis

The MB analysis was aimed at studying the average reservoir pressure versus recovery-factor (RF) response for the Middle Bakken reservoir. Reservoir surrounding horizontal wells 16346 and 16370 from the Parshall Field was chosen to perform this study. The required PVT data for the MB calculation were adopted from a real PVT report for a Middle Bakken well of the Elm Coulee Field. A detailed account for the Material Balance calculations is enclosed in Appendix C.

No production support from the U&L Shale layers should prompt the reservoir to operate on the fluid expansion drive (FED). In the initial production-phase when the average reservoir pressure is above the bubble-point, the recovery is driven by the oil expansion. Lower compressibility (slight expansion for a finite pressure-drop) of oil prompts a rapid decline in the average reservoir pressure. As per the MB analysis, the reservoir should undergo a pressure decline from initial reservoir pressure of 7000 psi to 1567psi (expected bubble-point) to achieve a RF of about 4-5% (Figure 3.16).

Artificial-lifts for these two wells were installed probably once average reservoir pressure declined below 3000 psi (well scout-ticket, NDIC O&G division website). In the later production-phase, when the reservoir has depleted below the bubble point pressure, solution-gas is expected to evolve out of the oil-phase. The evolved gas, with higher compressibility values

arrests the pressure decline to some extent. In this production phase, the MB analysis suggests depletion to about 1100psi and 500psi average reservoir pressure to achieve 10% and 20% RF respectively (Figure 3.16).

Even an optimistic volumetric calculation suggested that the current RF for the chosen wells (16346 and 16370) should not be less than 10%. As per the MB analysis, at this RF the average reservoir pressure around the wells are expected to be less than 1100 psi, provided that there was no external pressure support. The current oil rates for these wells producing on the artificial-lift exceed 70-80 BOPD. These rates would be difficult to sustain if the reservoir pressure was less than 1100 psi, especially from a 10000ft deep and 6000ft long horizontal well. The average reservoir pressure around the well must be much more than 1100 psi and the depleted reservoir pressure can be above the MB estimated value, only if there is some external pressure support to the Middle Bakken reservoir. Production contribution from the U&L Shale could provide one such pressure support to the Middle Bakken reservoir, which in turn can justify the high average reservoir pressure to sustain the observed oil production rates for the two chosen wells.

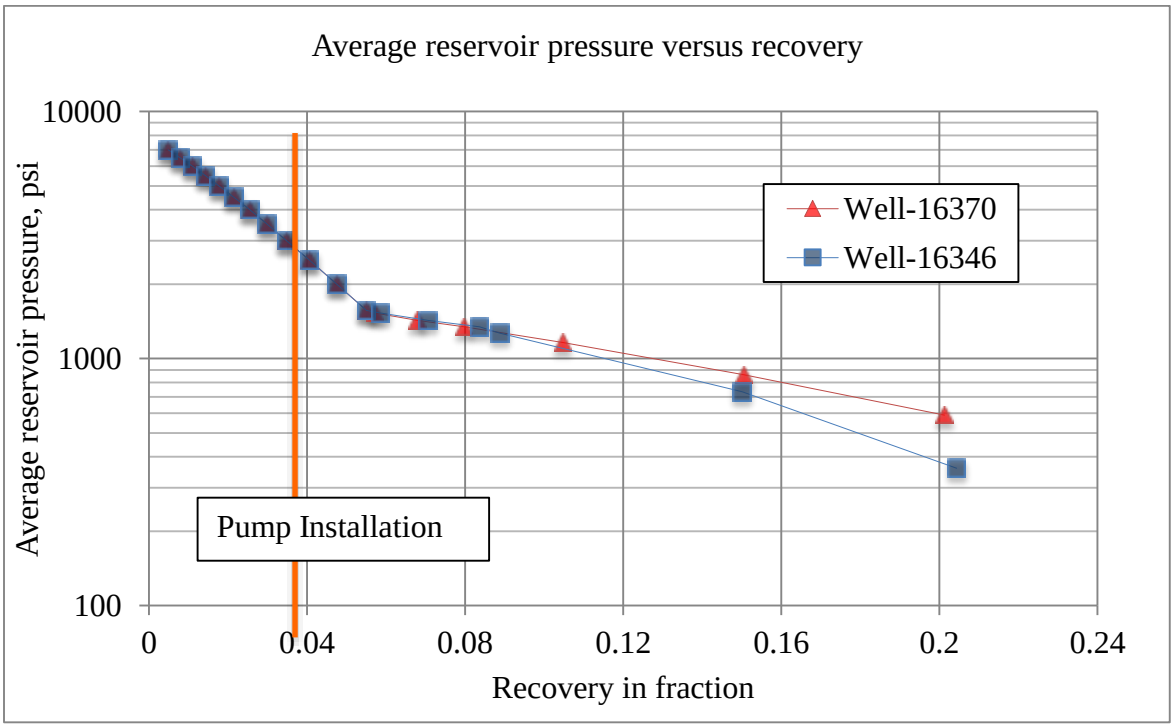

Figure 3.16: Chart depicting the material-balance derived results: recovery factor versus average reservoir pressure for two wells of Parshall Field.

3.6 Single Phase Simulation in FORTRAN

The purpose of this study was to study the effect of desorption in the U&L Shale matrix on the production-performance of a simplified Bakken reservoir. The results were derived for a hypothetical case in which the reservoir was saturated with a single-phase fluid, which has methane as its only component. Methane was also the only component that was desorping from the U&L Shale matrix.

3.6.1 Bakken Prototype and FORTRAN Simulator

A Bakken system prototype geomodel was simulated utilizing a FORTRAN-code to get a single-phase fluid (methane) production response. The geomodel can be schematically represented through Figure 3.17, whereas Table 3.1 lists the numerical values for the reservoir, fluid and well properties. The detail of the mathematical development of the simulation-scheme for the FORTRAN code is found in Appendix D. All three layers have dual porosity media, and the mesh pattern in Figure 3.17 depicts the three-dimensional fracture-network (both natural and hydraulic).

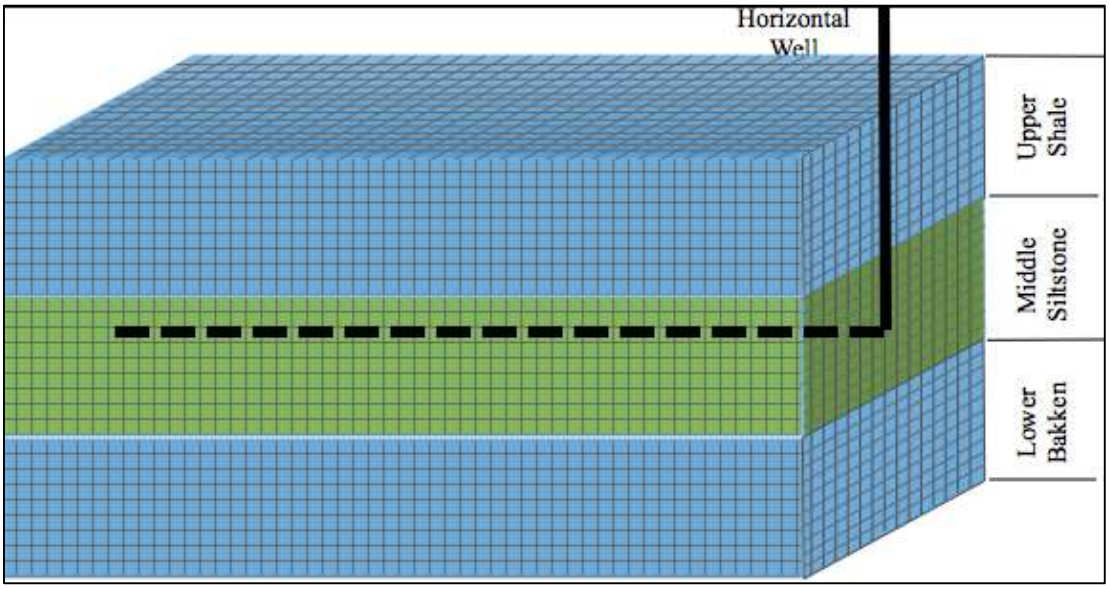

Figure 3.17: Schematic diagram showing the geomodel for the single-phase simulation on FORTRAN.

A horizontal well is centrally completed in the middle layer to produce from the reservoir under constant bottom-hole pressure control. The upper and lower (U&L) layers are considered to have adsorbed methane molecules in their matrix and their desorption follow the Langmuir-isotherm shown in Figure 3.18. The matrix-to-fracture fluid transfer in the U&L layers was considered to follow the principles of convective (diffusive) gas flow. The Middle layer was considered to contain no adsorbed gas, and here the matrix-to-fracture transfer was considered to follow the principles of an advective type (Darcy type) flow.

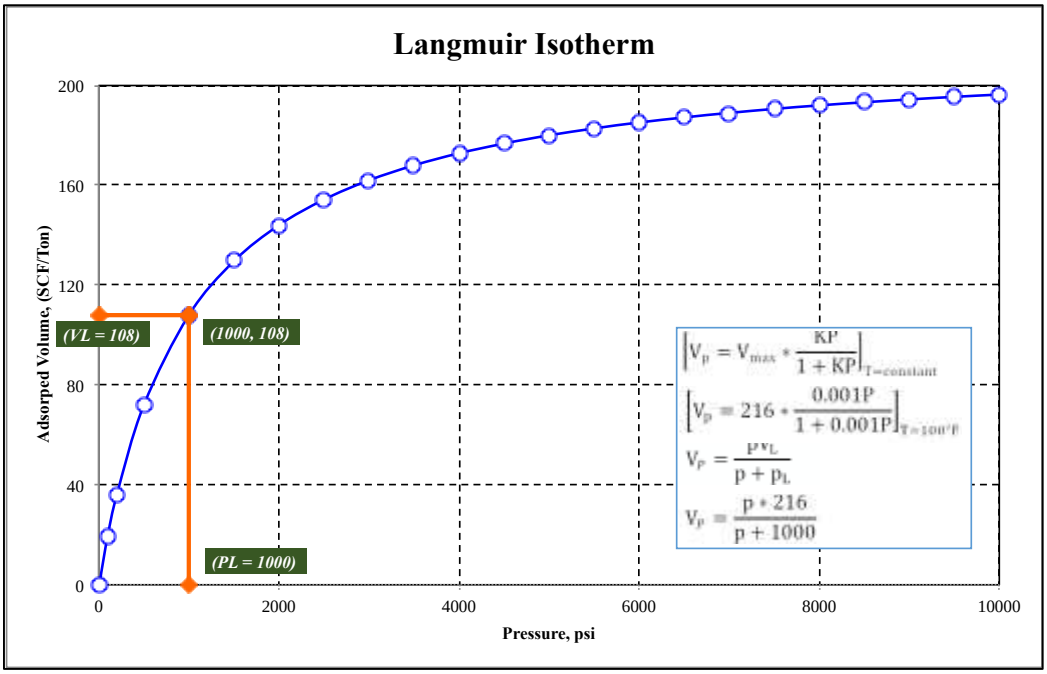

Figure 3.18: Langmuir isotherm for the single-phase simulation.

3.6.2 Single Phase Result

Two simulation-runs were performed on the FORTRAN-code, one on the system as described above, and other on the same system, but this time the fracture-permeability in the U&L layers were set to zero. The output of the simulation-run was time versus average reservoir pressure of the well containing grid-block. The difference in the pressure response with time for the well containing grid-block for the two runs could be witnessed in Figure 3.19. The sustained higher pressure in the in the well-containing grid block points that the U&L Shale layers active contribution through desorption could significantly alter the recover from the reservoir.

Table 3.1: Parameters used in single-phase simulation

Gridding:

(1×7×3) Uniform Gridding

$\Delta x = 7000ft$ $\Delta y = 250ft$ $\Delta z = 35ft$

Well Location and Parameters:

Well's Grid-Address: (1,4,2)

Well-radius: $r_{well} = 0.25ft$

Fracture Properties:

$X_f = y_f = z_f = 1ft$

$W_f = 10\mu m$

Matrix Properties:

Siltstone Matrix Permeability: $k_{mat} = .0001$ mD

U&L Shale Gas Diffusion-coefficient: $D=1.0$ cm^2/sec

Fluid Properties:

Viscosity of methane: $\mu = 0.02cp$

Initial reservoir Pressure: $P_{Res} = 6500Psi$

Simulation-Run Controls:

Well flow-in Bottom Hole Pressure: $P_{wf} = 1500$ Psi

Time Step: 100 time steps on logarithmic scale

Total Run Time: $T_f = 1000$ Days

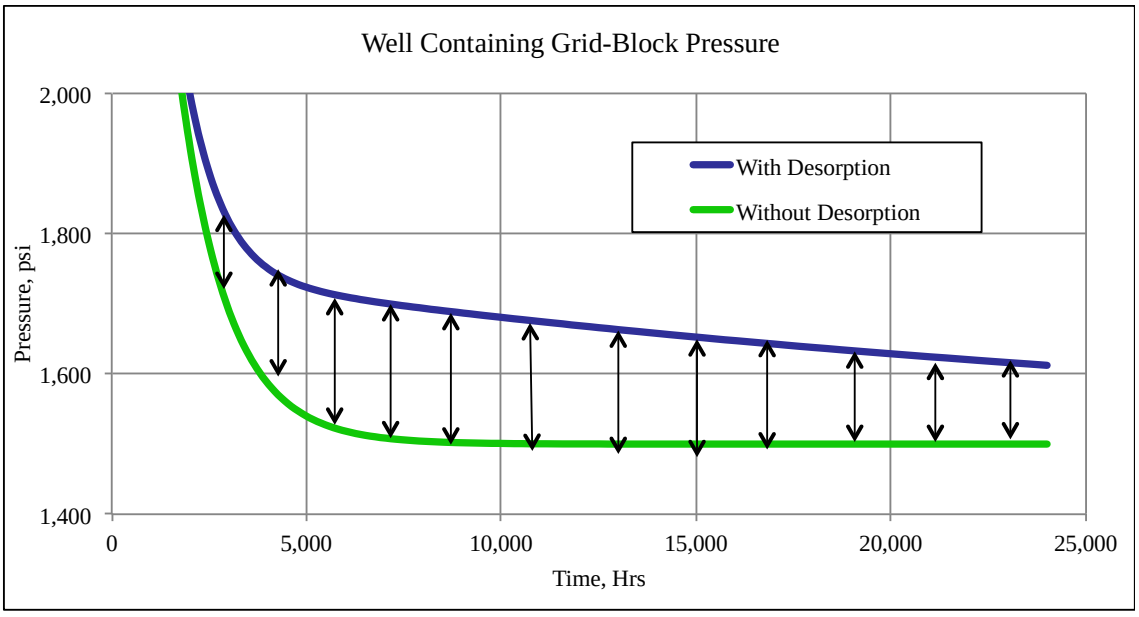

Figure 3.19: Comparison between the well containing grid block pressure for the contribution case and the non-contribution case runs.

CHAPTER 4

METHODOLOGY

This chapter provides an overview of the quantification-scheme for the anticipated production-contribution from the U&L Bakken Shale to the Middle Bakken reservoir. Each of the four pieces of evidence elaborated in Chapter 3 strongly indicated the proposed production-contribution. The theoretical outline of the controlling physical processes, discussed in Chapter 2, was critical in designing the quantification scheme for this research. It could be noted here that many of these processes are not even fully understood, and the research pertaining to them in the literature are in their incipient stages. Therefore, most of these processes when applied in the quantification-scheme are shown to have either empirically developed formulations or an analogical-background.

4.1 Reservoir Simulation Tool

The reservoir simulation tool was an obvious choice for this research as it provides the robustness and the flexibility to incorporate the mathematical formulations for the controlling physical processes discussed in Chapter 2. Based on their theoretical-outlines, the adopted reservoir simulation scheme had the following salient features:

- Dual-porosity media for all the three layers
- Convective type (diffusive flow) matrix-to-fracture fluid transfer for the U&L Shale reservoir
- Advective type (Darcy flow) matrix-to-fracture fluid transfer in the Middle Bakken reservoir
- U&L Shale OM pores dominate the fluid storage

The sensitivity-analysis, which was one of the deliverabilities of this research, required a tool to perform fast iterative calculations. Commercial reservoir simulators can handle high volumes of associated calculations and they are capable of delivering quick results at acceptable

accuracy levels. The nature of the research required compositional simulation, which prompted the use of CMG™'s compositional module GEM™.

4.1.1 Introduction to GEM™

According to the CMG™ documentation and user manual, GEM™ is a multi-dimensional, equation-of-state (EOS) compositional simulator, which accounts for both the thermodynamic and the fluid-flow aspects of the reservoir. It can be run in explicit, fully implicit and adaptive-implicit modes. It utilizes either the Peng-Robinson or the Soave-Redlich-Kwong equation-of-state to predict phase-equilibrium and fluid properties. It accomplishes coupling between the geomechanical model and the simulator in a modular and explicit way.

4.1.2 Assumptions and Simplifications

- The heterogeneities in the reservoir properties were ignored in this study for the limited scope of this research and non-availability of information.
- O'Brien, et al. (2012) reported that the hydraulic fracture height in a Montana Bakken well may extend from 190 to 450ft, which suggests the hydraulic fractures might extend throughout the three layers of the Bakken system, if not so, they at least were able to activate the naturally existing fractures in the U&L Shale.
- The three layers were stacked together, and there was no permeability-barrier to impair their connectivity
- There was no interference-effect from the nearby producing wells and the well confined its influence inside the stimulated reservoir volume (SRV)
- Geomechanical effects on porosity and permeability were neglected
- Water was considered to remain as an immobile phase at all times

4.1.3 Reservoir Simulation in Tight Reservoir

Contrary to the field-scale simulation practice in the conventional reservoirs, extremely tight reservoirs, such as the Middle Bakken, are simulated individually for each well. This simulation approach works satisfactorily as the wells barely communicate beyond their respective stimulated reservoir volume (SRV). Therefore, the interference-effect between the wells placed even in the same reservoir is a non-issue, until the SRVs of the two wells overlap

each other. Following the same convention, the simulation scheme adopted in this research had only one horizontal well, which is completed in the Middle Bakken reservoir.

4.2 Simulation Scheme

For this research, the three-layered Bakken system was emulated in a simplified prototype to study the implications of the proposed simulation scheme. The prototype consisted of three horizontal layers stacked together, in which the top and the bottom layers represented the U&L Shale and the central layer, placed in between them represented the middle-siltstone reservoir. Dual-porosity flow media was chosen for the simulation scheme and the associated flow equations and formulations are listed in Appendix E.

The simulator GEM™ accepts the data entry through the DAT file, which list the different data under the coded instruction-sets. These coded instructions serve like the communication language between the simulator and a DAT file, and as the simulators read the codes, the instruction-sets and different data are passed over to the simulator's run-module. The run-module then executes as per the instructions to deliver the output of the simulation. The different data-section of the DAT files are listed below:

1. Reservoir description
2. Component properties
3. Rock-fluid data
4. Initialization
5. Well and recurrent data

These data-sections in the DAT file for the adopted simulation scheme are discussed separately in detail in the following sections. It should be noted that the numerical values entered in the example DAT file is liable to change as per the simulation-run requirements.

4.2.1 Reservoir description

The reservoir description section in the DAT file specifies the gridding-scheme, block-dimensions, structural-top information, block-porosity, block-permeability, rock-compressibility data and flow-media type.

4.2.1.1 Gridding, Block-Dimensioning and Structural Top

Gridding: Figure 4.1 is a snapshot of the reservoir-data Section of the DAT file for the simulation scheme utilized in this research. The reservoir was divided into 40-blocks along the x-axis, 15-blocks along the y-axis and 11-blocks along the z-axis, which means there were in total 6600 $(40 \times 15 \times 11)$ cuboid-shaped grid-blocks. Along the z-axis, the top three (1^{st} to $3^{rd)}$ and the bottom three (8^{th} to 11^{th}) grid-layers represented the Upper and the Lower Bakken Shale respectively. The remaining five grid-layers (4^{th} to 8^{th}) represented the Middle Bakken layer.

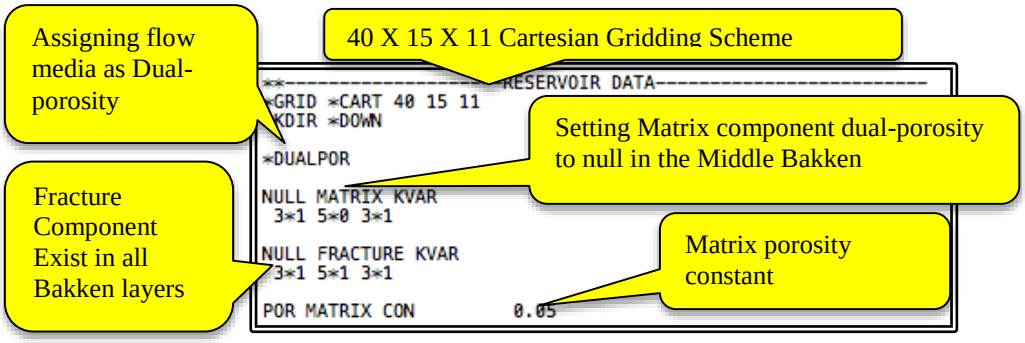

Figure 4.1: DAT file section for Cartesian gridding for the Bakken prototype. Matrix component of dual-porosity set to null.

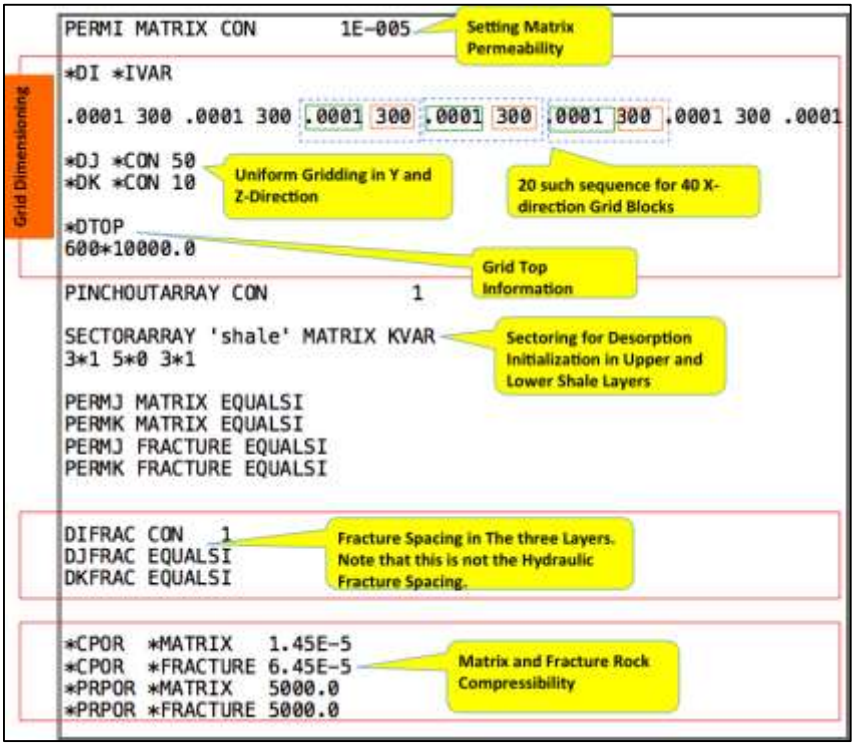

Figure 4.2: DAT file section for grid-block dimensioning and structural-top information, fracture spacing in the U&L Shale, and rock-compressibility data.

Block Dimensioning: The snapshot in Figure 4.2 starts with the grid-dimensioning information where each block was assigned the respective x, y and z lengths. There was a uniform-gridding along the y-axis (50ft) and z-axis (10ft). Along the x-axis, the gridding was not uniform and its thickness followed a specific alternating x-dimension to accommodate the hydraulic fracture planes.

Structural Top: The structural-top information (Figure 4.2) provided the depth to all the 600 (40×15) blocks of the upper-most grid-layers. The instruction specified that the reservoir-top was perfectly horizontal (x-y plane) and, situated at a depth of 10000ft depth.

4.2.1.2 Porosity, Permeability and Rock-Compressibility

Porosity and permeability: As it was mentioned in Section 4.1.2, the heterogeneity in reservoir properties such as porosity and permeability was ignored in the simulation scheme. Therefore, in the DAT file, the matrix porosity was specified as constant for all the grid-blocks, which is 5% (Figure 4.1). Similarly, the matrix permeability was specified as 0.00001md to all the grid-blocks. The fracture porosity and permeability values followed a specific pattern for the grid-blocks (Figure 4.4 and Figure 4.5).

Rock-Compressibility: The matrix and fracture components were given separate rock-compressibility values of 0.0000145 and 0.0000645 (1/psi) respectively. The reference pressure for the compressibility values was also specified at 5000psi.

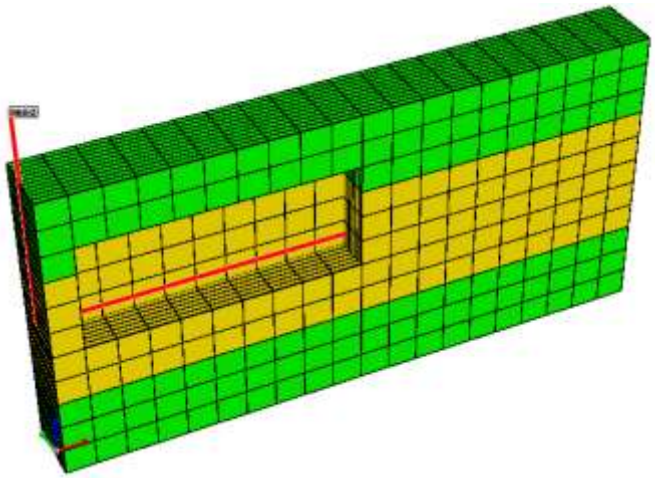

Figure 4.3: Grid-scheme's 3-D graphical representation. Three Bakken layers: U&L Shale shown in Green color and the Middle Layer shown in yellow. The horizontal well centrally penetrates through middle-layer.

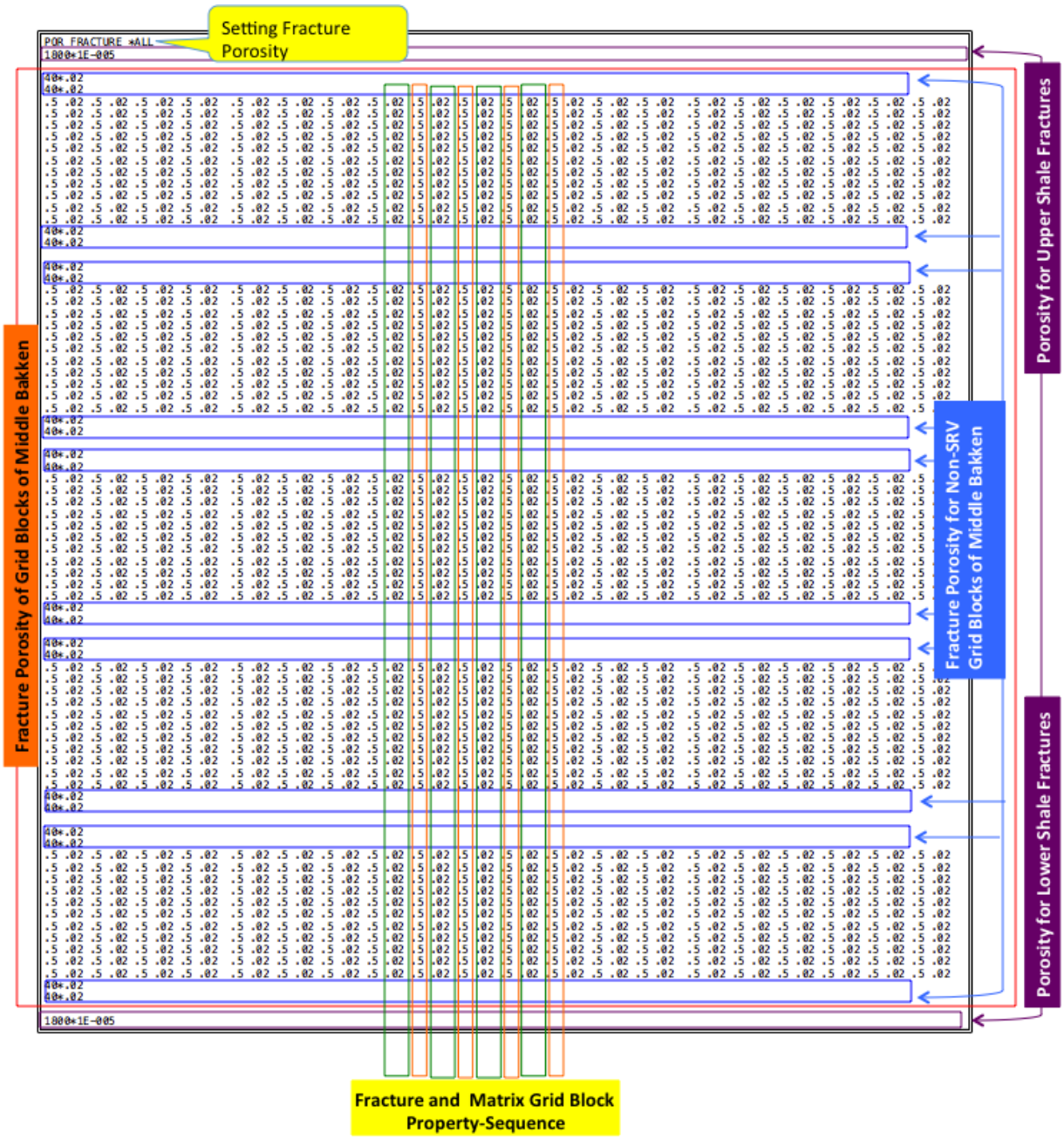

Figure 4.4: DAT file Section for the fracture porosity input.

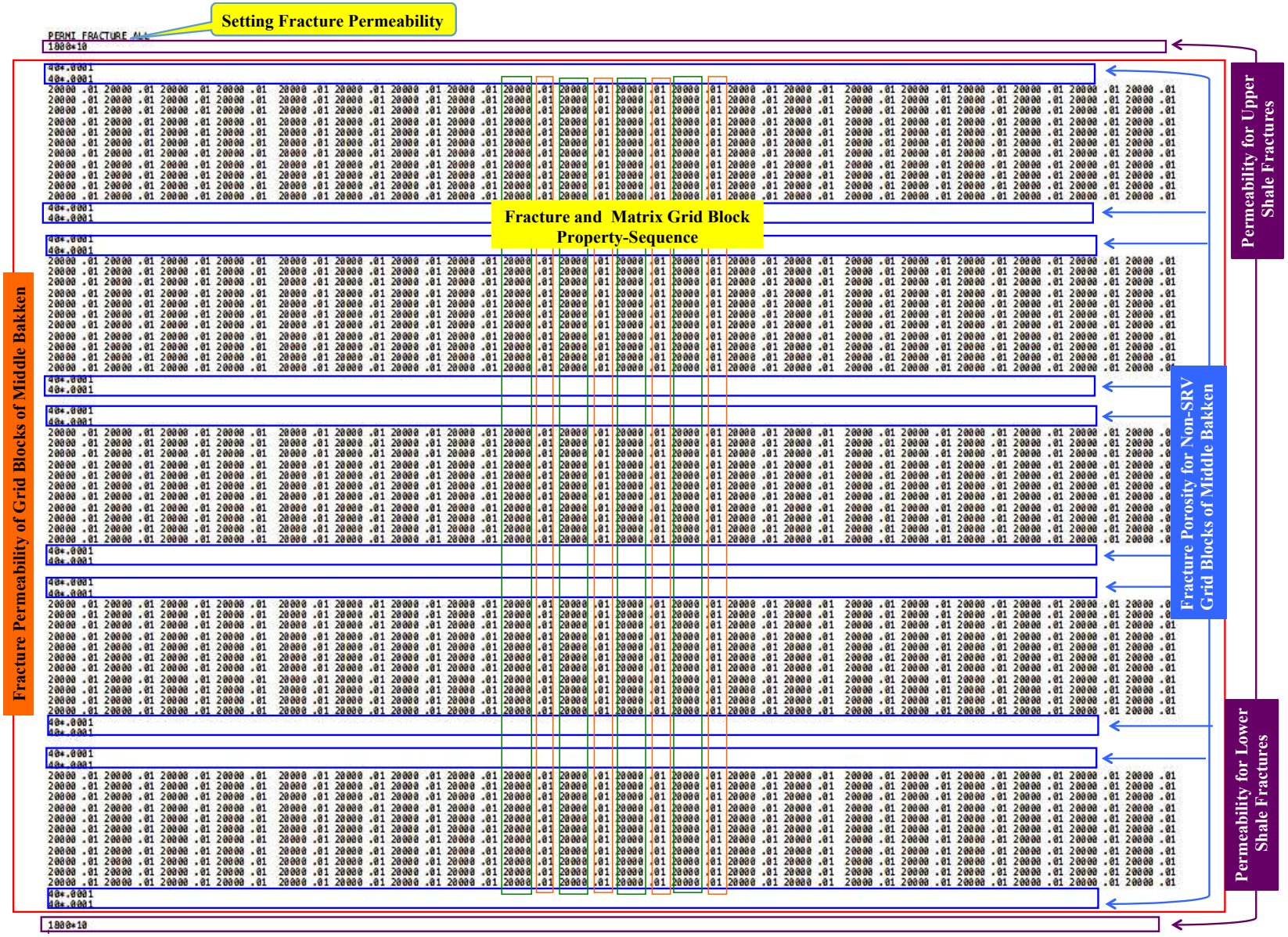

Figure 4.5: DAT file Section for fracture permeability input.

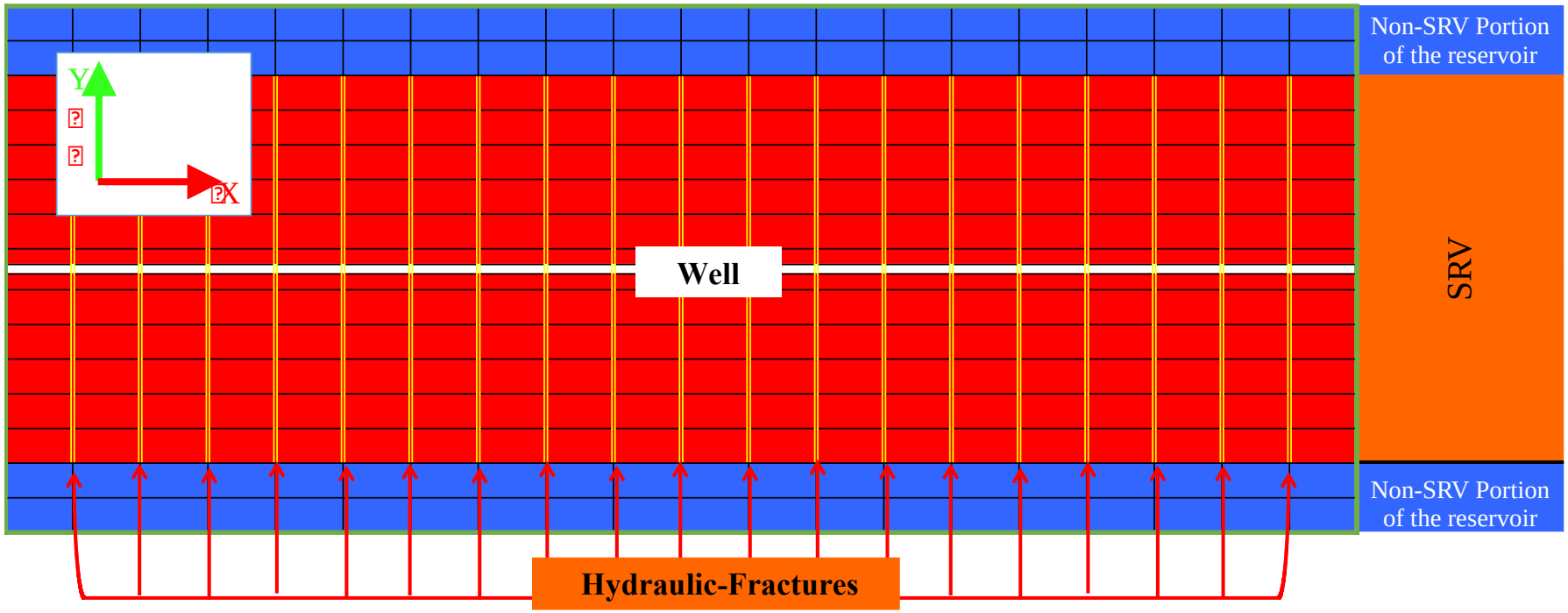

Figure 4.6: Top View of the gridding scheme.

4.2.1.3 Dual-porosity Media

As discussed in Section 2.2, dual-porosity media were expected in all the three Bakken layers. Section 2.2.1 and Section 2.2.2 described the theoretical difference between the dual-porosity media in the U&L Shale layers and that in the Middle Siltstone layer. The distinction was based on the matrix-to-fracture fluid transfer and fluid storage scheme. The U&L Shale were discussed to have the diffusive matrix-to-fracture and adsorption dominated fluid-storage in OM pores, whereas the middle layer was described to have Darcy matrix-to-fracture fluid transfer and conventional fluid storage in the pores.

Incorporating two different dual-porosity flow media in a single simulation-application was a challenge for this analysis, and to achieve it, special gridding-maneuvers and sectoring were performed. The following describes how this was accomplished in this research:

Dual-porosity in the Middle Bakken Layer: Snapshot in Figure 4.1 shows that the matrix-component of the dual-porosity media in the middle layer was set to null. Thus, the matrix-component of the dual-porosity media did not exist in the middle layer as reflected in the null space for the middle-layer in Figure 4.7.

As described in Section 2.2.2, the natural micro-fractures were expected to serve as the matrix, and the natural macro-fractures were and the hydraulic fractures were considered as the fracture-network of the Middle Bakken dual-porosity media. By altering the fracture porosity and fracture permeability values for some strategically located grid-blocks produced the desired matrix-component of the dual-porosity in this layer.

Snapshot in the Figure 4.2 shows that the x-axis lengths to the grids are assigned with twenty sequences of [0.0001 300] inputs, its interpretation in the geomodel can be explained by its top view in Figure 4.6. It shows the alternating sequences 300ft wide reservoir-blocks (red blocks) and 0.0001ft wide hydraulic fractures (yellow vertical-line). In conjugation with sequential alteration of fracture properties (porosity and permeability values) shown in snapshot in the Figure 4.4 and Figure 4.5, dual-porosity media was established in the middle layer. To be precise, the nineteen alternating 0.0001ft wide hydraulic fracture blocks (yellow lines in Figure 4.6) were assigned with a fracture-permeability of 10000mD and fracture-porosity of 0.5.

Whereas, the other twenty alternating 300ft wide blocks were assigned with the fracture-permeability of 0.01mD and fracture-porosity of 0.02, which made them serve as the matrix-component for the middle layer. Three-dimensional view in Figure 4.8, show the hydraulic-fracture as the nineteen parallel planes (red color), placed perpendicular to the x-axis, whereas the Middle Bakken matrix is shown in Figure 4.9.

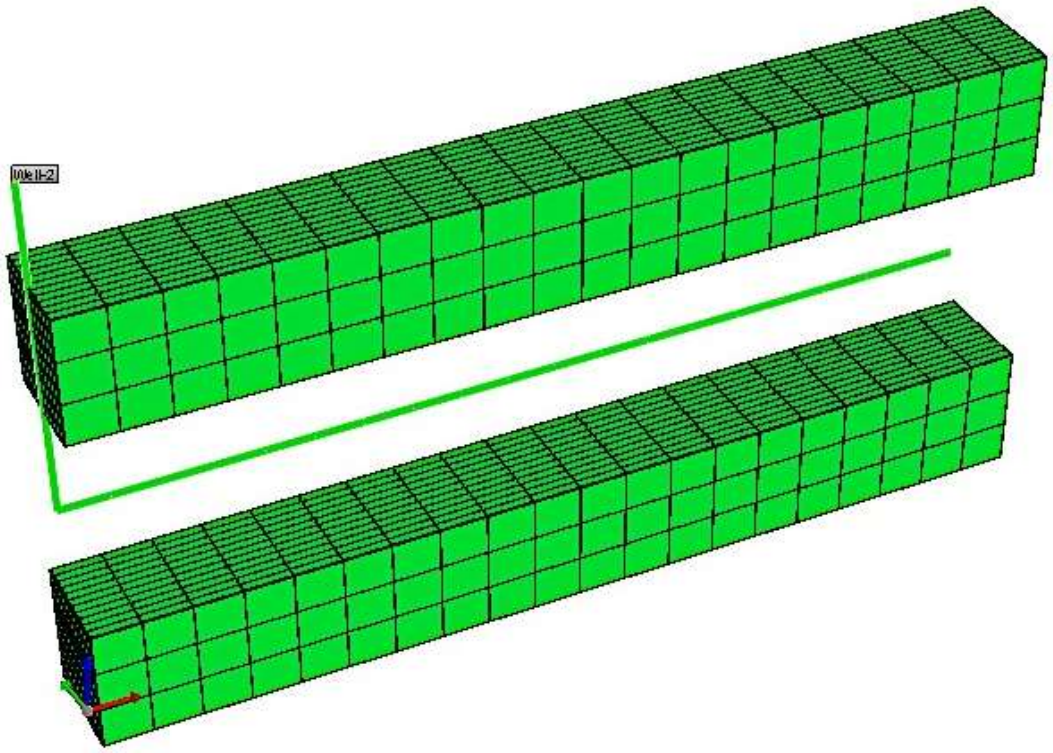

Figure 4.7: The space between two layers show that the matrix-component of the specified dual-porosity media in DAT file exists only in the U&L Shale layers.

This property-alteration sequence was not extended up to the U&L Shale layers, as these layers were assigned with the values associated with the respective shale-reservoir. For example, in Figure 4.4 uniform fracture-porosity and fracture-permeability of 0.001% and 10mD were assigned to the respective 1800 $(40 \times 15 \times 3)$ grid-blocks of the U&L Shale layers. However, the grid-dimensioning maneuvers were not restricted to the 3000 $((40 \times 15 \times 5)$ grid-blocks of the Middle Bakken layer only. However, it did not affect the U&L Shale behavior until their properties were constant in all the U&L Shale grid-blocks.

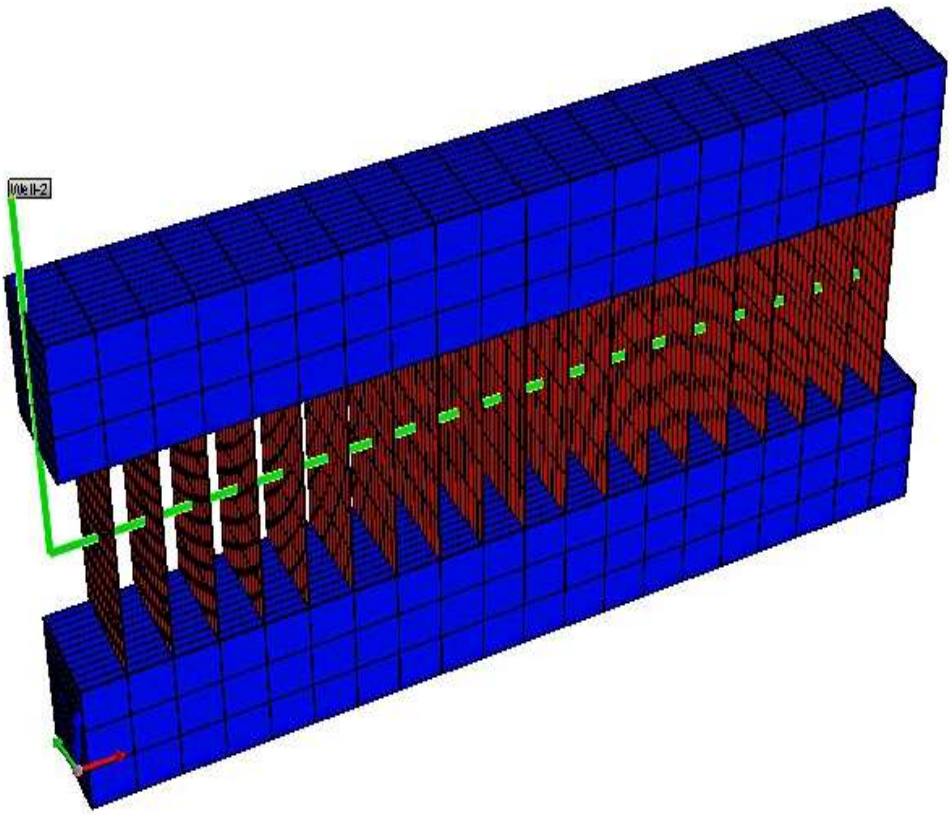

Figure 4.8: Fracture network in the three Bakken layers. The red vertical planes represent the hydraulic fracture of the Middle Bakken layer. The continuous blue grid-blocks represent the fracture porosity in the U&L Shale.

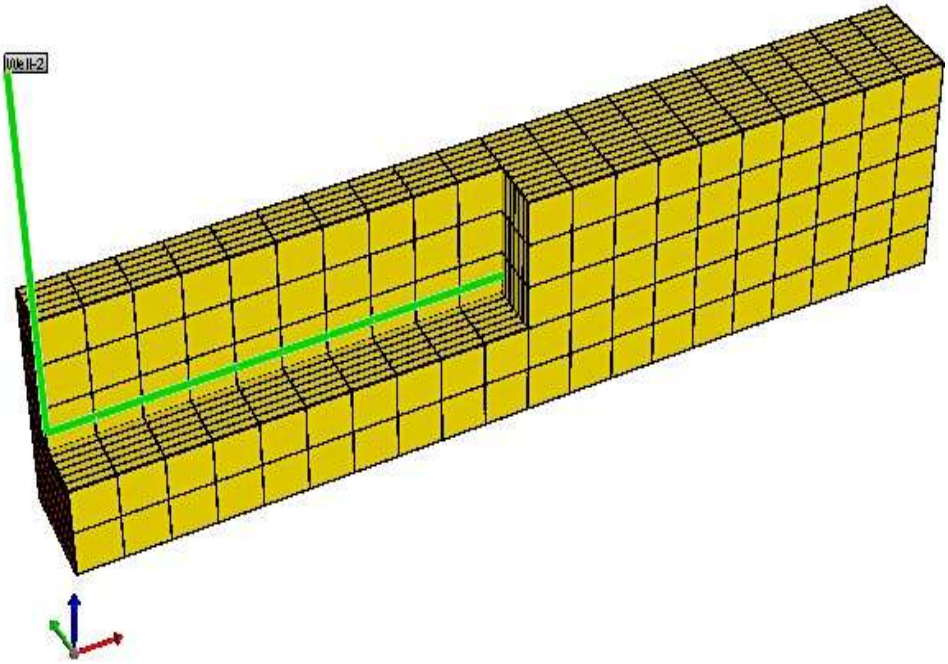

Figure 4.9: The Middle Bakken matrix in the simulation scheme.

Siltstone matrix had no active desorption, and the matrix-to-fracture fluid transfer was expected to be dominated by the pressure-gradient driven Darcy (advective) flow. The governing mathematical-equations are as follows (Kazemi, et al. 1976):

$$\tau_{jmf} = \sigma V \left(\frac{k_{rj}}{\mu_j}\right)(p_{jm} - p_{jf}) \tag{4.1}$$

Where,

$j = \text{phase (oil, gas, water)}$

$m = \text{matrix}$

$f = \text{fracture}$

$p = \text{pressure}$

$V = \text{gridblock volume}$

$$\sigma, \text{shape factor} = 4\left(kx/l_x^2 + ky/l_y^2 + kz/l_z^2\right) \tag{4.2}$$

$k = \text{fracture permeability}$

$l = \text{fracture spacing}$

Dual-porosity in the U&L Shale Layer: As discussed in Section 2.2.1, the OM pores in the U&L Shale had the adsorption-capacity to store the hydrocarbon fluid in their matrix. The natural and hydraulic fractures are expected to serve as the fracture-network component of the postulated dual-porosity media. The specified dual-porosity in the DAT file imparted its specialty only to the U&L Shale layers (Figure 4.7) and not to the middle layer, where dual-porosity was ensured with gridding-maneuvers. The Lx, Ly and Lz fracture spacing from the equation 4.2 for the dual-porosity media were specified as 1ft each. Note that, these are not the fracture-spacing for the multi-stage hydraulic-fractures; these fracture spacing represent an estimate of the natural fracture spacing in the U&L Shale layers.

The kerogen rich shale matrix was assumed to have offered the active multi-component desorption sites for the hydrocarbon-molecules. Once desorped, matrix-to-fracture transfer of these molecules was considerably dominated by the concentration-gradient driven diffusive (convective) flow, as discussed in Section 2.1.2. GEM™ offers to choose either free-gas or Langmuir's adsorbed gas molecular-concentration in the fracture and the matrix for diffusive

flow calculations. For this study, which entails multi-component desorption, Langmuir isotherms provided the concentration gradient for each component. The following equations describe the diffusive transfer in such cases:

$$Q_{LM,k} = V * [\sigma * D_{eff,k}] * F(S_g) * (LM_{k,m} - LLM_{k,f}) \quad (4.3)$$

Where,

V = Cell volume

σ = Shape factor

$D_{eff,k}$= Diffusion value for the k^{th} species

$F(S_g)$ = Function of fracture gas saturation, modeling water blocking

$LM_{k,m}$= Extended Langmuir isotherm for k^{th} species, multiplied by rock-density, evaluated at matrix composition and pressure

$LM_{k,m}$= Extended Langmuir isotherm for k^{th} species, multiplied by rock-density, evaluated at matrix composition and pressure

4.2.2 Fluid Components

Fluid-properties data input section specifies the particulars of the different hydrocarbons components present in the reservoir fluid. It also includes the Langmuir isotherm constants and diffusion-coefficients for the components.

4.2.2.1 Representative Fluid

GEM™ requires component-wise thermodynamic-constants, which can be produced with fluid PVT modeling software, such as WINPROP™. Reservoir fluid composition is determined utilizing the laboratory PVT analysis of a representative fluid sample. For this project, a representative fluid sample was not available; therefore, an appropriate composition for the fluid was chosen to be consistent with above the bubble-point pressure GOR. The chosen fluid consisted of 40% Methane, 40% Normal Hexane and 20% Normal Dodecane. A WINPROP™ generated P-T phase-diagram for the chosen fluid is shown in Figure 4.10. It should be noted here that the chosen mixture might not be a true representative of the reservoir fluid, but it was a reasonable compromise for the qualitative nature of this research.

The snapshot in Figure 4.11 shows the fluid PVT data input in the DAT file. The Peng-Robinson equation-of-state (Peng and Robinson 1976) is used for the flash calculations (Appendix E), which requires the thermodynamic-coefficients of the components. For the three components, WINPROP™ was utilized to generate these coefficients and they are included at the end of fluid PVT section.

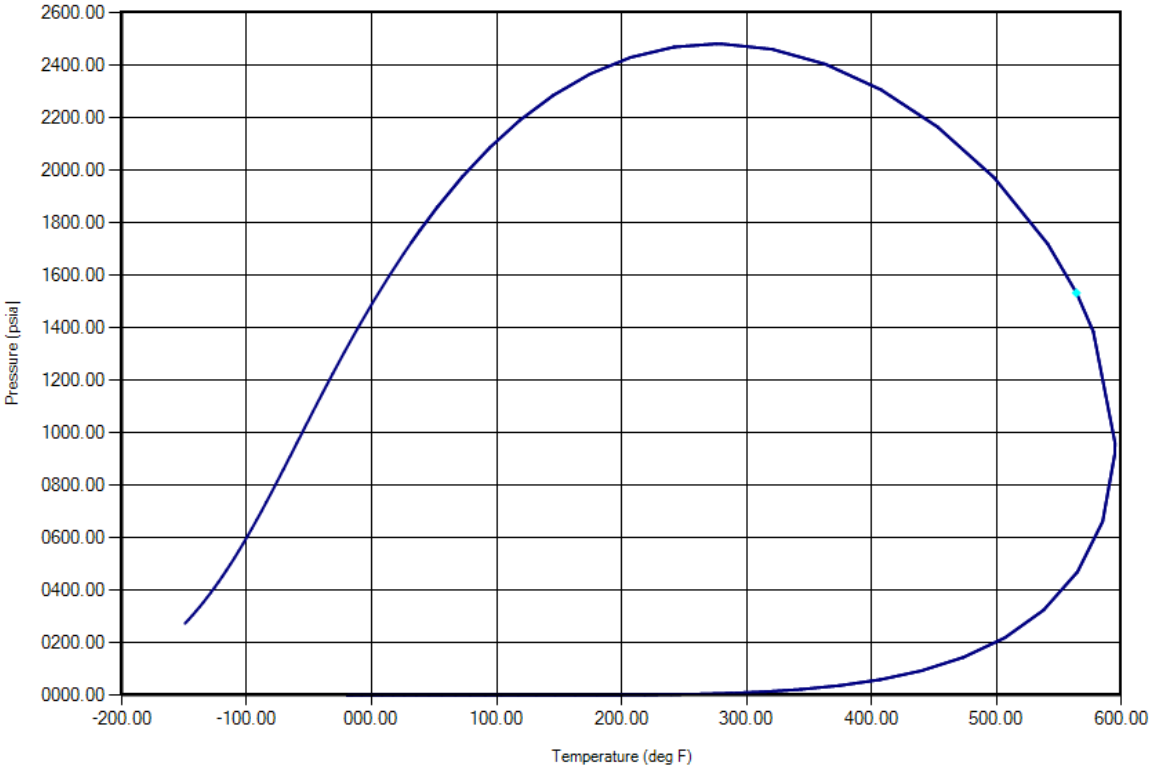

Figure 4.10: P-T diagram for the chosen fluid showing two-phase envelope for the fluid.

4.2.2.2 Multi-component Desorption

QUICKCBM™ module of BUILDER™ was utilized to produce desorption and diffusion input data (Figure 4.12) in the DAT file. GEM™ follows the extended Langmuir isotherm for multi-component adsorption (Arri, et al. 1992), which was described in Section 2.2.2. It uses Equation 2.3 to calculate component-concentrations in the matrix (U&L Shale matrix) the matrix-to-fracture fluid transfer term using Equation 4.3.Figure 4.13 shows the Langmuir isotherm for the multicomponent desorption data in the DAT file. The separate isotherm for three components (Methane, Hexane and Dodecane) represent the varying degree of desorption in the U&L Shale matrix over the different ambient pressures.

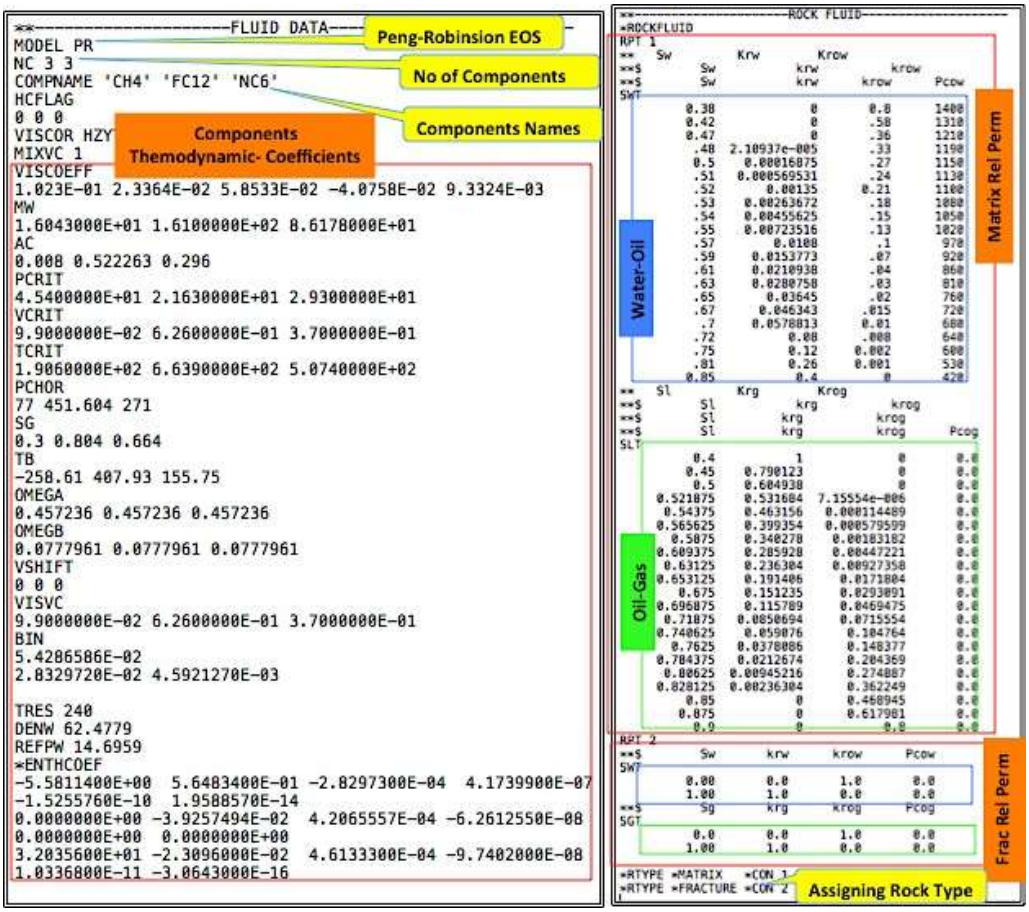

Figure 4.11: DAT file Section showing the fluid PVT data, and the relative permeability tables.

```
**----------FLUID DATA----------
MODEL PR
NC 3 3
COMPNAME 'CH4' 'FC12' 'NC6'
HCFLAG
0 0 0
VISCOR HZY
MIXVC 1
VISCOEFF
1.023E-01 2.3364E-02 5.8533E-02 -4.0758E-02 9.3324E-03
MW
1.6043000E+01 1.6100000E+02 8.6178000E+01
AC
0.008 0.522263 0.296
PCRIT
4.5400000E+01 2.1630000E+01 2.9300000E+01
VCRIT
9.9000000E-02 6.2600000E-01 3.7000000E-01
TCRIT
1.9060000E+02 6.6390000E+02 5.0740000E+02
PCHOR
77 451.604 271
SG
0.3 0.804 0.664
TB
-258.61 407.93 155.75
OMEGA
0.457236 0.457236 0.457236
OMEGB
0.0777961 0.0777961 0.0777961
VSHIFT
0 0 0
VISVC
9.9000000E-02 6.2600000E-01 3.7000000E-01
BIN
5.4286586E-02
2.8329720E-02 4.5921270E-03

TRES 240
DENW 62.4779
REFPW 14.6959
*ENTHCOEF
-5.5811400E+00  5.6483400E-01 -2.8297300E-04  4.1739900E-07
-1.5255760E-10  1.9588570E-14
0.0000000E+00 -3.9257494E-02  4.2065557E-04 -6.2612550E-08
0.0000000E+00  0.0000000E+00
3.2035600E+01 -2.3096000E-02  4.6133300E-04 -9.7402000E-08
1.0336800E-11 -3.0643000E-16
```

```
**----------ROCK FLUID----------
*ROCKFLUID
RPT 1
**   Sw        Krw        Krow
**$       Sw         krw        krow       Pcow
SWT
      0.38          0        0.8       1400
      0.42          0        .58       1310
      0.47          0        .36       1210
       .48  2.10937e-005        .33       1190
       0.5    0.00016875        .27       1150
       .51    0.00056953        .24       1130
       .52       0.00135       0.21       1100
       .53    0.00263672        .18       1080
       .54    0.00455625        .15       1050
       .55    0.00723516        .13       1020
       .57        0.0108         .1        970
       .59     0.0153773        .07        920
       .61     0.0210938        .04        860
       .63     0.0280758        .03        810
       .65       0.03645        .02        760
       .67      0.046343       .015        720
         .7     0.0578813       0.01        680
       .72          0.08        .008        640
       .75          0.12       0.002        600
       .81          0.26       0.001        530
      0.85           0.4           0        420
**   Sl        Krg        Krog
**$       Sl         krg        krog
**$       Sl         krg        krog
**$       Sl         krg        krog       Pcog
SLT
       0.4           1           0         0.0
      0.45    0.790123           0         0.0
       0.5    0.604938           0         0.0
  0.521875    0.531684  7.15554e-006         0.0
   0.54375    0.463156   0.00011489         0.0
  0.565625    0.399354   0.00057599         0.0
    0.5875    0.340278    0.0018318         0.0
  0.609375    0.285928    0.0044722         0.0
   0.63125    0.236304    0.0092736         0.0
  0.653125    0.191406     0.017188         0.0
     0.675    0.151235     0.029389         0.0
  0.696875    0.115789     0.046948         0.0
   0.71875   0.0850694     0.071555         0.0
  0.740625    0.059076     0.104764         0.0
    0.7625   0.0378086     0.148377         0.0
  0.784375   0.0212674     0.204369         0.0
   0.80625  0.00945216     0.274887         0.0
  0.828125  0.00236304     0.362249         0.0
      0.85           0     0.468945         0.0
     0.875           0     0.617981         0.0
       0.9           0          0.8         0.0
RPT 2
**$       Sw         krw        krow       Pcow
SWT
         0.0         0.0         1.0         0.0
         1.0         1.0         0.0         0.0
**$       Sg         krg        krog       Pcog
SGT
         0.0         0.0         1.0         0.0
         1.0         1.0         0.0         0.0
*RTYPE *MATRIX   *CON 1
*RTYPE *FRACTURE *CON 2
```

Figure 4.12: Snapshot of the DAT file showing the QUICKCBM™ generated desorption and diffusion input data.

```
**----------DESORPTION AND DIFFUSION----------
ADGMAXC 'FC12' MATRIX CON 5.97862E-007
ADGMAXC 'FC12' FRACTURE CON            0
ADGMAXC 'CH4' MATRIX CON    0.0418503
ADGMAXC 'CH4' FRACTURE CON            0
ADGMAXC 'NC6' MATRIX CON   0.00418503
ADGMAXC 'NC6' FRACTURE CON            0
ADGCSTC 'CH4' MATRIX CON       0.0005
ADGCSTC 'CH4' FRACTURE CON            0
ADGCSTC 'FC12' MATRIX CON       0.0005
ADGCSTC 'FC12' FRACTURE CON            0
ADGCSTC 'NC6' MATRIX CON       0.0005
ADGCSTC 'NC6' FRACTURE CON            0
ROCKDEN MATRIX CON          250
ROCKDEN FRACTURE CON          250
COAL-DIF-COMP 'CH4' CON         0.05
COAL-DIF-COMP 'FC12' CON       1E-005
COAL-DIF-COMP 'NC6' CON        0.001
```

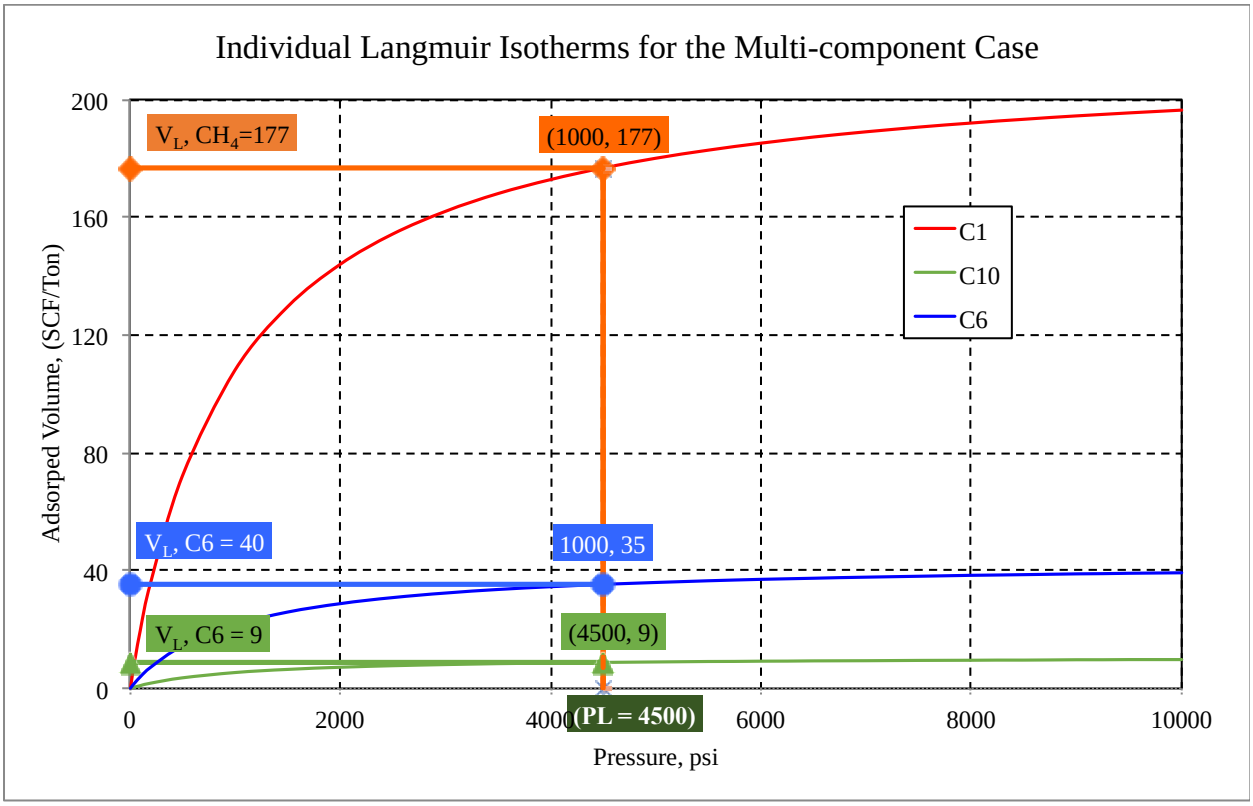

Figure 4.13: Sample Langmuir isotherm for the simulation scheme.

4.2.3 Rock-fluid Data

For this project, relative-permeability tables were not available for the Middle Bakken, and the U&L Shale flow media. However, CMG™ offers an alternative to generate the relative-permeability curves for a variety of lithology utilizing the following set of correlations:

$$k_{rw} = k_{rwiro} * \left({(S_w - S_{wcrit})} \Big/ {(1.0 - S_{wcrit} - S_{oirw})} \right)^{N_w} \quad (4.4)$$

$$k_{row} = k_{rocw} * \left({(S_o - S_{orw})} \Big/ {(1.0 - S_{wcon} - S_{orw})} \right)^{N_{ow}} \quad (4.5)$$

$$k_{rog} = k_{rogcg} * \left({(S_l - S_{org} - S_{wcon})} \Big/ {(1.0 - S_{gcon} - S_{org} - S_{wcon})} \right)^{N_{og}} \quad (4.6)$$

$$k_{rg} = k_{rgcl} * \left(\frac{(S_g - S_{gcrit})}{(1.0 - S_{gcrit} - S_{oirg} - S_{wcon})} \right)^{N_{og}} \quad (4.7)$$

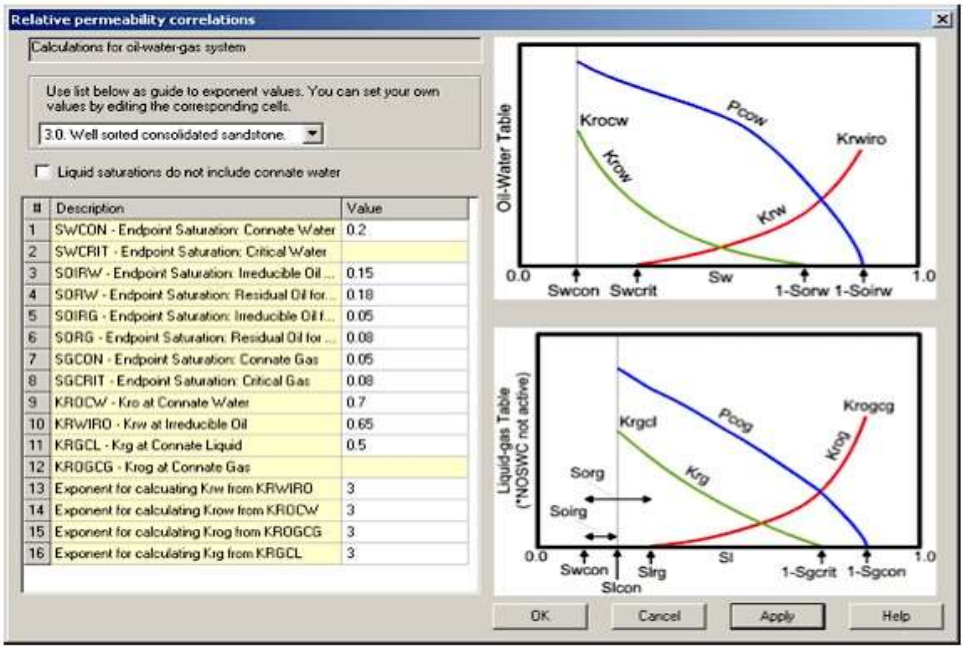

Figure 4.14: Correlation dialogue box in CMG™'s module BUILDER™ for relative permeability-curve generation.

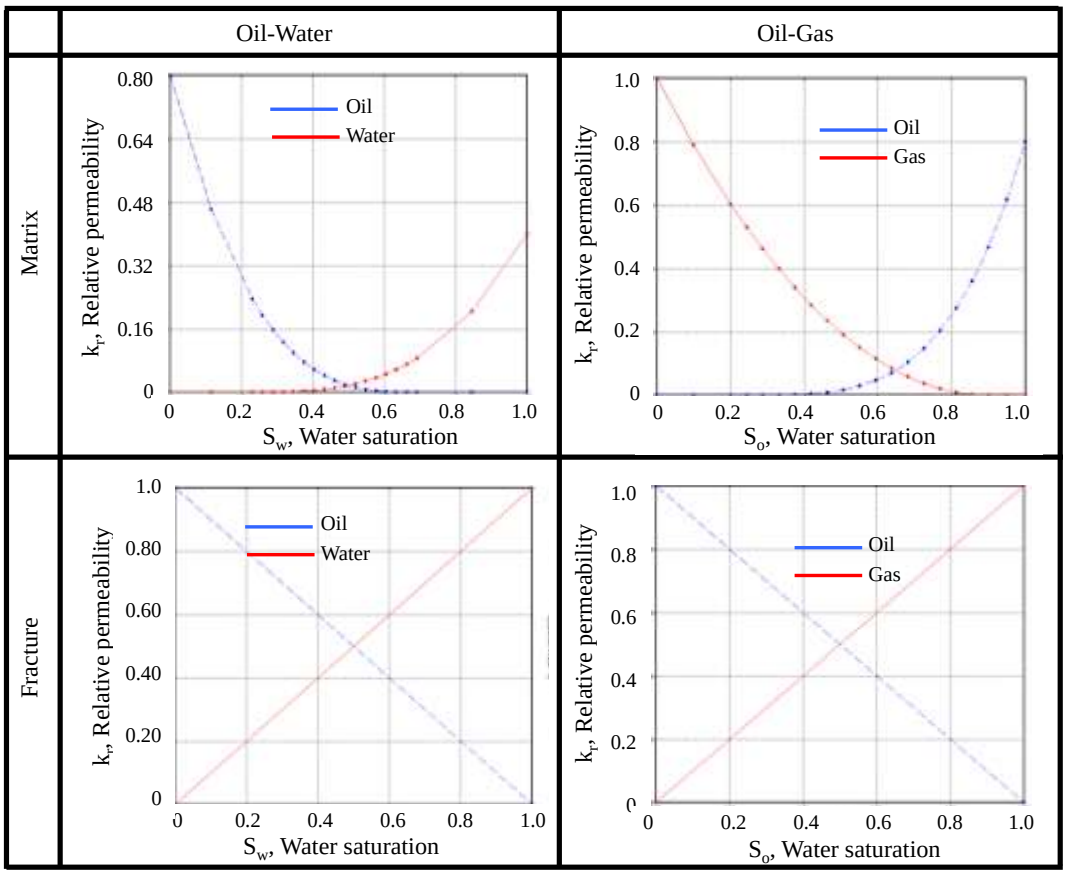

Figure 4.15: Relative-permeability curves for matrix and fracture-network.

The terms appearing in the equations are maximum attainable relative permeability, critical and residual saturations for the water, oil and gas phases. These parameters are listed in relative-permeability correlation dialogue box (Figure 4.14). Two sets of relative-permeability curves were generated for the matrix and fracture flow media (Figure 4.15). It should be emphasized here that these curves might not represent the Bakken porous media. However, the effect on the simulation results could be compromised considering the qualitative nature of this research.

In the DAT file, the relative permeability data was entered within the rock-fluid section. The snapshot in the right side of the Figure 4.11 shows the water-oil and oil-gas relative permeability tables for two rock-types 1 and 2. At the end of this input section, the two rock-types were assigned to the matrix and fracture-network.

4.2.4 Initial Conditions

GEM™ offers eight different initialization schemes for the equilibrium-calculation during the onset of a simulation-run. For this study, the vertical-block-centered-composition initialization scheme was chosen to include desorption in the flow calculations. This initialization scheme sets the composition-vector at the geometrical center of the grid blocks. Utilizing this composition, gravity-capillary equilibrium calculations evaluate the initial pressure and water-saturation for each grid-block. S_o and S_g are subsequently calculated using the flash calculations (Appendix E).

The two separate initialization regions, named as 1 and 2 are assigned to the matrix and fracture flow media. The water-oil contact depth (10,200ft) and reference pressure (6500psi) at the datum (10,030ft) are specified for both the initialization regions. A table of global composition (0.4, 0.2 and 0.4 for Methane, Dodecane and Hexane) for both the initialization regions is provided at a reference depth (10,000ft).

4.2.5 Well and Recurrent Data

The right side of Figure 4.16 shows input scheme for well data in the DAT file. A constant flowing bottom-hole pressure of 1000psi is set as the operating constraint for the well. A 0.25ft radius horizontal well is placed along the x-axis and the skin is set to zero around the wellbore. The well is symmetrically placed in the Middle Bakken layer and the multi-staged

hydraulic fractures for the well was same as discussed in Section 4.2.1.1. The perforations in the well exclusively belong to the hydraulic fracture blocks as shown in Figure 4.17.

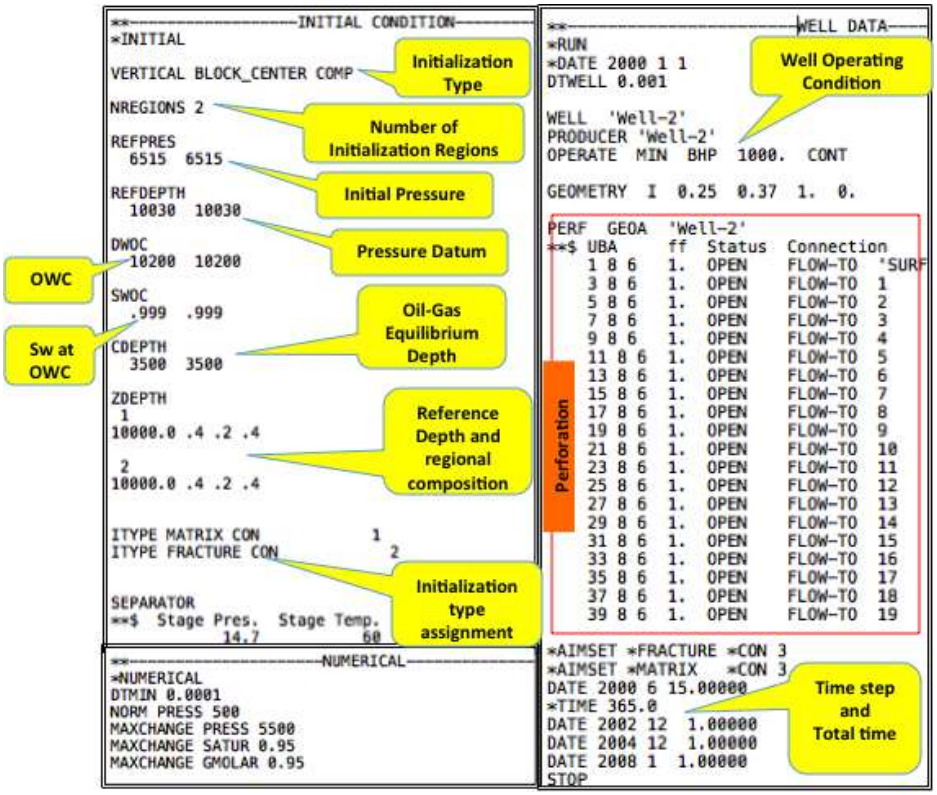

Figure 4.16: DAT file Section for Initialization, numerical control and well data.

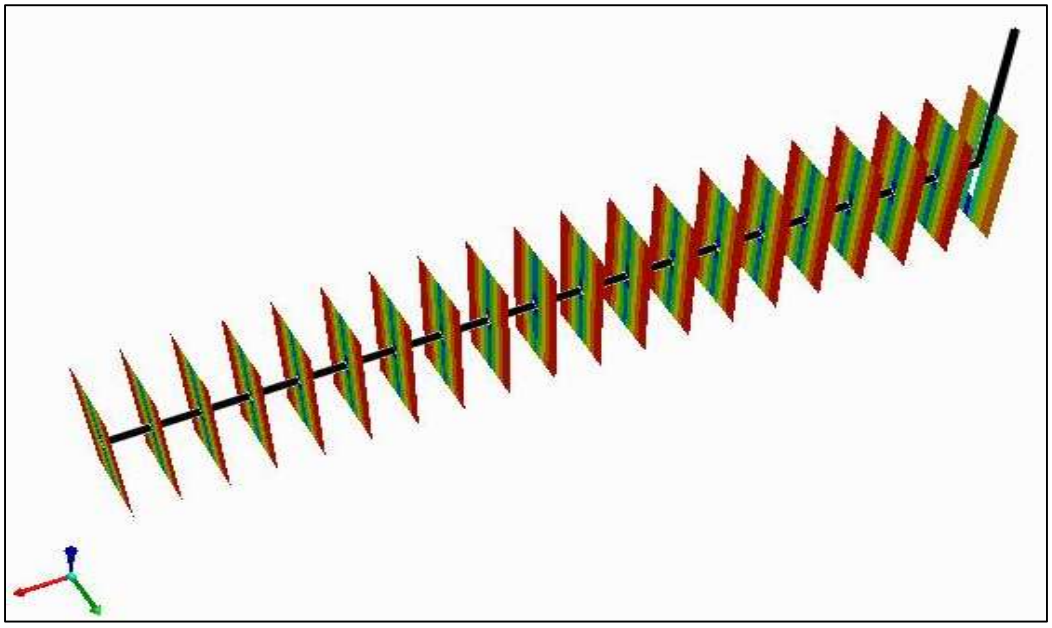
Figure 4.17: Multi-stage transverse fracturing along the horizontal well path.

4.2.5.1 Well-bore Formulation

Wellbore fluid-flow modeling is crucial in determining the flow capacity of a well. In case of long laterals, the frictional pressure loss along the horizontal Section critically affects the well performance. GEM™ accounts for this frictional and hydraulic pressure loss in the flow tubing using the following set of equations:

$$\Delta P = \Delta P_H - \Delta P_{KE} - \Delta P_F \quad (4.8)$$

Where,

$\Delta P_H = \rho g \Delta z$ (Hydrostatic head over the length Δz)

ρ: fluid density

g: Acceleration due to gravity

$\Delta P_{KE} = -\rho v^2 \ln\left(\frac{P_2}{P_1}\right)$ (Kinetic energy gain)

v: Fluid velocity

P_2: Upstream Pressure

P_1: Downstream Pressure

$\Delta P_F = \frac{2fv^2\rho}{D}\Delta Z$ (Frictional energy loss)

f: roughness

D: Pipe hydraulic diameter

For this project, the fluid density (ρ) was assumed to be 0.15 psi/ft and the production-tubing relative roughness (f) was chosen to be 0.02. The equation (included below) is a mathematical-representation of well-to-reservoir tying. The flow rates of phase j (j = o, g, w) at reservoir conditions is given by (Peaceman, 1983, 1987):

$$Q_j = \sum_l PI_{j,l}\left({k_r}/{\mu}\right)_{j,L}\left(p_{o,i} - p_{bh}\right) \quad (4.9)$$

$$PI_j = 2\pi kh\,{wfrac}\Big/\left\{\ln\left({r_e}/{r_w}\right) + S\right\} \quad (4.10)$$

Where,

Q_j: Production rate of the phase j

$PI_{j,l}$: Well Index of Ith grid well for the phase j

k_r: relative permeability of the phase j

μ: visosity of phase j

$p_{o,i}$: Oil phase pressure in the grid block I

p_{bh}: Well bore pressure

k: absolute permeability

h: perforation length

wfrac: radialfraction of the well drainage area

r_e: Effective drainage radius of the well grid $-$ block

r_w: Well radius

S: Skin

CHAPTER 5

RESULTS AND INTERPRETATION

This chapter presents the results of this research, which included the quantification of the anticipated production contribution from the Upper and Lower (U&L) Bakken Shale to the Middle Bakken reservoir. A simulation scheme was developed in Chapter 4, which was utilized to quantify the proposed contribution. The results for this quantification are illustrated through various type-curves, which show the effect of variation in different parameters on the shale contribution. The findings of the simulation-based quantification are concluded with a Tornado-chart, which demonstrates the relative sensitivity of the different parameters to the cumulative-production contribution from the horizontal well, described in Section 4.2.5.

5.1 Parameters Values and Range

This research was aimed at improving the present understanding of the production contribution from the U&L Shale to the Middle Bakken reservoir. Therefore, it was essential to identify those parameters, which control the process of the anticipated contribution. The simulation scheme developed in Chapter 4 was utilized to derive quantitative results for the shale production-contribution as a function of these parameters. However, deriving meaningful quantitative results from the simulation scheme were contingent on the validity of the chosen range and values for these input parameters. These parameters could be categorized in three main groups. The following outlines the various sources for the numerical values of these parameters.

5.1.1 U&L Shale Properties

Diffusion Coefficients: As discussed in Section 2.1.2, organic rich shales (ORS) are expected to have several components for the diffusion coefficient, which may include components from Fickian-diffusion, Knudsen diffusion, diffusion through the kerogen bulk, the surface diffusion and the liquid diffusion. It should be emphasized here that the determination of parameters such as the diffusion coefficient for the molecular flow in shale requires rigorous laboratory procedures, which was beyond the scope of this project. Moreover, no research pertaining to such analyses for the U&L Shale are reported in the literature. However, an analogy

can be drawn from the contribution of Fathi and Akkutlu (2009) and Yan, et al. (2013), in which they reported the cumulative diffusivity flow-component for methane in several ORSs and suggested that their values lie in the loose range of 1.0 to10^{-5} cm^2/sec. Considering that, the range for methane diffusivity in this study was selected as 0.5-.005 cm^2/sec.

In addition, the multi-component desorption and diffusion scenario prevailing in this study required diffusivity for other components as well. Chen and Chen (2008) reported the binary-diffusion coefficients of bi-molecular methane-hexane, methane-octane and methane-decane mixtures. The study suggested that the diffusion coefficients for each of the molecule-types lies within the same order of magnitude. For for the mole fraction of the chosen reservoir fluid (40% Methane, 20% Dodecane and 40% Hexane), using the curves in Figure 5.2 the diffusion coefficient for Hexane and Dodecane were calculated as half and a quarter respectively of that of methane.

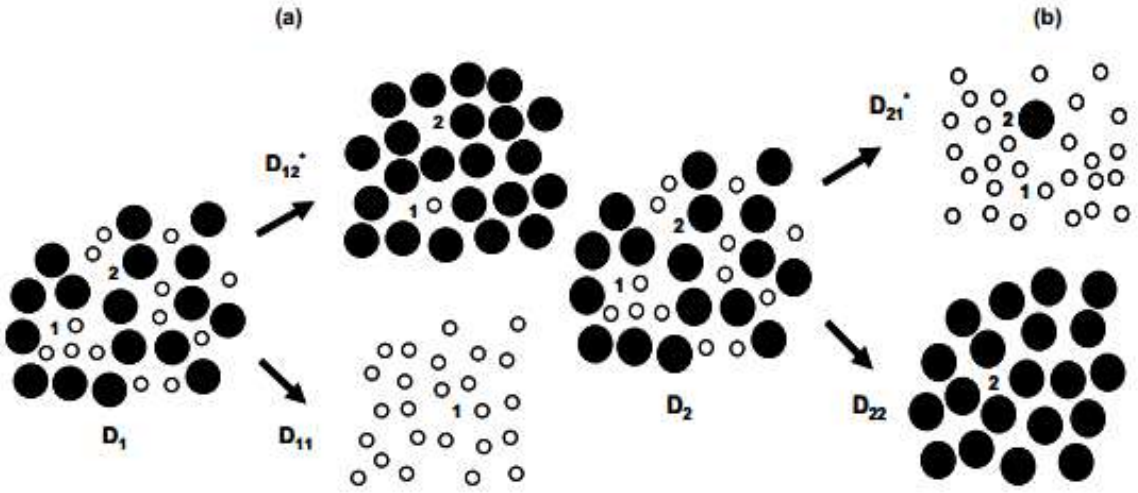

Figure 5.1: Schematic diagram showing the rule of mixing for self-diffusivity of the two components in a mixture (Chen and Chen 2008).

TOC and Langmuir isotherm: Schmoker and Hester (1983) conducted a comprehensive study to report the areal distribution of TOC in the U&L Bakken Shale. Figure 5.3 shows the isopach maps for the two shale layers, on which 159 distinct TOC sampling-points are shown with dots. The vast spread of the chosen sampling-points ensured the reliability of the TOC data. The histograms in Figure 5.3 show the statistical distribution of TOC (wt.%) values for both the shale layers.

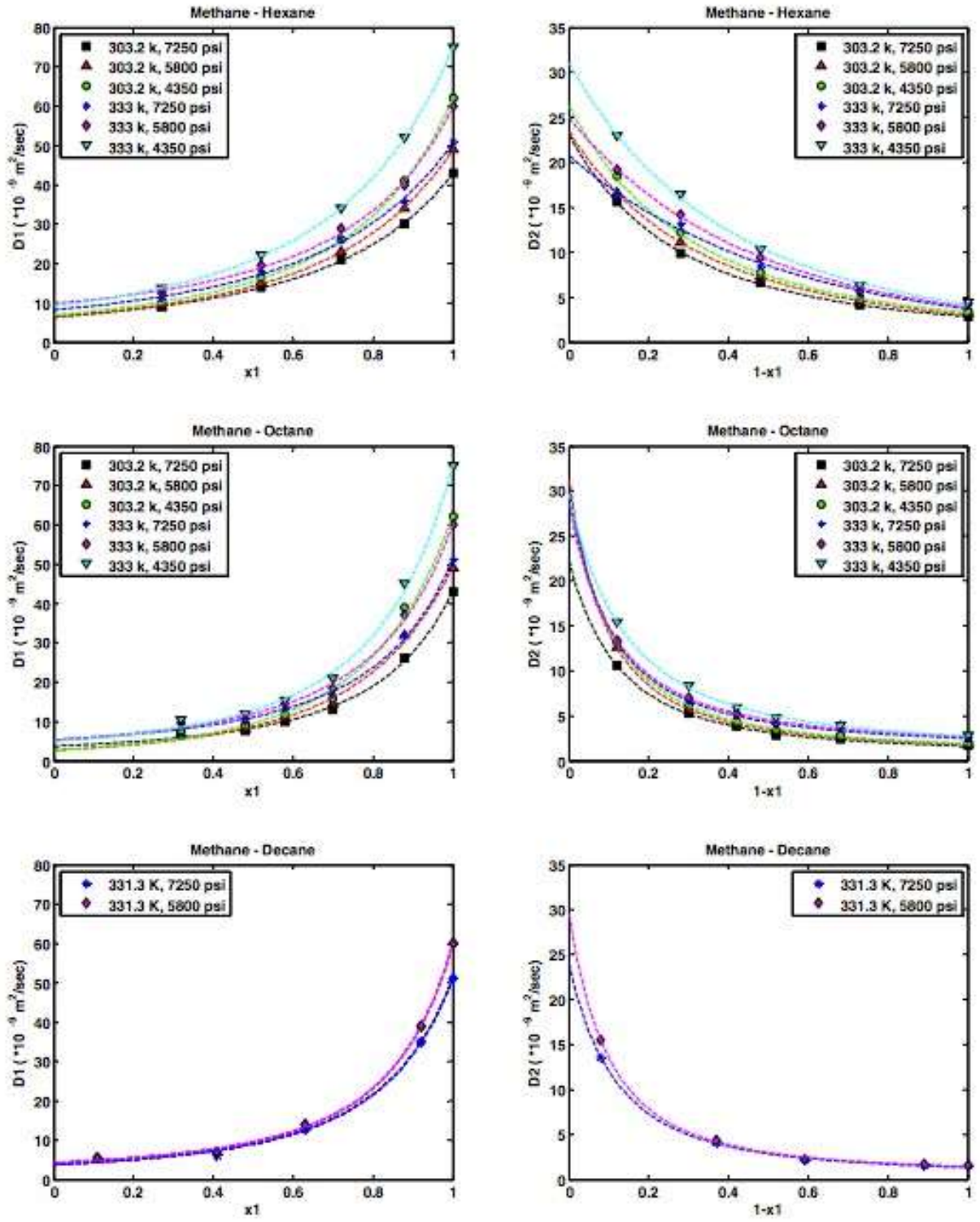

Figure 5.2: Bi-molecular mixture and the diffusion coefficients for methane, hexane, octane and decane molecules (Chen and Chen 2008).

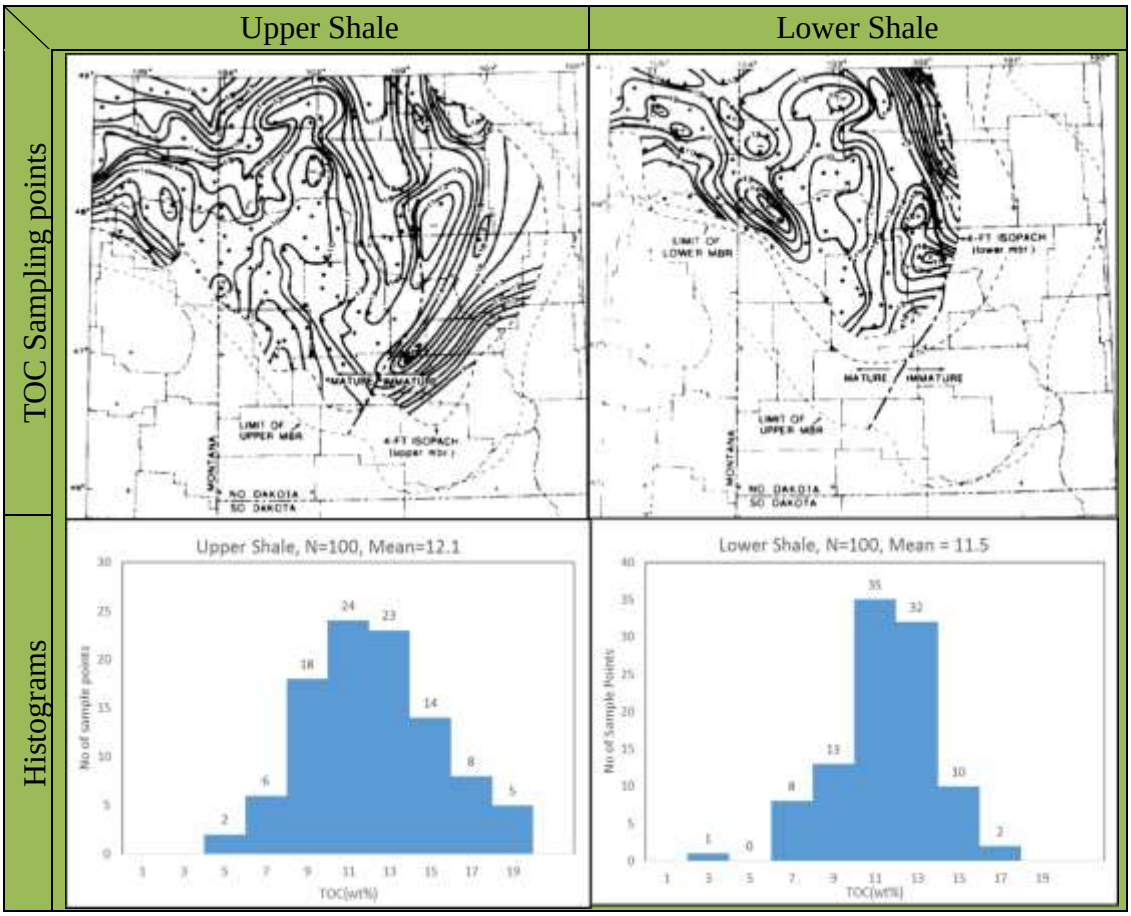

Figure 5.3: Total organic arbon distribution in the U&L Shale (Schmoker and Hester 1983).

As discussed in Section 2.6, TOC values of the U&L Bakken Shale layers are expected to control their adsorption storage-capacities. The same section also included a stepwise scheme, based on the contribution of Zhang, et al. (2012) and Lewis, et al. (2004), to evaluate the Langmuir isotherm parameters for a given TOC values. Using the same, Table 5.1 and Table 5.2 tabulate the values of the minimum, maximum and mean values of the two isotherm parameters evaluated at different values of TOC reported by Schmoker and Hester (1983).

Table 5.1: Table for Langmuir's constant, K evaluation utilizing the steps discussed in Section 2.6.

Kerogen Type	1/K (Psi) @ 65°C	C8 (Lewis Correlation Constant)	1/K (Psi) @ 115.6°C
Type 1	1343	2.803	2404
Type 2	1062	2.701	1901

Table 5.2: Table for Langmuir's adsorption capacity, V_{max} evaluation utilizing the steps of Section 2.6.

		TOC	V_{max}	C4 (Lewis Correlation Constant)	V_{max}
Upper Shale	Max	19	192	2.4	113
	Min	6	68	1.9	40
	Mean	12.18	127	2.2	75
Lower Shale	Max	17	173	2.3	102
	Min	3	39	1.7	23
	Mean	11.58	121	2.2	71

Table 5.3: The range, the average values and the source of the Middle Bakken reservoir parameters (Dechongkit and Prasad 2011).

Parameters	Symbol	Values		Average	References
		From	To		
Initial reservoir pressure (psia)	P	4,060	7,325	5,700	Cramer (1986) and Wang et al. (2010)
Reservoir temperature (F)	T	175	250	210	Kuhn et al. (2009)
Oil API gravity (degree API)	API	39	45	2,300	Breit et al. (1992)
Gas specific gravity	γ_g	0.77	0.88	0.83	Breit et al. (1992)
Bubble-point pressure (psia)	P_b	1,730	2,900	2,300	Breit et al. (1992) and Clark (2009)
Initial water saturation (decimal)	S_{wi}	0.20	0.50	0.35	Bohrer et al. (2008)
Water salinity (ppm)	Sal	2,000	471,000	237,000	Palombi et al. (2006)
Porosity (decimal)	ϕ	0.01	0.16	0.09	Pitman et al. (2001)

5.1.2 Middle Bakken Properties

The primary reservoir input parameters for the middle layer were derived from the study of Dechongkit and Prasad (2011). In the research, the authors surveyed various literatures pertaining to the Middle Bakken reservoir and reported the range of the primary reservoir parameters as shown in Table 5.3. It should be noted here that not all of the Middle Bakken parameters listed in Table 5.3 were used as the sensitivity-analysis variables. In this study, parameters, other than those included in the Middle Bakken properties category in Table 5.4, were maintained as constant at their respective average values.

5.1.3 Hydraulic fracture parameters

Fracture Spacing: Fracture spacing in a transverse multi-stage fracturing scheme is largely a completion design issue. O'Brien, et al. (2012) reported the frequently utilized completion scheme in the Elm Coulee Field, in which the fractures are ensured to lie at 400-500ft intervals (Figure 5.4). For this project, this range was made more inclusive by broadening it by another 100ft. The finalized range for the Middle Bakken hydraulic-fracture spacing was 350-550ft, and the most probable value was chosen as 450ft.

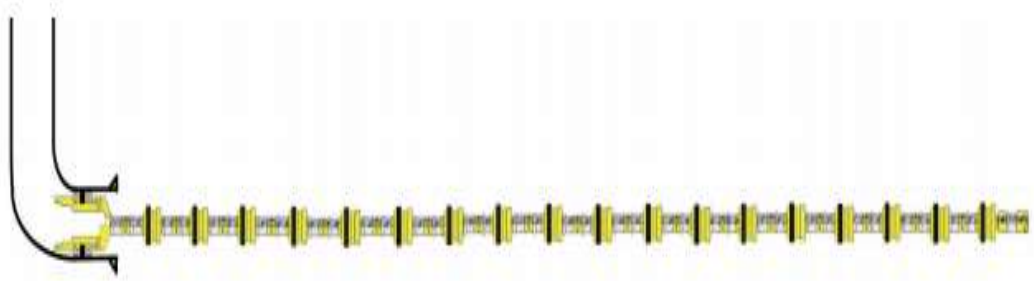

Figure 5.4: Multiple stage transverse hydraulic fracturing job in the Elm Coulee field achieved by using Hydraulic packers and frac-sleeves at the 400-500ft interval for zonal isolation and frac-diversion (O'Brien, et al. 2012).

Fracture Half-length: Fracture half-length (FHL) is not a premeditated or planned parameter. It is controlled by the unknown factors such as the local stress-field setting in the reservoir and the presence of localized faults. Therefore, advanced techniques such as microseismic survey based discrete-fracture-network modeling or well-test analysis are utilized to determine the FHL. On the basis of a microseismic study, O'Brien, et al. (2012) reported an average FHL as 450ft for a Middle Bakken well in the Elm Coulee field. The upper limit was mentioned as 900ft. For the sensitivity analysis a range of 250-750ft was chosen and the most expected value was chosen as 450ft.

5.2 Sensitivity Analysis Scheme

This study suggests that with the range of parameters listed in Table 5.4, the contribution from the U&L Shale might be accounted for 10-50% of the cumulative production from the Middle Bakken reservoir. This section outlines the procedure adopted for the quantification of this range for contribution-percentage. In the course of this study, multiple iterations were performed on the simulation scheme, which was discussed in Chapter 4. The outputs of the

simulation-run were oil rate, cumulative oil production and gas-oil-ratio (GOR) performance plots.

A total 6561 different combinations and equal numbers of iterations for simulation-runs were possible with three different values (minimum, mean and maximum) of the eight sensitivity analysis parameters. For each simulation-run, the evaluation of U&L Shale contribution required equal number of iterations under the non-contribution scenario, in which the U&L Shale were not contributing. To conduct a descriptive sensitivity analysis, there could be numerous schemes to shortlist the most effective cases among these 6561 iteration. However, for this research, the following scheme was utilized for this purpose.

Table 5.4: The eight finalized sensitivity analysis parameters and their range for sensitivity analysis.

Category	Parameters	Unit	Min	Max	Mean	Source
U&L Shale Properties	TOC	%	3	20	11	(Schmoker and Hester 1983)
	D	cm^2/sec	0.005	.5	0.05	(Chen and Chen 2008)
	Fracture Perm	md	0.1	10	1	Appropriately Chosen
	Fracture Spacing	feet	5	10	15	Appropriately Chosen
Middle Layer Properties	Matrix Porosity	fraction	0.02	0.04	0.05	(Dechongkit and Prasad 2011)
	Matrix Permeability	md	0.001	0.1	0.01	(Sonnenberg and Pramudito 2009)
HF Properties	HF Spacing	feet	350	550	400	(O'Brien, et al. 2012)
	Fracture Half Length	feet	250	750	750	(O'Brien, et al. 2012)

Contribution-case iterations: Sensitivity analysis for a particular parameter was performed by varying it to the assigned minimum, mean and maximum values, and all other parameters were set at their mean values. Non-contribution case iterations: To determine the U&L Shale contribution, the non-contribution case results for each of the contribution-case iterations were derived by setting the fracture permeability (k_f) of the Upper and Lower Shale to zero and keeping other parameters unchanged. The sensitivities of the eight parameters listed in Table 5.4 to the anticipated U&L Shale production contribution are being evaluated. Certain iterations utilizing the combination of the parameter-values are required to be performed to derive simulation results for the sensitivity analysis. Those iterations, and their corresponding

combinations of the parameter-values are listed in Table 5.5. The first case is when each parameter is set to its mean values (Iteration #1). Since, there are two iterations each for the minimum and maximum values of the eight sensitivity analysis parameters, which makes a total of other sixteen iterations (#2 to #17).

Table 5.5: The first seventeen combinations for variation in parameter values, others are for no-contribution cases. Blue, white and red cells represent the maximum, mean and the minimum values for the parameters in a specific iteration. Note that iteration #1NC to #9NC, circled with the red broken line represent the same case.

Iteration type	Parameters	Iteration #	(TOC, D, Kf, Lx, Φm, Km, FHL, HFS)	TOC	D	Kf	Lx	Φm	Km	FHL	HFS
Contribution Case	Mean	1	*(MD, MD, MD, MD, MD, MD, MD, MD)*	11	0.050	1.0	10	4%	0.010	450	450
	U&L Shale	2	*(MN, MD, MD, MD, MD, MD, MD, MD)*	3	0.050	1.0	10	4%	0.010	450	450
		3	*(MX, MD, MD, MD, MD, MD, MD, MD)*	20	0.050	1.0	10	4%	0.010	450	450
		4	*(MD, MN, MD, MD, MD, MD, MD, MD)*	11	0.005	1.0	10	4%	0.010	450	450
		5	*(MD, MX, MD, MD, MD, MD, MD, MD)*	11	0.500	1.0	10	4%	0.010	450	450
		6	*(MD, MD, MN, MD, MD, MD, MD, MD)*	11	0.050	0.1	10	4%	0.010	450	450
		7	*(MD, MD, MX, MD, MD, MD, MD, MD)*	11	0.050	10.0	10	4%	0.010	450	450
		8	*(MD, MD, MD, MN, MD, MD, MD, MD)*	11	0.050	1.0	5	4%	0.010	450	450
		9	*(MD, MD, MD, MX, MD, MD, MD, MD)*	11	0.050	1.0	15	4%	0.010	450	450
	Middle Layer	10	*(MD, MD, MD, MD, MN, MD, MD, MD)*	11	0.050	1.0	10	2%	0.010	450	450
		11	*(MD, MD, MD, MD, MX, MD, MD, MD)*	11	0.050	1.0	10	6%	0.010	450	450
		12	*(MD, MD, MD, MD, MD, MN, MD, MD)*	11	0.050	1.0	10	4%	0.001	450	450
		13	*(MD, MD, MD, MD, MD, MX, MD, MD)*	11	0.050	1.0	10	4%	0.100	450	450
	Hydraulic Frac	14	*(MD, MD, MD, MD, MD, MD, MN, MD)*	11	0.050	1.0	10	4%	0.010	250	450
		15	*(MD, MD, MD, MD, MD, MD, MX, MD)*	11	0.050	1.0	10	4%	0.010	750	450
		16	*(MD, MD, MD, MD, MD, MD, MD, MN)*	11	0.050	1.0	10	4%	0.010	450	350
		17	*(MD, MD, MD, MD, MD, MD, MD, MX)*	11	0.050	1.0	10	4%	0.010	450	550
Non-Contribution Case	Mean	1NC	*(MD, MD, ZERO, MD, MD, MD, MD, MD)*	11	0.050	0	10	4%	0.010	450	450
	U&L Shale	2NC	*(MN, MD, ZERO, MD, MD, MD, MD, MD)*	3	0.050	0	10	4%	0.010	450	450
		3NC	*(MX, MD, ZERO, MD, MD, MD, MD, MD)*	20	0.050	0	10	4%	0.010	450	450
		4NC	*(MD, MN, ZERO, MD, MD, MD, MD, MD)*	11	0.005	0	10	4%	0.010	450	450
		5NC	*(MD, MX, ZERO, MD, MD, MD, MD, MD)*	11	0.500	0	10	4%	0.010	450	450
		6NC	*(MD, MD, ZERO, MD, MD, MD, MD, MD)*	11	0.050	0	10	4%	0.010	450	450
		7NC	*(MD, MD, ZERO, MD, MD, MD, MD, MD)*	11	0.050	0	10	4%	0.010	450	450
		8NC	*(MD, MD, ZERO, MN, MD, MD, MD, MD)*	11	0.050	0	5	4%	0.010	450	450
		9NC	*(MD, MD, ZERO, MX, MD, MD, MD, MD)*	11	0.050	0	15	4%	0.010	450	450
	Middle Layer	10NC	*(MD, MD, ZERO, MD, MN, MD, MD, MD)*	11	0.050	0	10	2%	0.010	450	450
		11NC	*(MD, MD, ZERO, MD, MX, MD, MD, MD)*	11	0.050	0	10	6%	0.010	450	450
		12NC	*(MD, MD, ZERO, MD, MD, MN, MD, MD)*	11	0.050	0	10	4%	0.001	450	450
		13NC	*(MD, MD, ZERO, MD, MD, MX, MD, MD)*	11	0.050	0	10	4%	0.100	450	450
	Hydraulic Frac	14NC	*(MD, MD, ZERO, MD, MD, MD, MN, MD)*	11	0.050	0	10	4%	0.010	250	450
		15NC	*(MD, MD, ZERO, MD, MD, MD, MX, MD)*	11	0.050	0	10	4%	0.010	750	450
		16NC	*(MD, MD, ZERO, MD, MD, MD, MD, MN)*	11	0.050	0	10	4%	0.010	450	350
		17NC	*(MD, MD, ZERO, MD, MD, MD, MD, MX)*	11	0.050	0	10	4%	0.010	450	550

MD=Mean, MN=Minimum, MX=Maximum, B=Base

Additionally, for the quantification of the U&L Shale production contribution for the seventeen iterations (#1 to #17), equal numbers of non-contribution case iterations (# 1NC to # 17NC) are also performed. For iterations #1NC to #9NC, k_f is set to zero, ensuring that there is no fluid flow in the U&L Shale. Therefore, the values of U&L Shale parameters (TOC, D, k_f and L_x) are expected not to affect the results for such non-contribution iterations. These iterations resulted in the same output for all their simulation-runs. For other non-contribution case iterations (#10NC to #17NC), results for simulation-runs are different from each other.

5.3 Sensitivity Analysis Results and Analysis

The sensitivity study results and their analysis are presented for eight parameters through separate sets of type-curves. For the sensitivity study of a particular parameter, the three simulation results for the minimum, mean and maximum values were plotted over two different type-curves. The first type-curve contained the three performance-plots each for the oil rate and cumulative oil responses for the minimum, mean and maximum values of that particular parameter. The second type curve plotted the three GOR versus time response for the three different values of the parameters. Plotting them together enabled analyzing the effect of these parameters on the time bound performance. Each of these type curves also included non-contribution case results to assist in interpreting the U&L Shale production contribution.

5.3.1 The U&L Shale Parameters Sensitivity

The contribution-case simulation-results for the maximum and minimum values of the U&L Shale parameters were generated using Iteration #2 to #9. The simulation result for Iteration #1 was included in each of the sensitivity studies to represent the mean value results for each parameter. The non-contribution cases were generated utilizing Iteration #1NC to #9NC. As stated earlier, the simulation outcome for these iterations are essentially the same, which explained the the existence of a single non-contribution case response on the type curves.

5.3.1.1 Total Organic Carbon

The rate and cumulative oil type-curve for the TOC (weight %) variation are shown in Figure 5.6(a). Output from of Iteration #1 to #3 were utilized for the contribution case results.

The results for non-contribution case were derived from Iteration #1NC to #3NC, which were essentially the same and appeared as a single curve over the type-curves.

There was an indication of proportionality between the degree of stabilization in the oil rate and the values of TOC (%). Enhancement in the cumulative oil performance curves also refelect the positive impact of an increase in the TOC (%) on the deliverability of the reservoir. Figure 5.6(b) shows the GOR performance type-curves for TOC (%). In comparision the the non-contribution case, GOR seemed to get subdued at later stages of production as the TOC (%) increased, which also explains the anomalous trends recorded for actual wells in the Bakken (Section 2.6).

5.3.1.2 Diffusion Coefficient

The diffusivity of the components controls the critical matrix-to-fracture transfer in the U&L Shale. Diffusion can be either concentration driven or even density difference driven due to change in pressure (Figure 5.5). It has the same implication on fluid transportation in a shale matrix as the permeability has in a conventional reservoir. Therefore, an increase in the components diffusivity coefficients was expected to enhance the matrix-to-fracture fluid transfer in U&L Shale and thereby increase their production contribution. The type-curves for diffusivity are shown in Figure 5.7 (a) and (b), which indicated the enhancement in production as the diffusivity of methane and other components increased.

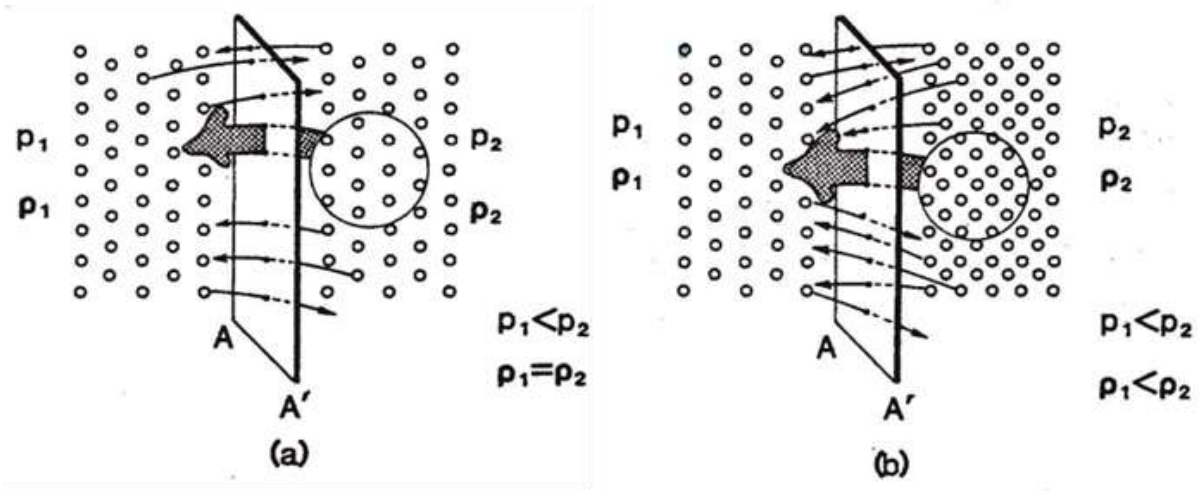

Figure 5.5: Phenomenon of self-diffusion through a plane across which the change in concentration is attributed to either (a) change in pressure only or, (b) change in both pressure and density (Ertekin, et al. 1986).

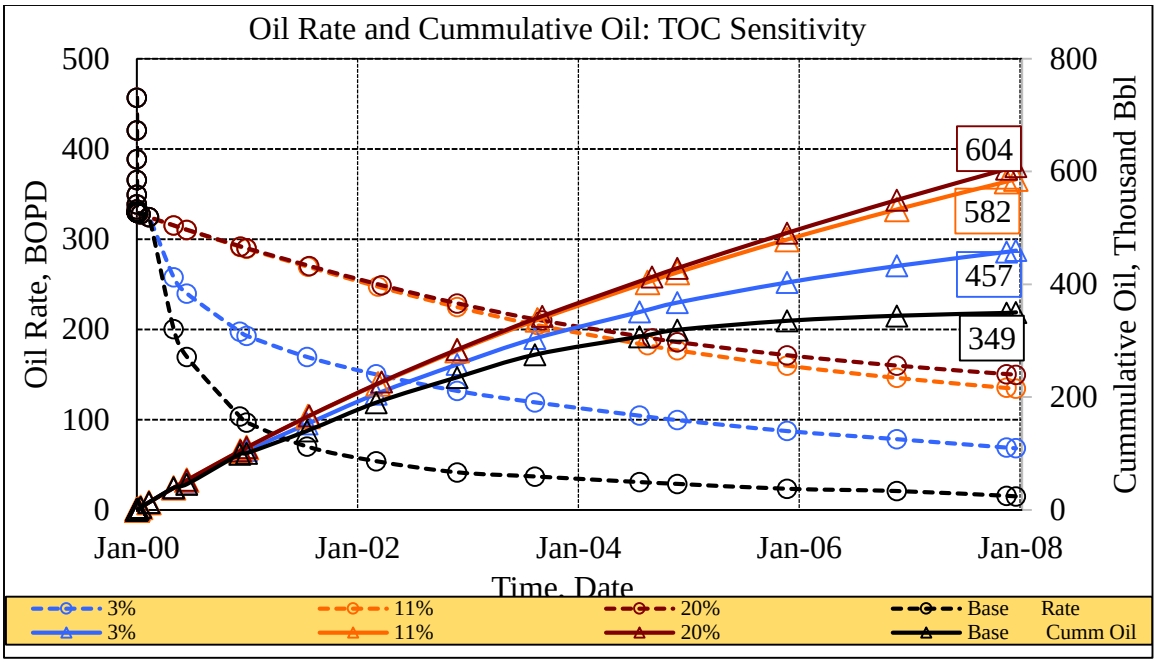

(a)

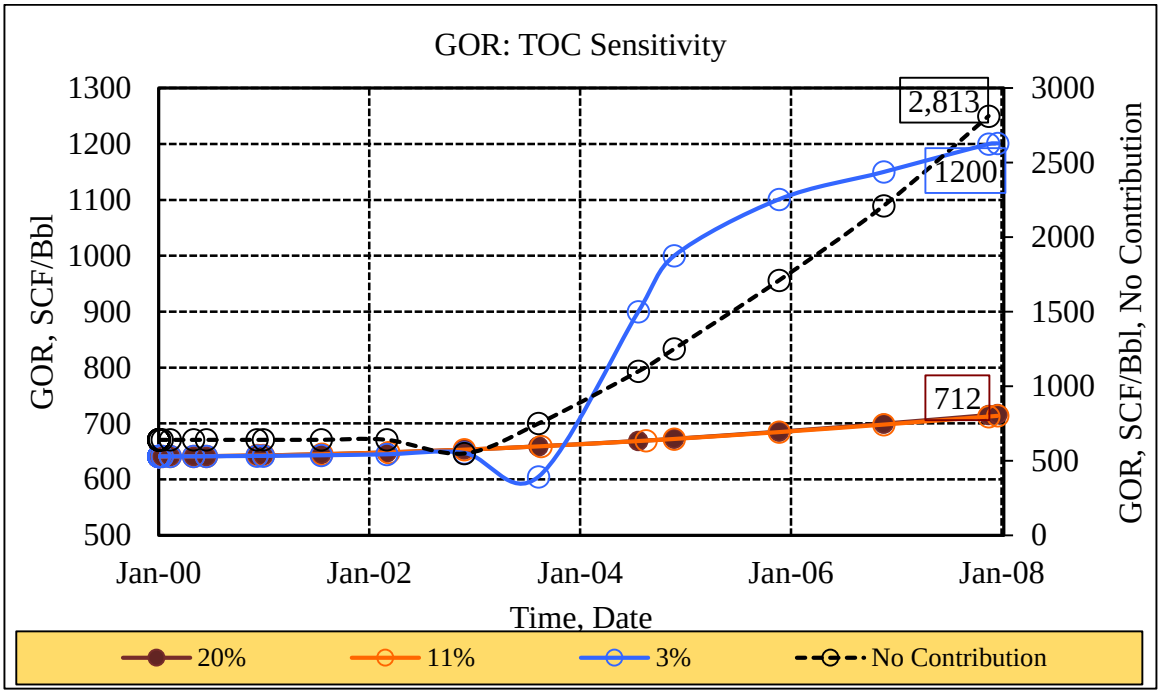

(b)

Figure 5.6: (a) Rate and cumulative oil performance type-curves for total organic carbon variation in the Upper and Lower Shale. The data-labels show cumulative oil in thousand barrel in the eighth year of production. (b) Gas-Oil ratio performance plot for total organic carbon variation. The data-labels show gas-oil ratio in SCF/Bbl in the eighth year of production.

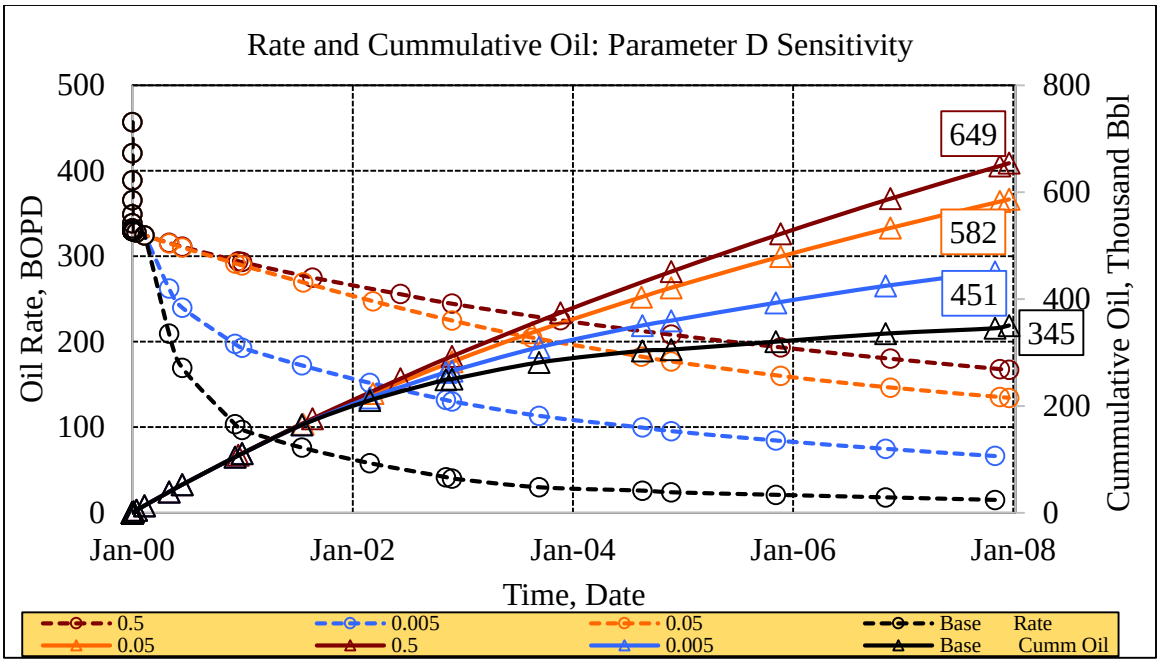

(a)

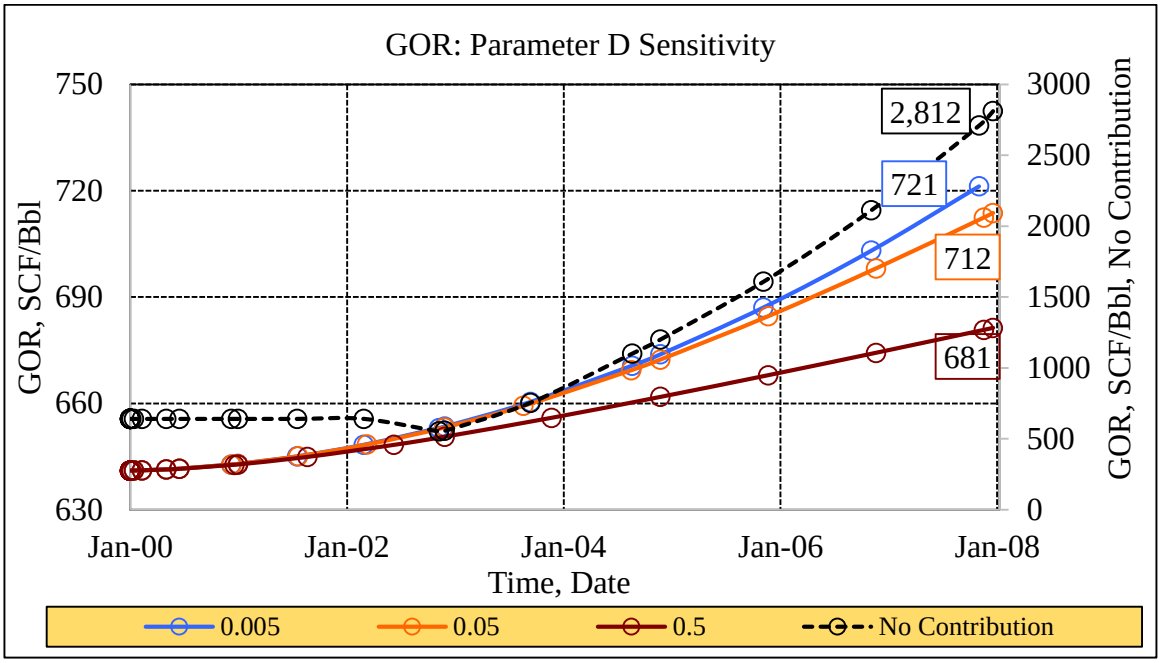

(b)

Figure 5.7: (a) Rate and cumulative oil performance type-curves for methane diffusivity variation. The data-labels show cumulative oil in thousand barrel in the eighth year of production. (b) Gas-oil ratio performance plot for methane diffusivity variation. The data-labels show gas-oil ratio in SCF/Bbl in the eighth year of production.

5.3.1.3 U&L Shale Fracture Permeability

Figure 5.8 (a) show the rate and cumulative-oil type-curves for variation in the U&L Shale fracture permeability. This parameter seemed to not affect the U&L Shale contribution. The rate was recorded higher by a small margin during the initial production-phase in the higher k_f cases. During the later phase of production it seemed that the contribution was more controlled by the amount of matrix-to-fracture fluid transfer in Shale than its k_f values. Figure 5.8 (b) show the GOR type-curves for parameter k_f and it suggests that the GOR increases with an increase in k_r. This following interpretation could explain this behavior. There was a slight increase in the cumulative production, and as all other parameters were unchanged, this increment was attributed to a prolonged drainage of the shale-matrix. The capacity of shale matrix to provide the production-contribution was unchanged and a prolonged drainage from the matrix only resulted in a larger pressure drop in the matrix. This pressure drop, in turn resulted in a larger amount of molecules to desorp from the shale matrix. Methane makes the largest fraction of these desorped-molecules' mixture and it might be prominent enough to increases the amount of gas in the production fluid.

5.3.1.4 The U&L Shale Fracture Spacing

The fracture spacing controls the shape-factor (Equation 4.2) of a dual-porosity media, which in turn affects the crucial matrix-to-fracture fluid-transfer (Equation (4.1). Figure 5.9 (a) show the performance plots for the U&L Shale fracture spacing (L_x) variation. There was a clear indication of more contribution from the U&L Shale as the fracture spacing decreased. The better-sustained rate could be attributed to the enhanced matrix-to-fracture fluid transfer, which was expected when fractures were closely spaced. The effect in the GOR type-curves, as the L_x decreased enhanced contribution for the U&L Shale increasingly subdued the GOR in the latter production phase. Figure 5.9 (b) shows the GOR type-curve for parameter L_x. It suggests there was an increase in GOR of the well as the fractures were spaced farther from each other. The behavior was interpreted by relating it to the enhancement in matrix-to-fracture fluid transfer. This enhancement takes place without causing any further drop in the shale-matrix pressure. Therefore, at a higher matrix pressure lesser amount of gas desorped out of the matrix, which might lower the amount of methane (gas) and fluid GOR.

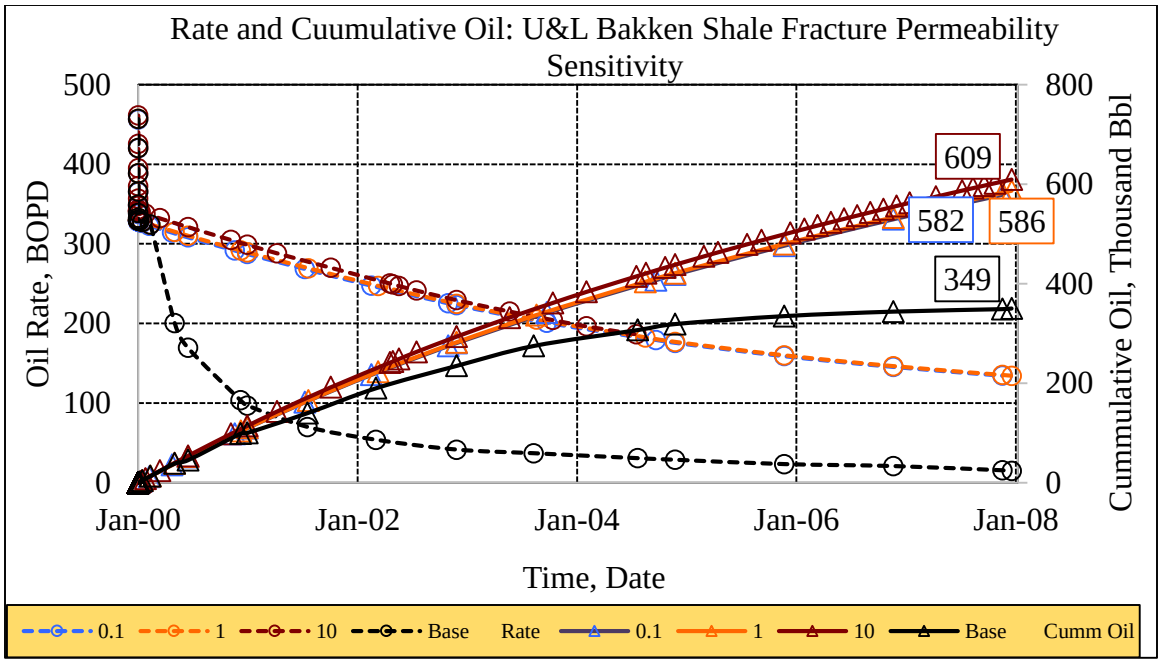

(a)

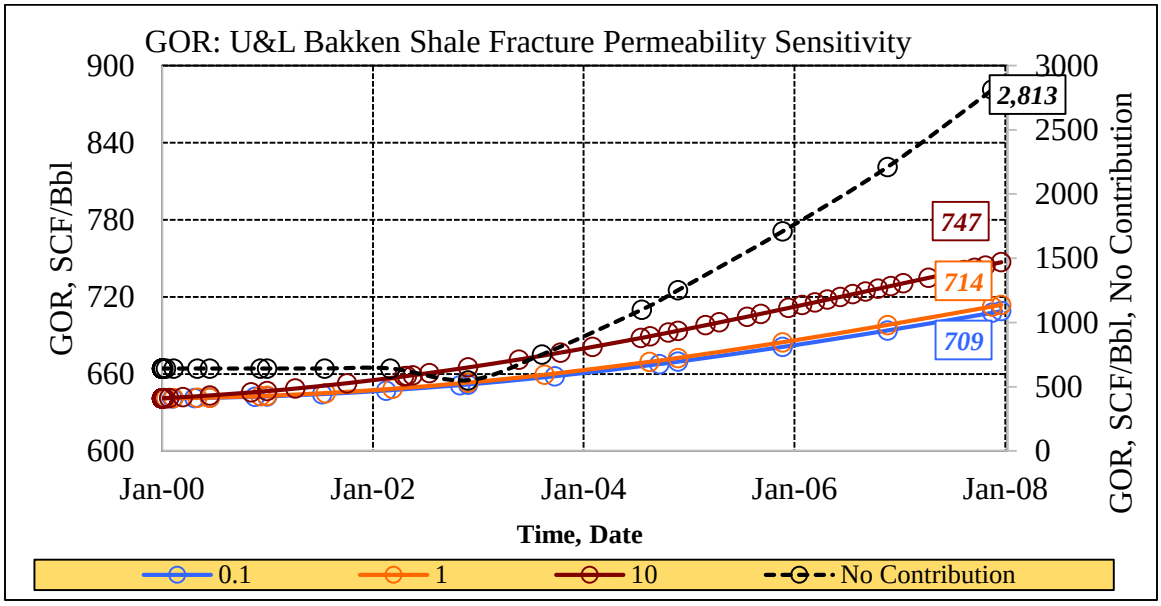

(b)

Figure 5.8: (a) Rate and cumulative oil performance type-curves for the Upper and Lower Shale fracture permeability variation. The data-labels show cumulative oil in thousand barrel in the eighth year of production. (b) Gas-oil ratio performance plot for U&L Shale fracture permeability variation. The data-labels show gas-oil ratio in SCF/Bbl in the eighth year of production.

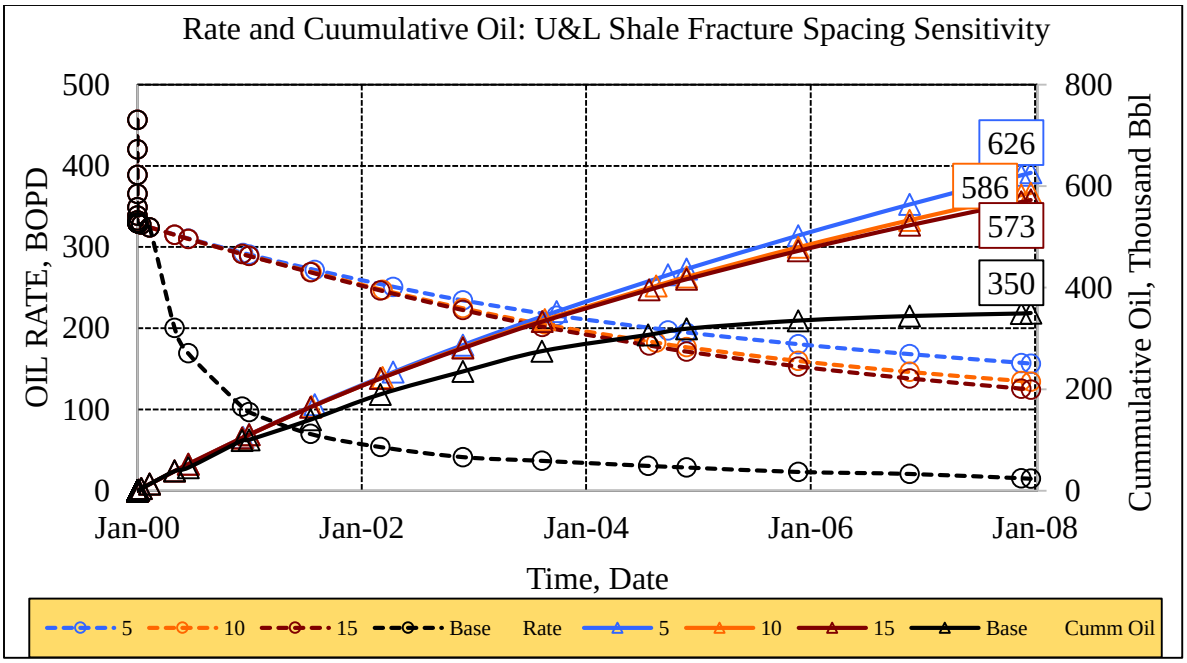

(a)

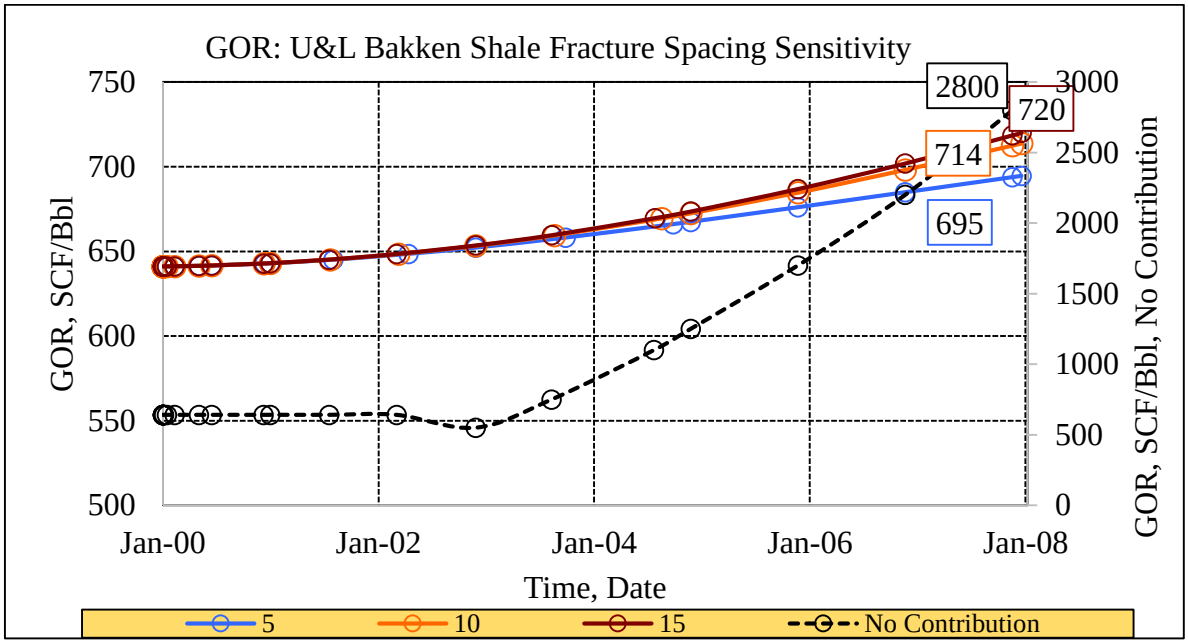

(b)

Figure 5.9: (a) Rate and cumulative oil performance type-curves for Upper and Lower Shale fracture spacing variation. The data-labels show cumulative oil in thousand barrel in the eighth year of production. (b) Gas-oil ratio performance plot for U&L Shale fracture spacing variation. The data-labels show gas-oil ratio in SCF/Bbl in the eighth year of production.

5.3.2 The Middle Bakken Parameters Sensitivity

The contribution-cases simulation-results for the minimum and the maximum values of the Middle Bakken parameters were derived from the Iteration# 10 to 13. The simulation result for the parameter's mean value was derived from Iteration #1NC. For the Middle-Bakken-parameter, their respective non-contribution case (Iteration #10NC to #13NC and #1NC) had different simulation results.

Plotting all the non-contribution case on the type-curves meant plotting twelve curves together on the same graph. For the purpose of maintaining clarity in the type-curves, the only non-contribution case simulation result of Iteration #1NC was included. The other non-contribution case results were utilized in the Tornado chart analysis in Section 5.5.

5.3.2.1 The Middle Bakken Matrix Porosity

The Middle Bakken matrix porosity (ϕ_m) was not expected to have a direct correlation with the U&L Shale contribution. It affected the deliverability of the Middle Bakken layer and thereby controlled the production-induced pressure-drop in the Middle layer. This pressure-drop in turn affected the fluid-flow and production-contribution from the U&L Shale fracture-network to the Middle layer.

The type-curves for parameter ϕ_m in Figure 5.10 (a) and (b) were expected to be cumulating the effect of the values of ϕ_m on both the production-contribution from the U&L Shale and that from the Middle layer. Therefore, it was not discernable from these type-curves, whether ϕ_m had a positive effect or negative effect on the production contribution from the U&L Shale.

U&L Shale production contribution for varying ϕ_m could be evaluated by comparing the contributions cases (Iteration #10 to #13 and #1) with the corresponding non-contribution case (Iteration #10 to #13 and #1). Section 5.5 demonstrates that the contribution from the U&L Shale is inversely proportional to ϕ_m. The disproportionality between the two could be related to the enhancement in the matrix support from the middle layer, which will reduce the requirement of contribution from the U&L Shale.

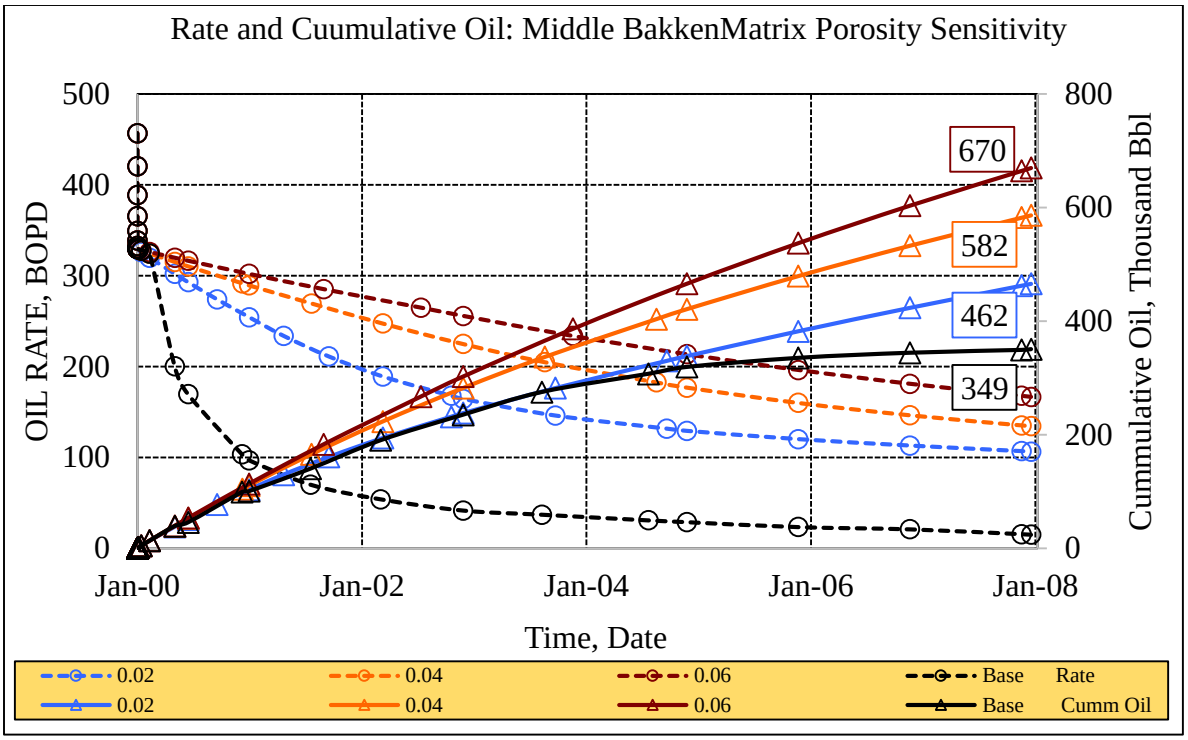

(a)

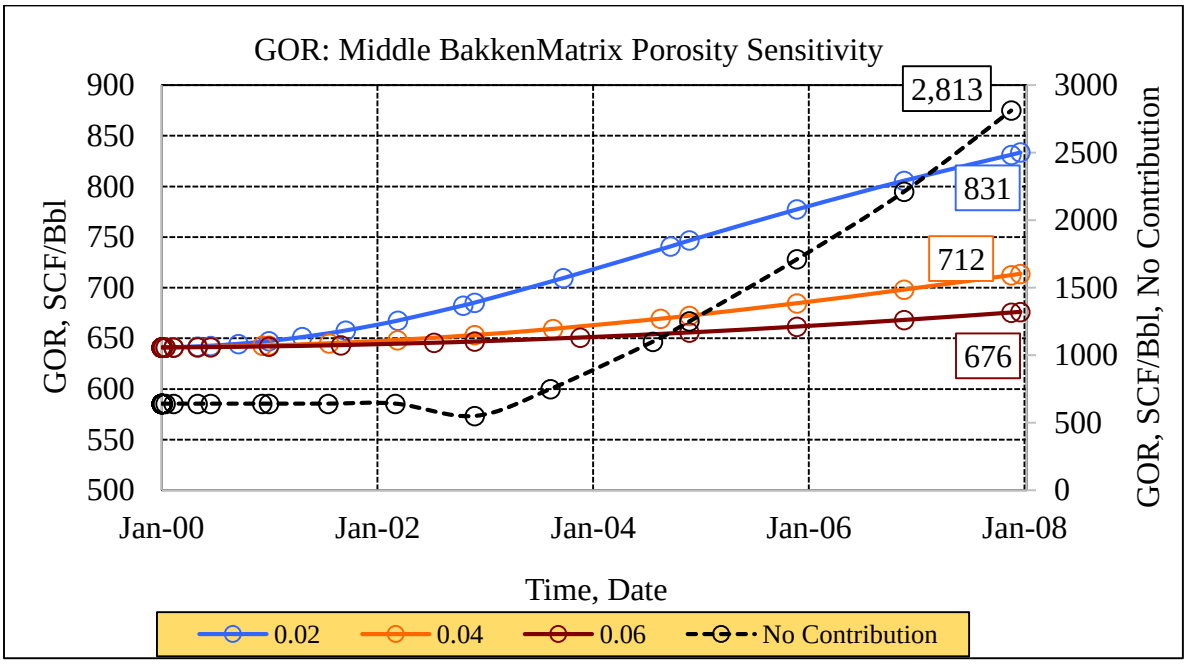

(b)

Figure 5.10: (a) Rate and cumulative oil performance type-curves for the Middle Bakken porosity variation. The data-labels show cumulative oil in thousand barrel in the eighth year of production. (b) Gas-oil ratio performance plot for the Middle Bakken porosity variation. The data-labels show gas-oil ratio in SCF/Bbl in the eighth year of production.

5.3.2.2 Middle Bakken Matrix Permeability

Figure 5.11 (a) and (b) show the type-curves for the Middle Bakken matrix permeability (k_m) variation. The similar effect, as seen in Section 5.3.2.1, could be expected because there should be an enhancement in the Middle Bakken matrix support with an increase in k_m. These type-curves were expected to include the effect of both improved matrix support from the Middle Bakken and the effect of increase or decrease in the contribution from the U&L Shale. Therefore, these type-curves might not reflect a clear sensitivity of U&L Shale production-contribution to k_m.

However, it is shown in Section 5.5 that the increase in k_m had a negative impact on the U&L Shale production contribution. The result was justified because an increase in k_m ensured more contribution from the Bakken matrix, so less support from the U&L Shale were subsequently required.

5.3.3 Hydraulic Fracture Parameters Sensitivity

Simulation results for the maximum and minimum values of the hydraulic-fracture parameters were derived from Iteration# 13 to 16. The simulation results for the mean values of each parameter were generated utilizing Iteration# 17. Iteration# 31 to 34 and 17 were used to generate the simulation results for the non-contribution case. Among them, the simulation results of Iteration#18 were the only non-contribution case, which was plotted over the type-curves. The simulation results of the other non-contribution case were utilized in the Tornado chart analysis in Section 5.5.

5.3.3.1 Fracture Half Length

The fracture half-length (FHL) augments the availability of the stimulated reservoir volume (SRV) in the Middle Bakken layer. Prolonged contribution could be expected from the Middle Bakken Matrix in a larger FHL case. Greater SRV also ensured a greater active contact area for fluid-transfer to the Middle Bakken from the U&L Shale layers. Therefore, with an increase in the active contact-area more fluid-transfer and production-contribution were expected from the Shale layers.

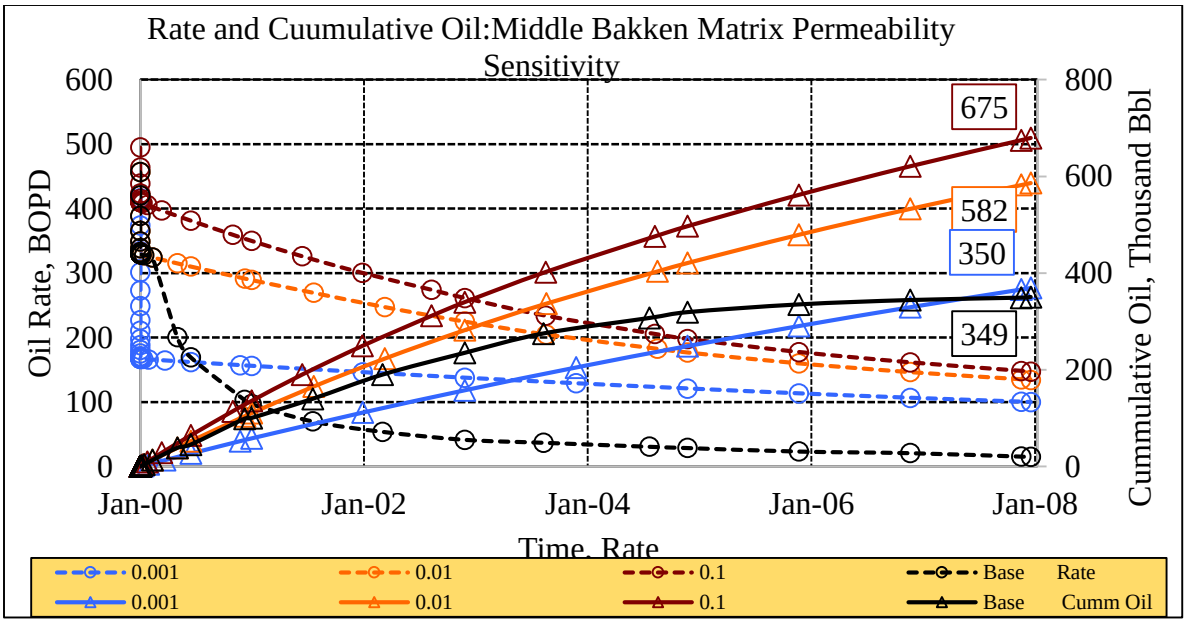

(a)

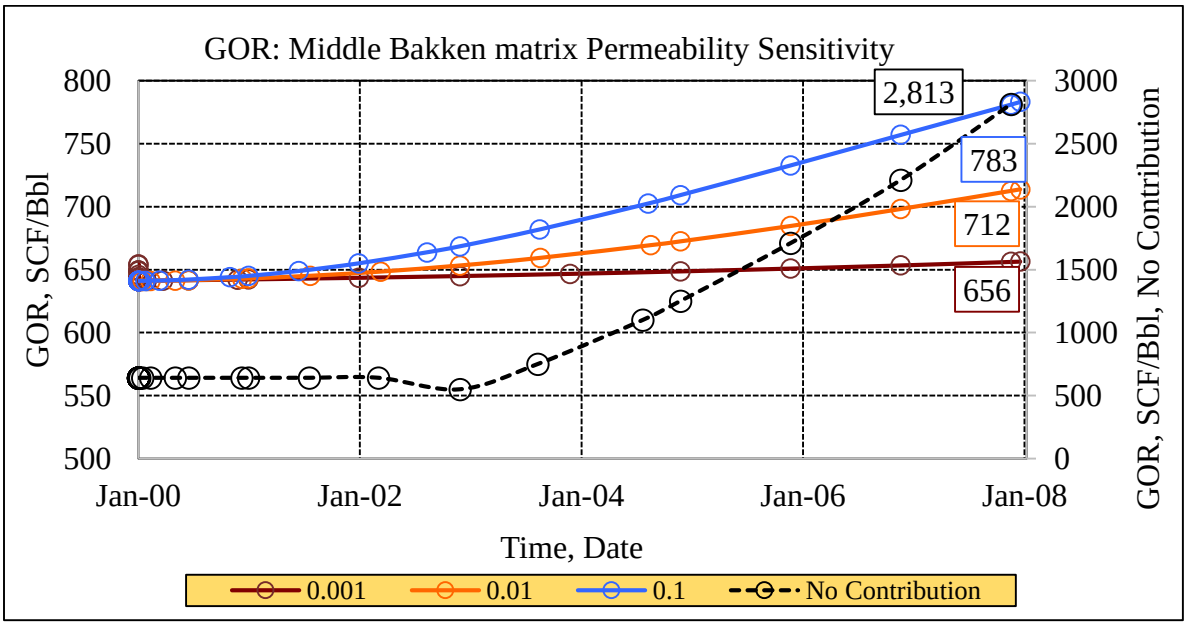

(b)

Figure 5.11: (a) Rate and cumulative oil performance type-curves for Middle Bakken matrix permeability variation. The data-labels show cumulative oil in thousand barrel in the eighth year of production. (b) Gas-oil ratio performance plot for curves for Middle Bakken matrix permeability variation. The data-labels show gas-oil ratio in SCF/Bbl in the eighth year of production.

The type-curves in Figure 5.12 (a) and (b) show that during the in the initial phase, oil rates were similar in all the FHL cases. In the later production-phase, the larger FHL case sustained with a higher oil rate, suggesting there was a prolonged Middle Bakken matrix-support. However, these type-curves presented a cumulative effect of the U&L Shale production contribution and support from the Middle Bakken matrix. Therefore, they should not be interpreted for the purpose of judging the effect of parameter FHL on the extent of production-contribution from the U&L Shale.

It will be later shown in Section 5.5 that the increase in FHL had increased the U&L Shale production contribution. However, the rate of the rise in this contribution with increasingly larger FHL seemed negative. The following could be interpreted as the reason for this observation. With an increase in parameter FHL the drainage radius of the well also increased, and at points farther from the well the pressure-drop in the reservoir is expected to decrease with the distance. Therefore, for a larger FHL case, higher pressure can be expected at farther point, which will lower the pressure differential across the Middle layer and the U&L Shale layers. The lower pressure differential means lower fluid transfer from and a net reduction in the production-contribution.

5.3.3.2 Hydraulic Fracture Spacing

Figure 5.13 (a) and (b) show the type-curves for variation in the hydraulic fracture spacing (FS). An increase in the number of hydraulic-fracture stages was expected to enhance the contact between the Middle Bakken matrices and fracture-network. This better contact ensured effective drainage from the Middle Bakken matrix. Moreover, an increase in the fracture-stages also increased the number of productive fracture-channels to the well. Therefore, a higher oil rates were observed for closely spaced fractures. However, the HFS did not affect the SRV and the same drainage area was expected to be available for each of these cases. Therefore, in the latter production-phase the oil-rates seemed to be converging to the same value.

In Section 5.5, it is shown that the closely spaced hydraulic fracture network assists in drawing more production contribution from the U&L Shale. The reason being a better contact between the Middle and the Shale layers with an increased number of hydraulic fractures along the well length.

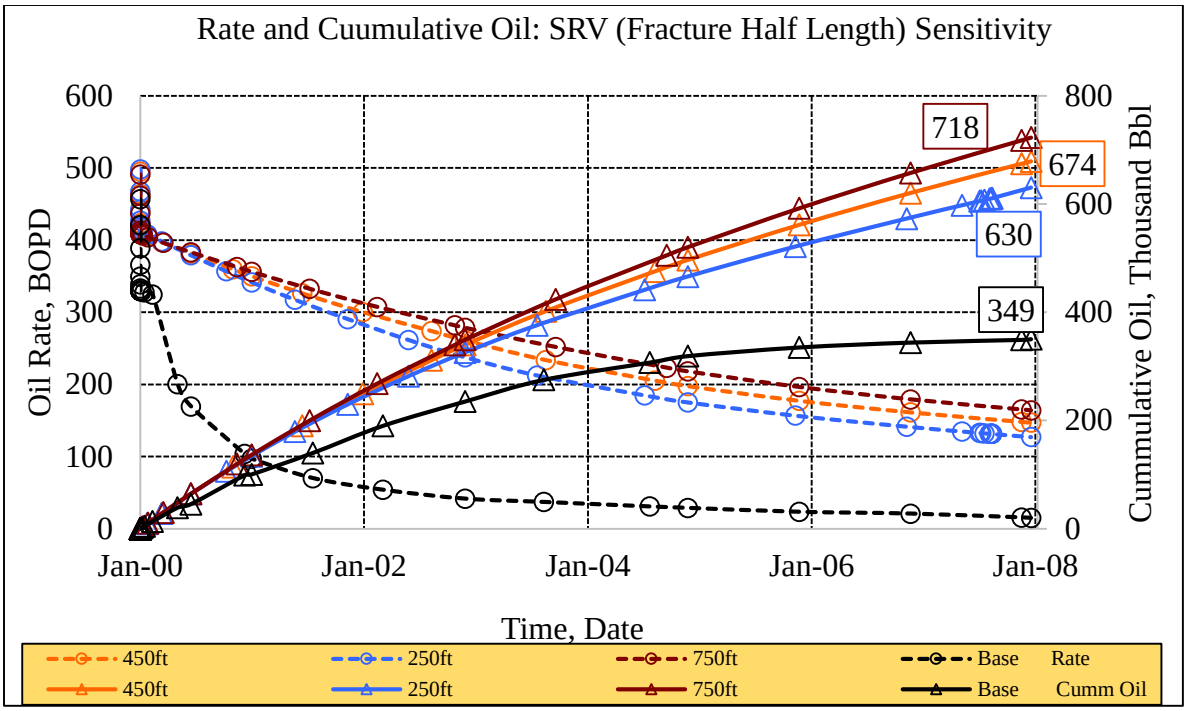

(a)

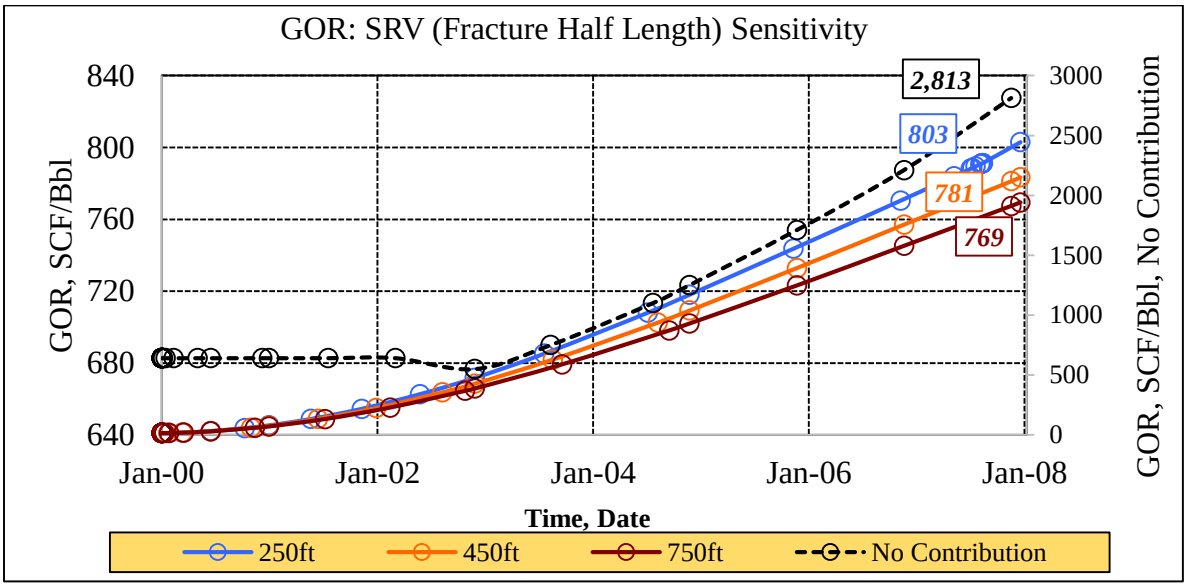

(b)

Figure 5.12: (a) Rate and cumulative oil performance type-curves for fracture half-length variation. The data-labels show cumulative oil in thousand barrel in the eighth year of production. (b) Gas-oil ratio performance plot for fracture half-length variation. The data-labels show gas-oil ratio in SCF/Bbl in the eighth year of production.

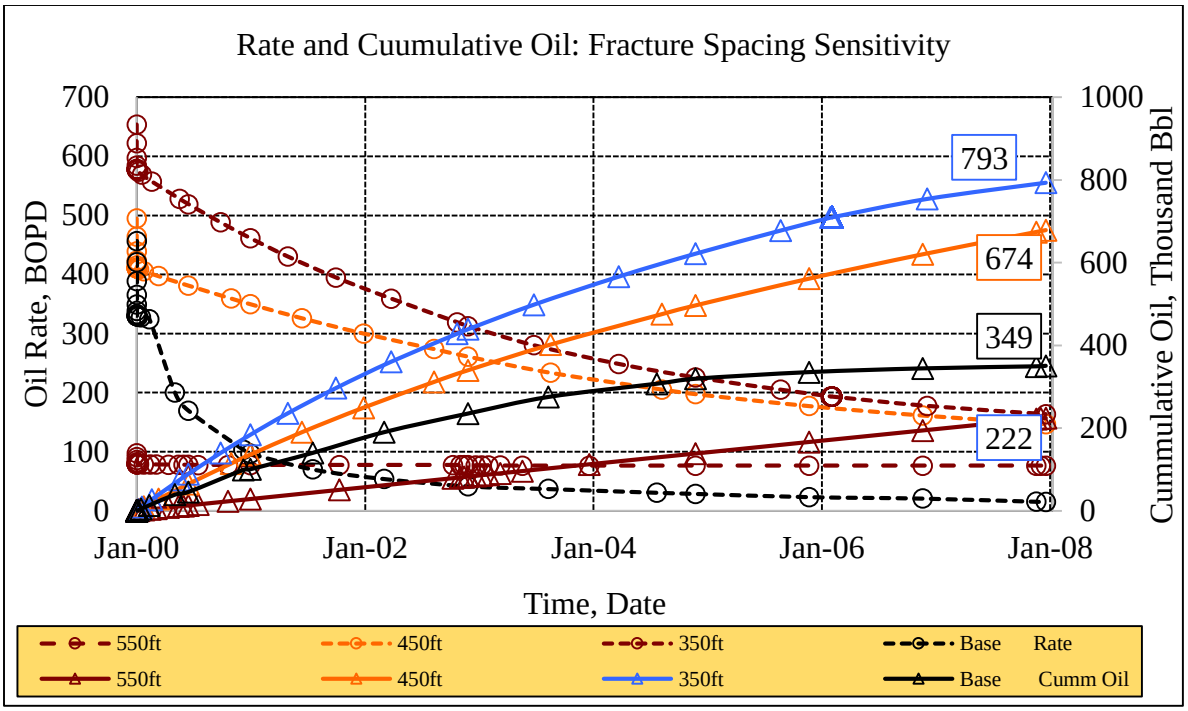

(a)

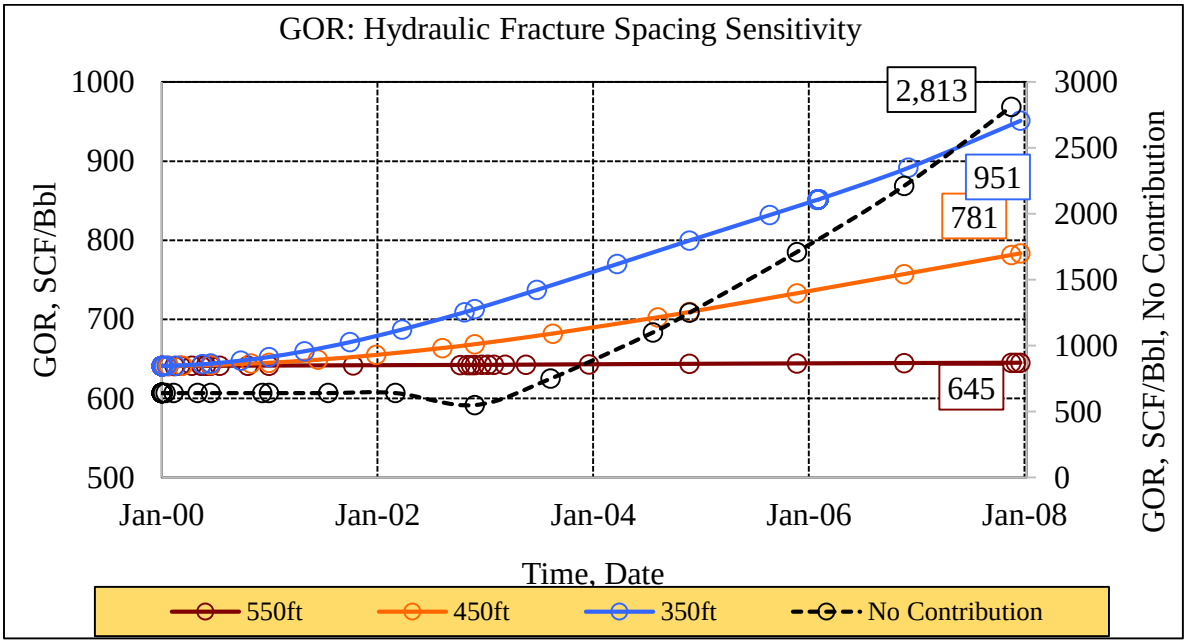

Figure 5.13: (a) Rate and cumulative oil performance type-curves for hydraulic fracture spacing variation. The data-labels show cumulative oil in thousand barrel in the eighth year of production. (b) Gas-oil ratio performance plots for hydraulic fracture spacing variation. The data-labels show gas-oil ratio in SCF/Bbl in the eighth year of production.

5.4 GOR Trends: Simulation results versus the field results

Figure 5.14 compares the simulation GOR responses at three different U&L Shale TOC values with the actual GOR response for the well producing from the Middle Bakken reservoir. The three different GOR from simulation iterations are in close resemblance with the three different representative cases (1, 2 or 3) for the GOR experience for the Middle Bakken wells. For the minimum TOC (3% w/w) case, desorption from the U&L Shale is substantial only at low-pressure ranges. Therefore, the contribution from the U&L Shale starts only after a substantial increase in GOR as pressure drops below the bubble-point pressure of the Middle Bakken oil. However, an active support from the U&L, after this point, arrests the pressure drop and therefore, the GOR is maintained at almost a constant level. At higher U&L Shale TOC values, the Shale production contribution could be expected to be substantial enough to completely arrest the pressure drop and therefore, no significant rise in the GOR in witnessed in such instances. Therefore, the type 2 and 3 responses for the Bakken wells might well relate to the local high in the TOC in the overlying and underlying Shale layers.

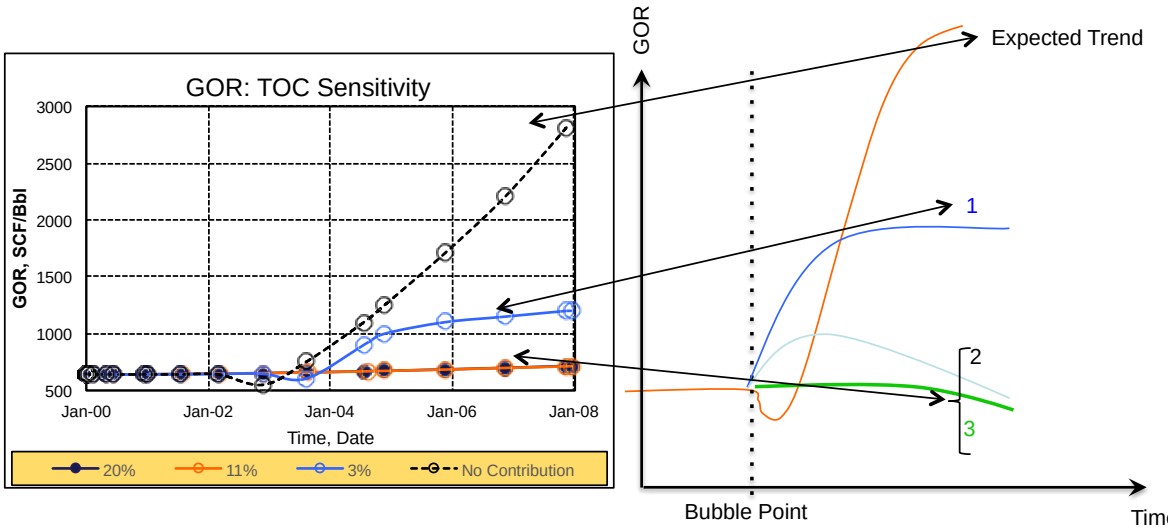

Figure 5.14: Comparison of the simulation result for the well with that of the gas-oil ratio response for the Bakken well.

5.5 Relative-sensitivity Study

A tornado chart was prepared to compare the sensitivities of the various parameters to the cumulative production for a given period of time. The aim of this analysis was to identify those parameters for which a change in their numerical values affect the cumulative production the

most and the least. This study was also intended to understand the degree of proportionality or disproportionality between the cumulative production and the values of the different parameters. The iteration listed in Table 5.5 was utilized to derive simulation results for this relative sensitivity study.

5.5.1 Data Preparation

Table 5.6 outlines the steps and calculations involved in the preparation of input data for the Tornado chart shown in Figure 5.16. Columns 2, 3 and 4 list the minimum, mean and the maximum values for each of the eight sensitivity-analysis parameters listed in column 1. The different values for the sensitivity analysis parameters were adopted from the Table 5.4.

Contribution Case Cumulative Production: Simulation results for the cumulative oil in the first eight years production were derived for the contribution-case iterations (# 1 to 17, Table 5.4). Column 5 lists the eight cumulative production results for the eight iterations in which one of the sensitivity-analysis parameters is set to its minimum value. For example, the value entered in the row for parameter TOC in column 5 was derived by setting the TOC to the minimum value, and setting other seven parameters to their respective mean-values. Similarly, column 7 lists the cumulative production for those cases in which one of the eight parameters is set to the maximum value. Column 6 lists the cumulative production for the case when all the parameters are set to their respective mean values. The cumulative production values in all the rows of column 6 are essentially the same, because they derive results from the same iteration (#17) in which all the parameters are at their respective mean values.

Non-contribution Case Cumulative Production: The same convention is followed in column 8, 9 and 10 to list the simulation results for the cumulative production in non-contribution cases, which were derived utilizing Iteration# 1NC up to #17NC. Column 8 lists the cumulative oil for the non-contribution case iterations in which one of the eight parameters is set to its minimum value. Column 9 lists the cumulative oil for the non-contribution case iterations in all the eight parameters are set to their mean value and as discussed previously, their values in all the rows are the same. Column 10 lists the cumulative oil for the non-contribution case iterations in which one of the eight parameters is at its maximum value.

Contribution from U&L Shale: The cumulative production values listed in columns 4 and 7 were derived utilizing essentially the same combinations of the values of the eight parameters except, the contribution from the U&L Shale was annulled in column 7. The row-wise differences in the values in these columns are basically the U&L Shale production contribution, when one of the eight parameters is set to its minimum value. Column 11 lists these U&L Shale contributions as the percentage of contribution case cumulative production values listed in column 5. Column 12 lists the contribution in percentage when all the parameters are set to their respective mean values. Lastly, column 13 lists the contribution in percentage when one of the parameters is set to its maximum value.

Figure 5.15 plots the different simulation-results for the U&L Shale production-contribution, represented as the percentage of the respective cumulative production. As outlined in Section 5.2, while deriving the U&L Shale contribution results at the minimum, mean and the maximum values of a particular parameter, others are maintained as constants at their respective mean values.

5.5.2 Tornado-chart Analysis

Column 14 and 15 lists the difference between the columns 11 and 12, and columns 13 and 12 respectively. The values in column 14 could be interpreted as the rise or fall in the U&L Shale production contributions as the value of one of the eight parameters is changed from its minimum to its mean. Similarly, column 15 lists the same rise or fall, but this time the value of the parameters is changed from its maximum to its mean.

Tornado chart in Figure 5.16 plots the column 14 and 15 with the series-names ‘MIN’ the ‘MAX’ respectively. It is evident from the chart that the U&L Shale TOC, which controls matrix storage capacity; and D, which control the matrix-to-fracture fluid transfer, have the maximum impact on the anticipated contribution. The chosen range for other U&L shale parameters seems not to alter the contribution-percentage significantly.

As the TOC (Wt. %) in the U&L Shale dropped from the mean values of 11% to the minimum of 3%, the contribution-percentage dropped by 16.4%. However, a rise in TOC from 11% to 20% enhanced the contribution by a meager 2.2%. This result indicates that with the

adopted values of the parameters, the effect of rise in TOC beyond 20% should not alter the results for the contribution.

The result for component diffusivity is similar in the left wing of the chart as the value dropped from the mean to the minimum value. However, the result of 6.2 % rise in the contribution-percentage in right wing of the chart suggest that there is still a room for an increase in parameter D, which is expected to enhance the U&L Shale contribution-percentage.

Enhancements in the Middle Bakken matrix with an increase in parameters ϕ_m and k_m had a negative impact on the Shale contribution, as it was reflected from the corresponding bars in the Tornado chart. However, the effects of change in these parameters on the contribution-percentages are not as pronounced as the U&L Shale parameters.

Lastly, hydraulic fracture enhancements have a positive impact on the contribution-percentage, which is reflect in the chart for FHL and HFS bars in the chart. The close-spaced fractures seem to further improve the U&L contribution-percentages.

5.6 The Best and The Worst Contribution-scenario

The Tornado chart analysis suggests that the Iterations #1 and #3 in Table 5.7 represent the best and the worst scenarios for the U&L Shale production-contribution. In Iteration #2 all the parameters were set to their mean values. The last three iterations in the table are the corresponding non-contribution case iterations. Columns 5 to 10 in Table 5.8 list the simulation-results for the cumulative production for the six iterations. Columns 11, 12 and 13 contain the results for the worst (11%), the most expected (40%) and the best (52%) possible values for the U&L Shale production contribution with the surveyed data-ranges in Table 5.4.

Table 5.6: Calculation Table for the tornado-chart.

	Sensitivity Analysis Parameters			Cummulative Oil For eight Years of Production			Base Case (Without Contribution)			Contribution From the U&L Shale			Tornado-Chart %	
1	2	3	4	5	6	7	8	9	10	11	12	13	14	15
										(=(5-8/5)	*(=(6-9)/6)*	*(=(7-10)/9)*	*(=11-12)*	*(=13-12)*
Parameter	**Min**	**Mid**	**Max**	**Min**	**Mid**	**Max**	**Min**	**Mid**	**Max**	**Min**	**Mid**	**Max**	**Min**	**Max**
D	0.005	0.05	0.5	456090	586381	654115	350331	350331	350331	23%	40%	46%	-17.1%	6.2%
TOC	3	11	20	460017	586381	608809	350331	350331	350331	24%	40%	42%	-16.4%	2.2%
HFS	350	450	550	793487	586381	224343	451304	350331	143760	43%	40%	36%	2.9%	-4.3%
ϕ_m	0.02	0.04	0.06	465672	586381	669714	259456	350331	413217	44%	40%	38%	4.0%	-2.0%
k_m	0.001	0.01	0.1	369191	586381	679239	214012	350331	429438	42%	40%	37%	1.8%	-3.5%
L_x	5	10	15	626237	586381	572881	350331	350331	350331	44%	40%	39%	3.8%	-1.4%
FHL	250	450	750	630192	586381	722816	391304	350331	429760	38%	40%	41%	-2.3%	0.3%
k_f	0.1	1	10	582722	586381	609373	350331	350331	350331	40%	40%	43%	-0.4%	2.3%

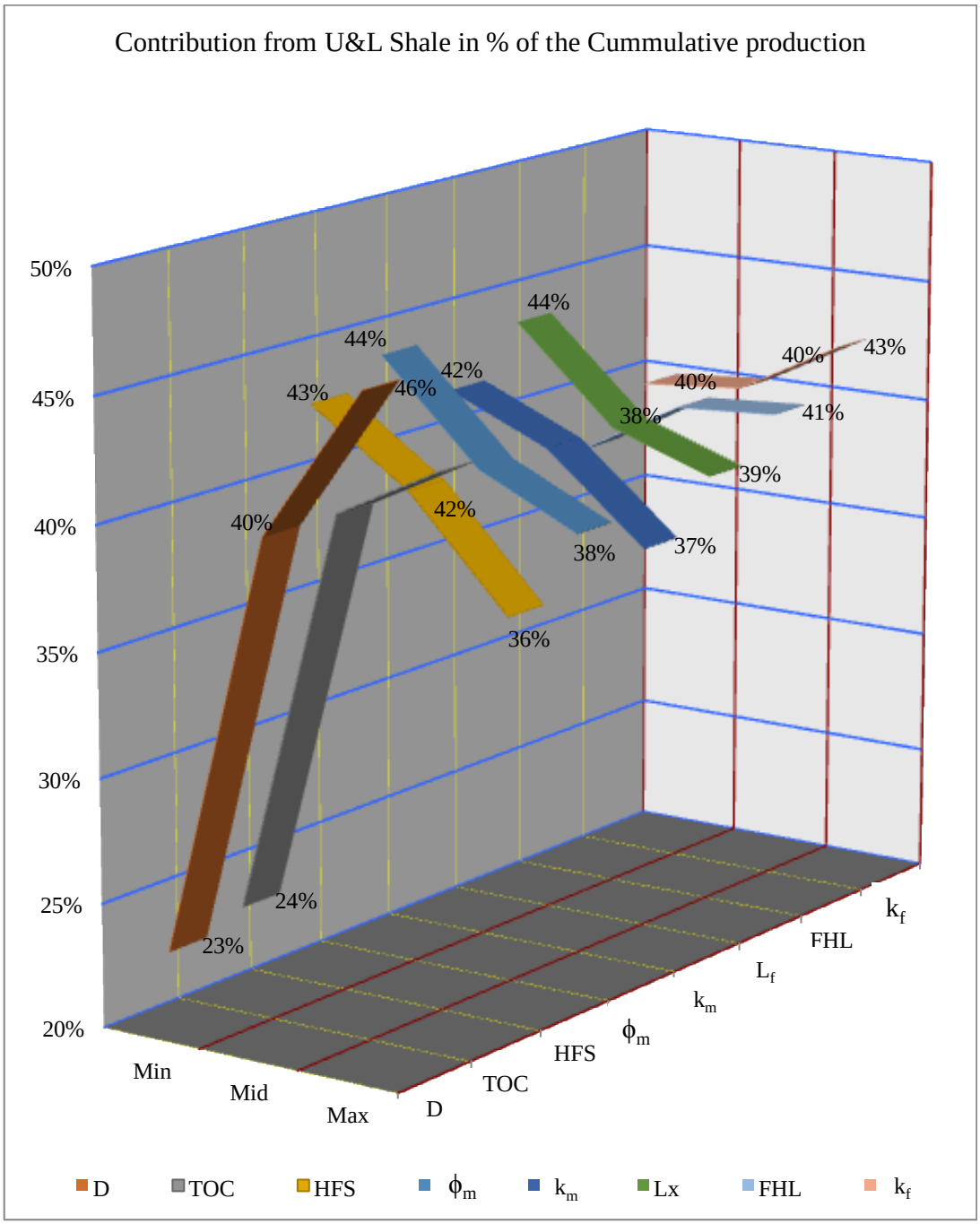

Figure 5.15: The U&L Shale production-contribution at the minimum, mean and the maximum values of the eight parameters. The contributions in different cases are represented as percentages of the corresponding eight years cumulative-productions. Plotted data derived from columns 11, 12 and 13 of Table 5.6.

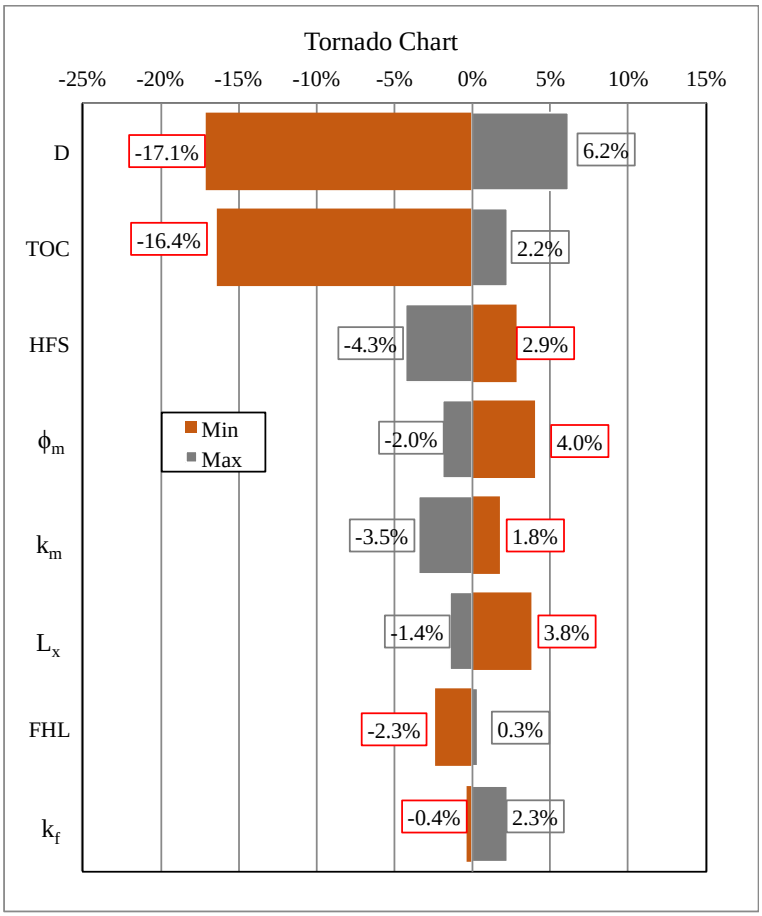

Figure 5.16: Tornado-chart showing the relative sensitivity of different parameters on the production contribution to the Middle Bakken reservoir from the Upper and Lower Shale.

Table 5.7: The combination of sensitivity analysis parameters used in the best and the worst U&L Shale contribution scenario.

Iteration type	Parameters	Iteration #	(TOC, D, Kf, Lx, Φm, Km, FHL, HFS)	TOC	D	Kf	Lx	Φm	Km	FHL	HFS
Contribution Case	Worst Case	1	*(MN, MN, MN, MX, MX, MX, MN, MX)*	3	0.005	0.1	15	6%	0.100	250	550
	Mean	2	*(MD, MD, MD, MD, MD, MD, MD, MD)*	11	0.050	1.0	10	4%	0.010	450	450
	Best Case	3	*(MX, MX, MX, MN, MN, MN, MX, MN)*	20	0.500	10.0	5	2%	0.001	750	350
Non-Contribution Case	Worst Case	1NC	*(MN, MN, ZERO, MX, MX, MX, MN, MX)*	3	0.005	0	15	6%	0.100	250	550
	Mean	2NC	*(MD, MD, ZERO, MD, MD, MD, MD, MD)*	11	0.05	0	10	4%	0.010	450	450
	Best Case	3NC	*(MX, MX, ZERO, MN, MN, MN, MX, MN)*	3	0.005	0	5	2%	0.001	750	350
MD=Mean, MN=Minimum, MX=Maximum											

Table 5.8: Calculation table for the best and the worst scenario for the U&L Bakken Shale contribution.

	Sensitivity Analysis Parameters			Cumulative Oil For eight Years of Production (Contribution Cases)			Cumulative Oil For eight Years of Production (Non-contribution Cases)			Contribution From the U&L Shale		
1	2	3	4	5	6	7	8	9	10	11	12	13
										(=(5-8/5)	*(=(6-9)/6)*	*(=(7-10)/9)*
Parameter	Worst Case	Mean	Best Case	Worst Case	Mean	Best Case	Worst Case	Mean	Best Case	Worst Case	Mean	Best Case
TOC	3	11	20	563451	586381.25	868854	498451	350331	413456	12%	40%	52%
D	0.005	0.05	0.5									
Kf	0.1	1	10									
Lx	15	10	5									
Φm	0.06	0.04	0.02									
Km	0.1	0.01	0.001									
FHL	250	450	750									
HFS	550	450	350									

CHAPTER 6

CONCLUSION AND SUGGESTIONS

This chapter concludes this research by outlining the various results and their interpretation. The limitations in the scope of these results are also discussed. Different improvements are recommended for future studies to overcome these shortcomings.

6.1 Conclusions

1. The production performance anomalies of the Middle Bakken wells could be attributed to the interference from the U&L Shale layers. This interference might act like an active production-support to aid the recovery mechanism of the Middle Bakken reservoir.
2. The phenomena of desorption and diffusion of hydrocarbon molecules in the organic rich U&L Shale matrix is expected to play a significant role in this production-contribution. By including their mathematical formulations in the reservoir simulation, the proposed contribution can be quantified with some reservations.
3. Results from the simulation utilizing the surveyed primary input data suggest that the U&L Shale layers might be contributing in a range of 10%-50% of the total cumulative production of the Middle Bakken wells. With the mean values of each of the primary input parameters, the contribution was estimated as 40% of the cumulative production. It could be noted here that Sonnenberg and Pramudito (2009) reported the contribution from the Upper Shale in Elm Coulee Field (Lower Shale absent) might be up to 20%. Therefore, the derived 40% collective contribution from the two Shale layers (Upper and Lower) may be justified. However, because of the uncertainties in the values of certain sensitivity analysis parameters, the possibility of the over-estimation of the contribution cannot be completely ruled out.
4. Parametric sensitivity analysis in Chapter 5 suggests that the contribution from the Shale layers is the most sensitive towards the total organic carbon (TOC) and the diffusivity coefficients (D). The enhancements in the Middle layer's reservoir quality have a

negative impact on the proposed contribution. However, the improvements in hydraulic fracturing encourage the contribution.

6.2 Limitations

1. There exists a major knowledge-gap in the present understanding of the fluid-storage and fluid transportation in liquid rich shales. Therefore, quantifying the anticipated contribution form the U&L Shale might pose serious theoretical challenges. The mathematical equations used to model desorption and diffusion in the simulation calculation were an approximation and there are no validity-checks to their effectiveness. Moreover, the process of desorption assumes an equilibrium or steady state while performing the calculations, which might not be true and transitory in nature.
2. Heterogeneity and anisotropy in reservoir properties were ignored in this study. Not much heterogeneity was expected over the areal-extents, however, the existence of five different facies for the Middle Bakken is well known and heterogeneity along the vertical axis should be ideally accounted for. Similarly, ignoring the anisotropy could have hampered the quality of the results.
3. Lack of a laboratory calibration of the TOC-based correlation for the Langmuir isotherm parameters might limit the accuracy levels of the results. TOC correlation used in this study for the isotherm parameters is based on single-phase laboratory results for methane, which might not appropriately represent the multicomponent desorption in the Bakken Shale.
4. The crucial diffusion coefficient (D) and their exact range in Bakken Shale were not known. The results of this research suggest that the parameter D significantly affects the contribution process. Therefore, the lack of the representative range of parameter D might considerably affect the results for the anticipated contribution.
5. The geomechanical effects on the porosity and permeability are known to influence the production-performance of tight or unconventional reservoirs. Ignoring them in the simulation scheme might have affected the accuracy of the quantitative results, which were derived in Chapter 5

6.3 Recommendations for Future Work

1. A range of future research opportunities exists in both the laboratory studies and the mathematical modeling of the fluid storage and flow mechanism in oil rich shale. Without a better understanding of these processes, reliable quantitative results cannot be achieved for the anticipated production contribution.
2. Future research might facilitate an effective and more reliable method to include desorption in the liquid rich shales. The scheme for desorption of molecules in the liquid phase might described in section 2.5 might not be theoretically consistent with the laws of physics. Moreover, an analogy of the Langmuir isotherm was adopted from the phenomenon of desorption in the gas bulk, which might not fully represent desorption taking place in the liquid bulk.
3. The TOC-based derivation for the Langmuir isotherm parameters requires a comprehensive study, especially a multicomponent desorption situation. The correlations adopted from the contributions from Zhang, et al. (2012) and Lewis, et al. (2004) might be a case-specific solution.
4. The capillary pressure and the relative permeability experiments for the liquid rich shales are required for the crucial rock-fluid input data in the simulation studies. The complication associated with the very low permeability systems for such experiments needs to be addressed with developments in the existing experimental procedures.
5. The geomechanical effects on the primary input parameters, such as porosity and permeability need to be studied in detail. They might also affect the phenomena of diffusion and desorption in the organic-matter pores of the U&L Shale. Relevant laboratory studies are required to account for such effects.
6. Other source of validation for the presence of desorped gas in the production gas stream could also be investigated. One such source could be the separator gas compositional analysis, which can be analyzed for the compositional anomalies to validate the desorption-based contribution form the U&L Shale.
7. Sensitivity for other parameters such as the U&L Shale thickness; type of relative permeability and capillary pressure curves; reservoir fluid composition etc. could also be performed.

REFERENCES

Ambrose, R. J., Hartman, Robert C., Mery, D. C., Akkutlu, Y. I., Sondergeld, C. H. 2010. New Pore-scale Considerations for Shale Gas in Place Calculations. SPE 131772 Presented at Unconventional Gas Conference, Pittsburgh, Pennsylvania.

Arri, L. E., Yee, D., Morgan, W. D., Jeansonne, M. W. 1992. Modeling Coalbed Methane Production with Binary Gas Sorption. SPE 24363 Presented at Rocky Mountain Regional Meeting. Casper, Wyoming

Chen, J., Chen, S. 2008. A New Mixing Rule of Self Diffusivities in Methane Hydrocarbon Mixtures and the Determination of GOR and Oil Viscosities from NMR Log. SPE 115510 Presented at Annual Technical Conference and Exhibition, Denver, Colorado.

Chen, J.H., Li, B., Georgi, D., Chen, J., Yan, W. 2012. Petrographic Features of Kerogen in Gas Shales and their Effect on Hydrocarbon Storage. SPE 162612 Presented at Abu Dhabi International Petroleum Conference and Exhibition, Abu Dhabi, UAE.

Computer Modeling Group (CMG^{TM}). GEM User Manual and Documentation. CMG, Version 2012.

Dechongkit, P., Prasad, M. 2011. Recovery Factor and Reserves Estimation in the Bakken Petroleum System (Analysis of the Antelope, Sanish and Parshall fields). CSUG/SPE 149471 Presented at Presented at Canadian Unconventional Resources Conference, Calgary, Alberta.

EERC. GIS for Bakken and Three Forks formation. Website: http://www.undeerc.org/bakken/dss/. Accessed on 30th April 2013.

Ertekin, T., King, G. R., Schwerer, F. C. 1986. Dynamic Gas Slippage: A Unique Dual-Mechanism Approach to the Flow of Gas in Tight Formations. SPE 12045 Published in Formation Evaluation Journal. Vol. 1, No. 1 (February 1986): 43-52.

Fathi, E., Akkutlu, Y. I. 2009. Nonlinear Sorption Kinetics and Surface Diffusion Effects on Gas Transport in Low-permeability Formations. SPE 124478 Presented in Annual Technical Conference and Exhibition. New Orleans, Louisiana.

Freeman, C. M., Moridis, G. J., Michael, G. E., Blasingame, T. A. 2012. Measurement, Modeling, and Diagnostics of Flowing Gas Composition Changes in Shale Gas Wells. SPE 153391 Presented at Latin America and Caribbean Petroleum Engineering Conference, Mexico City.

Gao, C., Lee, J. W., Spivey, J. P., Semmelbeck, M. E. 1994. Modeling Multilayer Gas Reservoirs Including Sorption Effects. SPE 29173 Presented at Eastern Regional Meeting, Charleston, West Virginia.

Javadpour, F. 2007. Nanopores and Apparent Permeability of Gas Flow in Mudrocks (Shales and Siltstone). Journal of Canadian Petroleum Technology. Volume 48, No. 8, 16-21.

Kazemi, H., Merrill, L. S. Jr, Porterfield, K. L., Zemen, P. R. 1976. Numerical Simulation of Water Oil Flow in Naturally Fractured Reservoirs. SPE 5719 Published in Society of Petroleum Engineers Journal, Littleton, Colorado. December, 317-326.

Lewis, R., Ingraham, D., Pearcy, M., Williamson, J., Sawyer, W., Frantz, J. 2004. New Evaluation Techniques for Gas Shale. Schlumberger Reservoir Symposium, Houston, Texas.

Loucks, R. G., Reed, R. M., Ruppel, S. C., Jarvie, D. M. 2009. Morphology, Genesis, and Distribution of Nanometer-scale Pores in Siliceous Mudstones of the Mississippian Barnett Shale. Journal of Sedimentary Research. Volume 79, 848-861.

Meissner, F. F. 1978. Petroleum Geology of the Bakken Formation, Williston Basin, North Dakota and Montana. The Economic Geology of the Williston Basin, Montana Geological Society. The Economic Geology of the Williston Basin, Montana Geological Society. 1978, 207-230.

NDIC Oil and Gas Division. North Dakota Drilling and Production Statistics. January 2013. https://www.dmr.nd.gov/oilgas/stats/statisticsvw.asp (accessed 30th April 2013).

Nghiem, L. X., Li, Y. K., Agarwal, R. K. 1989. A Method for Modeling Incomplete Mixing in Compositional Simulation of Unstable Displacements. SPE 18439 Presented at Symposium on Reservoir Simulation, Houston, Texas

Nojabaei, B., Johns, R. T., Chu, L. 2012. Effect of Capillary Pressure on Fluid Density and Phase Behavior in Tight Rocks and Shales. SPE 159258 Presented at Annual Technical Conference and Exhibition, San Antonio, Texas.

O'Brien, D. G., Larson, R. T. Jr, Parham, R. C., Thingelstad, B. L., Aud, W. W., Burns, R. A., Weijers, L. 2012. Using Real-Time Downhole Microseismic To Evaluate Fracture Geometry for Horizontal Packer-Sleeve Completions in the Bakken Formation, Elm Coulee Field, Montana. SPE 139774 Published in Production and Operations Journal. February, Volume 27, No.1, 27-43.

Ozkan, E., Raghavan, R., Apaydin, O. G. 2010. Modeling of Fluid Transfer from Shale Matrix to Fracture Network. SPE 134830 Presented at Annual Technical Conference and Exhibition, Florence, Itly.

Peaceman, D. W. 1987. Interpretation of Well-Block Pressures in Numerical Reservoir Simulation - Part 3: Some Additional Well Geometries. SPE 16976 Presented in 62nd SPE Annual Technical Conference and Exhibition, Dallas, Texas.

Peaceman, D. W. 1983. Interpretation of Well-Block Pressures in Numerical Reservoir Simulation with Nonsquare Grid Blocks and Anisotropic Permeability. SPE 10528 Published in Society of Petroleum Engineers Journal. June, 531-569.

Peng, D. Y., Robinson, D. B. 1976. A New Two-Constant Equation of State. Published in Journal Industrial and Engineering Chemistry. Fundamentals, Issue 15, 59-64.

Pitman, J. K., Price, L., LeFever, J. A. 2003. Diagenesis and Fracture Development in the Bakken Formation, Williston Basin: Implications for Reservoir Quality in the Middle Member. USGS 1653 Published as U.S. Geological Survey Professional Paper.

Schmoker, J. W., Hester, T. C. 1983. Organic carbon in the Bakken Formation, United States Portion of Williston basin. Published in American Association of Petroleum Geologists Bulletin. Volume 67, 2165-2174.

Sonnenberg, S. A., Pramudito, A. 2009. Petroleum Geology of the Giant Elm Coulee field, Williston Basin. Published in American Association of Petroleum Geologists Bulletin. September, Volume 93, 1127-1153.

Swami, V., Settari, A. 2012. A Pore Scale Gas Flow Model for Shale Gas Reservoir. SPE 155756 Presented in American Unconventional Resources Conference, Pittsburg, Pennsylvania.

Tran, T., Sinurat, P., Wattenbarger, R. A. 2011. Production Characteristics of the Bakken Shale Oil. SPE 145684 Presented at Annual Technical Conference and Exhibition, Denver, Colorado.

USGS. 2008. U.S. Geological Survey. Petroleum Resource assessment of the Bakken Formation, Williston Basin Province, Montana and North Dakota. Slide Presentation for US Department of Interior, Washington, D.C. April.

USGS. 2012. National Oil and Gas Assessment 2012 Assessment Updates. Web Page for Total Mean Oil: http://energy.usgs.gov/OilGas/AssessmentsData/NationalOilGas-Assessment/Assessment Updates.aspx. Accessed on 31st April 2013.

Yan, B., Wang, Y., Killough, J. E. 2013. Beyond Dual-Porosity Modeling for the Simulation of Complex Flow Mechanisms in Shale Reservoirs. SPE 163651 Presented at Reservoir Simulation Symposium, The Woodlands, Texas.

Zhang, T., Ellis, G. S., Ruppel, S. C., Milliken, K., Yang, R. 2012. Effect of Organic-Matter Type and Thermal Maturity on Methane Adsorption in Shale Gas Systems. Published in Elsevier Organic Geochemistry Journal. Volume 47, 120-131.

APPENDIX A: MATERIAL BALANCE TIME AND CUMULATIVE GAS-OIL RATIO

The gas-oil ratio (GOR) performance plot in Section 3.2 uses the material balance time (MBT) to normalize the production time of the wells with their respective cumulative production. Cumulative gas-oil ratio (CGOR) was used to eliminate the short-lived fluctuations in the producing GOR (PGOR). Table A.1 presents the overview of the calculations performed to evaluate the MBT and CGOR at different production time for a Reunion Bay Field well. Figure A.1 compares the PGOR and CGOR with respect to the MBT; a stable and interpretable CGOR response in comparison to PGOR is evident.

Table A.1: Sample table calculation performed on an example well 16781 (Reunion Bay Field).

Date	Days	BBLS Oil	MCF Gas	Cum Oil	Cum Gas	MBT	PGOR	CGOR
						$\frac{\text{Cum Oil}}{\text{Latest Cumm Oil}}$	$\frac{1000 * \text{MSFD}}{\text{BOPD}}$	$\frac{1000 * \text{Cum gas}}{\text{Cum Oil}}$
Apr-08	19	18721	8012	18721	8012	0.05	428	428
May-08	31	21639	18398	40360	26410	0.10	850	654
Jun-08	30	16362	12295	56722	38705	0.14	751	682
Jul-08	31	13495	10331	70217	49036	0.18	766	698
Aug-08	31	11303	8494	81520	57530	0.21	751	706
Sep-08	5	843	755	82363	58285	0.21	896	708
Oct-08	13	6472	2717	88835	61002	0.22	420	687
Nov-08	30	14812	6730	103647	67732	0.26	454	653
Aug-10	31	6658	5805	286679	201497	0.72	872	703
….	….	….	….	….	….	….	….	….
….	….	….	….	….	….	….	….	….
….	….	….	….	….	….	….	….	….
….	….	….	….	….	….	….	….	….
….	….	….	….	….	….	….	….	….
Jun-12	30	3374	2770	387655	562636	0.98	821	1451
Jul-12	31	2937	4875	390592	567511	0.98	1660	1453
Aug-12	31	3071	9934	393663	577445	0.99	3235	1467
Sep-12	30	3133	9450	396796	586895	1	3016	1479

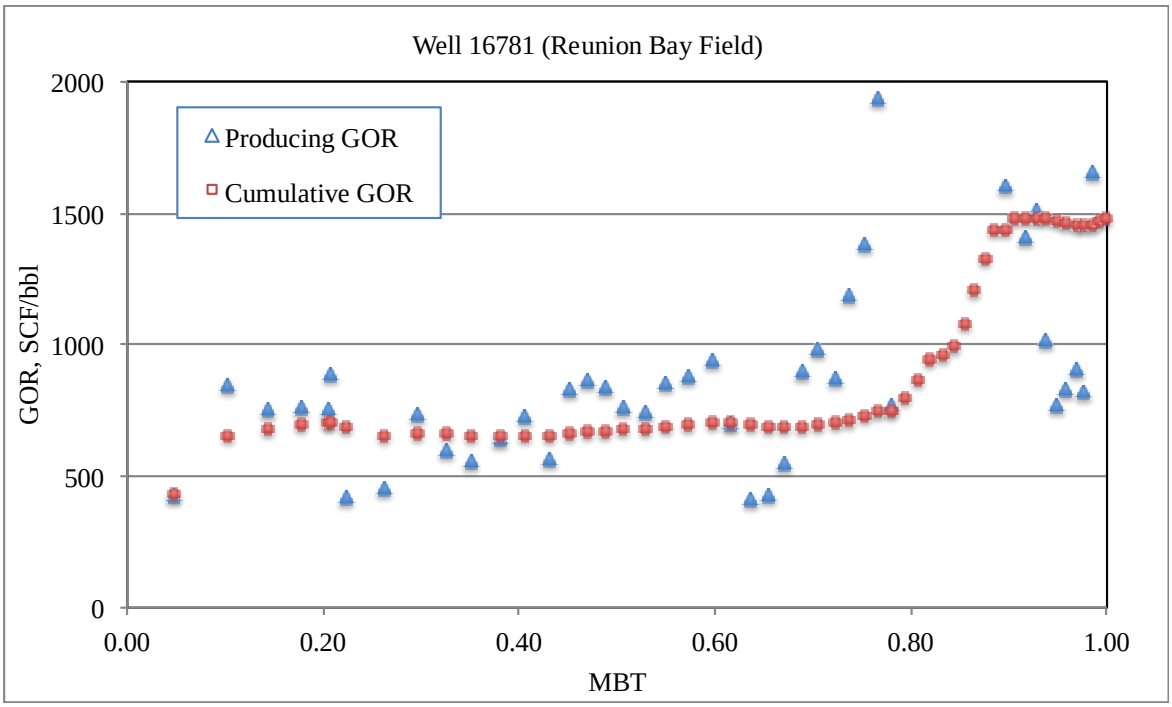

Figure A.1: Producing gas-oil ratio and cumulative gas-oil ratio plotted against the material balance time for well 16781.

APPENDIX B: ELKHORN RANCH FIELD CUMULATIVE GAS-OIL RATIO

The bubble chart in Section 3.3 uses the cumulative gas-oil ratio (CGOR) and the cumulative oil production for the forty-one wells in the Elkhorn Ranch Field. Table B.1, presents the calculated CGOR for the wells, along with their respective production life and the length of the horizontal-legs.

Table B.1: Calculation table for the Elkhorn Ranch CGOR bubble chart (Figure 3.12).

#	Well Number	Production Life	Cumulative Oil Production	Cumulative GOR	Horizontal Leg
		(Days)	(Bbls)	(SCF/Bbl)	(ft.)
1	6013	1083	62245	1.41	0
2	6158	4548	195196	1.13	0
3	7082	4039	206187	0.94	0
4	7690	8116	244403	0.69	0
5	7984	8373	60085	1.3175	0
6	8251	3597	41471	0.78	0
7	8465	2468	16330	2.04	0
8	8962	3474	44450	0.99	0
9	9122	3154	51585	1.24	0
10	11876	2749	199174	1.29	0
11	11877	1615	221430	3.37	2350
12	12072	8142	371953	3.39	2037
13	12297	2373	43882	0.89	1579
14	12511	5264	137444	0.71	2758
15	12599	6878	140271	3.48	3321
16	12632	6424	114458	3.05	2557
17	12712	6985	119955	3.11	2012
18	12727	1267	20667	0.33	2128
19	12736	1885	171049	3.98	2165
20	12766	1549	24229	0.75	2004
21	12774	5185	67702	1.06	2299
22	12776	2489	23401	0.41	2816
23	12814	5546	208269	1.68	2456
24	12829	6256	152348	0.60	7915
25	12886	7656	267909	4.85	3125
26	12908	7479	129624	2.99	2573
27	12939	4217	38304	5.00	2115
28	13112	6256	152348	0.60	3134
29	13123	896	15642	3.05	2776
30	13124	853	27942	5.06	2765
31	13194	7329	130216	1.99	1899

32	13219	7240	49773	33.47	2292
33	13256	7107	97207	13.33	2597
34	15088	3366	13076	0.69	0
35	16448	1408	88094	0.69	3757
36	17229	1356	69733	0.89	3217
37	19648	457	69656	1.11	8426
38	19687	495	111917	0.81	7764
39	19815	370	21806	1.53	9330
40	20174	375	12949	1.97	9890
41	20701	136	35500	1.27	9361

APPENDIX C: MATERIAL BALANCE CALCULATIONS

The following presents the overview of the material balance calculation in section 3.5, in which classical material balance equation for the solution gas drive recovery mechanism are used:

C.1 Stock Tank Original Oil in Place (STOOIP)

$$\text{STOOIP (N)} = A \cdot h \cdot \phi \cdot (1 - S_w)/B_{oi} \quad \text{(C.1)}$$

The following values were chosen for the parameters in equation B.1:

h: Formation thickness $= 35$ft

ϕ: Average porosity $= 0.1$, S_w: 0.75

(Source: Average value , ϕ: higher value to be in the safer side)

B_{oi}: Initial Oil formation volume factor $= 1.47$

(Source: PVT report for Bakken oil)

Figure C.1: Well drainage area determination: Broken line rectangles around solid black lines represents the Stimulated reservoir volume.

C.2 Material Balance Calculations:

Equations for solution drive recovery mechanism:

1. Above the bubble point pressure:

$$RF = N_p/N = \left(1 - \frac{B_{oi}}{B_o}\right) + \left(\frac{B_{oi}}{B_o}\right)\left(\frac{(c_w S_{wi} + c_f)}{(1 - S_{wi})}\right)\Delta P \qquad (C.2)$$

2. Below the bubble point (1529.6 psi, source PVT report for Elm coulee well):

$$RF = N_p/N = \frac{(B_t - B_{oi}) + B_{oi}((c_w S_{wi} + c_f)/(1 - S_{wi}))\Delta P}{[B_t + (R_p - R_{soi})B_g]} \qquad (C.3)$$

Where,

RF: recovery factor

N_p: Cummulative oil production at a specific time $'t'$

B_{oi}: Initial Oil formation volume factor

B_o: Oil formation volume factore at time $'t'$

c_w: Water compressibility

S_{wi}: Initial water saturation

c_f: Foramtion compressibility

ΔP: Reservoir pressure drop in time $'t'$

B_t: Total fluid formation volume factor

R_p: Producing Gas $-$ oil ratio

R_{soi}: Initial solution gas $-$ oil ratio

B_g: Gas formation volume factor

Table C.1: Correlation for the PVT properties (Source: PVT property report for Elm Coulee Well).

CONSTANT COMPOSITION EXPANSION @ 240.0 F (388.7 K)		
Relative Volume (V/Vsat)	(P >= Psat)	y=(-0.017347*x^2 + 1.739714*x + 1.304933)/(1.811100*x + 1.216402) R Squared = 0.984177
Relative Volume (V/Vsat)	(P <= Psat)	y=(1.899363*x^2 + -0.221361*x + 4.583522)/(6.367725*x + -0.114105) R Squared = 0.999995
DIFFERENTIAL LIBERATION @ 240.0 F (388.7 K)		
Live Oil Density (g/cc)	(P >= Psat)	y=(0.015384*x^2 + 1.450189*x + 0.952829)/(2.081195*x + 1.522568) R Squared = 0.999971
Live Oil Density (g/cc)	(P <= Psat)	y=(-0.689570*x^2 + 21.633931*x + 1.898937)/(31.616552*x + 2.429531) R Squared = 0.999549
Oil FVF [1]	(P >= Psat)	y=(-0.027485*x^2 + 2.741200*x + 2.019144)/(1.930680*x + 1.273208) R Squared = 0.999978
Oil FVF [1]	(P <= Psat)	y=(0.209886*x^2 + 1.841685*x + 0.117637)/(1.354998*x + 0.113014) R Squared = 0.999975
GOR (vol/vol)	(P <= Psat)	y=(37.093520*x^2 + 16.292673*x + -0.136693)/(0.468867*x + 0.051182) R Squared = 0.999947
Oil Viscosity (cp=mPa.s)	(P >= Psat)	y=(0.102655*x^2 + 1.789855*x + 0.000899)/(5.382371*x + 0.763366) R Squared = 0.985631
Oil Viscosity (cp=mPa.s)	(P <= Psat)	y=(0.061334*x^2 + 1.290868*x + 1.411355)/(6.659379*x + 2.209428) R Squared = 0.999734
y is the measured parameter and x = P/Psat, dimensionless		

Table C.2: Calculation table for well 16370.

P	Bo	Cw	Cf	R	Bg	RF
7000	1.406	3.0E-06	6.59E-06	344.82		0.00
6500	1.410	3.1E-06	6.59E-06	344.82		0.01
6000	1.415	3.1E-06	6.59E-06	344.82		0.01
5500	1.419	3.1E-06	6.59E-06	344.82		0.01
5000	1.424	3.2E-06	6.59E-06	344.82		0.02
4500	1.430	3.2E-06	6.59E-06	344.82		0.02
4000	1.435	3.2E-06	6.59E-06	344.82		0.03
3500	1.442	3.3E-06	6.59E-06	344.82		0.03
3000	1.449	3.3E-06	6.59E-06	344.82		0.03
2500	1.458	3.4E-06	6.59E-06	344.82		0.04
2000	1.469	3.4E-06	6.59E-06	344.82		0.05
1564	1.480	3.4E-06	6.59E-06	344.82	0.0023	0.06
1529.6	1.474	3.4E-06	6.59E-06	340.29	0.0023	0.06
1429	1.462	3.4E-06	6.59E-06	326.92	0.0025	0.07
1345	1.452	3.5E-06	6.59E-06	315.65	0.0026	0.08
1160	1.430	3.5E-06	6.59E-06	290.31	0.0030	0.10
860	1.391	3.5E-06	6.59E-06	246.96	0.0041	0.15
590	1.349	3.5E-06	6.59E-06	203.17	0.0060	0.20

APPENDIX D: SINGLE PHASE SIMULATION FORMULATION

The mathematical formulation of the FORTRAN code for the section 3.6 is derived in the following sections:

D.1 For the Middle Layer

Diffusivity-equation for the fracture network:

$$\nabla \cdot \frac{k_{f,eff}}{\mu} \nabla p_f - \tau + q_f = (\emptyset c_t)_f \frac{\partial p_f}{\partial t} \tag{D.1}$$

Equation for the Transfer term, matrix to fracture fluid transfer, Advective flow (Darcy type):

$$\tau = \sigma \frac{k_m}{\mu} (p_f - p_m) = (\emptyset c_t)_m \frac{\partial p_m}{\partial t} \tag{D.2}$$

Rate-term represented in terms of Well Index, well flow-in pressure and well-containing grid-block pressure:

$$q_{f_i} = -WI\left(P_{f_i} - P_{w_i}\right) \tag{D.3}$$

Expression for the Well Index:

$$WI = \left(\frac{k_f \emptyset_f}{\mu}\right)(2\pi)\Delta z \frac{1}{\ln\frac{r_b}{r_w} + S} \tag{D.4}$$

Here, a scheme for 1-D finite difference discretization in x-axis will be proposed. The same concept could be applied to add y and z-dimensions.

Discretising equation D.2 gives:

$$\sigma \frac{k_m}{\mu}\left(P_{f_i}^{n+1} - P_{m_i}^{n+1}\right) = (\emptyset c_t)_m \left(\frac{P_{m_i}^{n+1} - P_{m_i}^{n}}{\Delta t}\right)$$

Or,

$$\sigma \frac{\Delta t \cdot k_m}{\mu \cdot (\emptyset c_t)_m}\left(P_{f_i}^{n+1} - P_{m_i}^{n+1}\right) = P_{m_i}^{n+1} - P_{m_i}^{n}$$

Or,

$$-\sigma \frac{\Delta t \cdot k_m}{\mu \cdot (\emptyset c_t)_m} P_{m_i}^{n+1} - P_{m_i}^{n+1} = -\sigma \frac{\Delta t \cdot k_m}{\mu \cdot (\emptyset c_t)_m} P_{f_i}^{n+1} - P_{m_i}^{n}$$

Or,

$$\left(\sigma \frac{\Delta t \cdot k_m}{\mu \cdot (\emptyset c_t)_m} + 1\right) P_{m_i}^{n+1} = \sigma \frac{\Delta t \cdot k_m}{\mu \cdot (\emptyset c_t)_m} P_{f_i}^{n+1} + P_{m_i}^{n}$$

Or,

$$P_{m_i}^{n+1} = \left(\sigma \frac{\Delta t \cdot k_m}{\mu \cdot (\emptyset c_t)_m} P_{f_i}^{n+1} + P_{m_i}^{n}\right) \Big/ \left(\sigma \frac{\Delta t \cdot k_m}{\mu \cdot (\emptyset c_t)_m} + 1\right) \tag{D.5}$$

Substituting the value of τ from equation D.2 into D.1 and discretizing it gives:

$$\left(T_{x_f}\right)_{i+\frac{1}{2}}\left(P_{f_{i+1}}^{n+1}-P_{f_i}^{n+1}\right)-\left(T_{x_f}\right)_{i-\frac{1}{2}}\left(P_{f_i}^{n+1}-P_{f_{i-1}}^{n+1}\right)-\sigma V_i\left(\frac{k_m}{\mu}\right)_i\left(P_{f_i}^{n+1}-P_{m_i}^{n+1}\right)$$
$$+q_{f_i}=(\emptyset c_t)_f V_i\left(\frac{P_{f_i}^{n+1}-P_{f_i}^{n}}{\Delta t}\right)$$

Substituting the value of $P_{m_i}^{n+1}$ from equation D.5 it gives:

$$\left(T_{x_f}\right)_{i+\frac{1}{2}}\left(P_{f_{i+1}}^{n+1}-P_{f_i}^{n+1}\right)-\left(T_{x_f}\right)_{i-\frac{1}{2}}\left(P_{f_i}^{n+1}-P_{f_{i-1}}^{n+1}\right)$$
$$-\sigma V_i\left(\frac{k_m}{\mu}\right)_i\left(P_{f_i}^{n+1}-\frac{\sigma\frac{\Delta t\cdot k_m}{\mu\cdot(\emptyset c_t)_m}P_{f_i}^{n+1}+P_{m_i}^{n}}{\left(\sigma\frac{\Delta t\cdot k_m}{\mu\cdot(\emptyset c_t)_m}+1\right)}\right)+q_{f_i}$$
$$=(\emptyset c_t)_f V_i\left(\frac{P_{f_i}^{n+1}-P_{f_i}^{n}}{\Delta t}\right)$$

Or,

$$\left(T_{x_f}\right)_{i+\frac{1}{2}}\left(P_{f_{i+1}}^{n+1}-P_{f_i}^{n+1}\right)-\left(T_{x_f}\right)_{i-\frac{1}{2}}\left(P_{f_i}^{n+1}-P_{f_{i-1}}^{n+1}\right)$$
$$-\sigma V_i\left(\frac{k_m}{\mu}\right)_i\left(\frac{P_{f_i}^{n+1}\left(\sigma\frac{\Delta t\cdot k_m}{\mu\cdot(\emptyset c_t)_m}+1\right)-\sigma\frac{\Delta t\cdot k_m}{\mu\cdot(\emptyset c_t)_m}P_{f_i}^{n+1}-P_{m_i}^{n}}{\left(\sigma\frac{\Delta t\cdot k_m}{\mu\cdot(\emptyset c_t)_m}+1\right)}\right)+q_{f_i}$$
$$=(\emptyset c_t)_f V_i\left(\frac{P_{f_i}^{n+1}-P_{f_i}^{n}}{\Delta t}\right)$$

Or,

$$\left(T_{x_f}\right)_{i+\frac{1}{2}}\left(P_{f_{i+1}}^{n+1}-P_{f_i}^{n+1}\right)-\left(T_{x_f}\right)_{i-\frac{1}{2}}\left(P_{f_i}^{n+1}-P_{f_{i-1}}^{n+1}\right)$$
$$-\sigma V_i\left(\frac{k_m}{\mu}\right)_i\left(\frac{P_{f_i}^{n+1}\sigma\frac{\Delta t\cdot k_m}{\mu\cdot(\emptyset c_t)_m}+P_{f_i}^{n+1}-\sigma\frac{\Delta t\cdot k_m}{\mu\cdot(\emptyset c_t)_m}P_{f_i}^{n+1}-P_{m_i}^{n}}{\left(\sigma\frac{\Delta t\cdot k_m}{\mu\cdot(\emptyset c_t)_m}+1\right)}\right)+q_{f_i}$$
$$=(\emptyset c_t)_f V_i\left(\frac{P_{f_i}^{n+1}-P_{f_i}^{n}}{\Delta t}\right)$$

Or,

$$\left(T_{x_f}\right)_{i+\frac{1}{2}}\left(P_{f_{i+1}}^{n+1}-P_{f_i}^{n+1}\right)-\left(T_{x_f}\right)_{i-\frac{1}{2}}\left(P_{f_i}^{n+1}-P_{f_{i-1}}^{n+1}\right)$$
$$-\sigma V_i\left(\frac{k_m}{\mu}\right)_i\left(\frac{P_{f_i}^{n+1}-P_{m_i}^{n}}{\sigma\frac{\Delta t\cdot k_m}{\mu\cdot(\emptyset c_t)_m}+1}\right)+q_{f_i}=(\emptyset c_t)_f V_i\left(\frac{P_{f_i}^{n+1}-P_{f_i}^{n}}{\Delta t}\right)$$

Substituting the value of q_{f_i} from equation D.3 to get:

$$\left(T_{x_f}\right)_{i+\frac{1}{2}} P_{f_{i+1}}^{n+1} - \left(T_{x_f}\right)_{i+\frac{1}{2}} P_{f_i}^{n+1} - \left(T_{x_f}\right)_{i-\frac{1}{2}} P_{f_i}^{n+1} + \left(T_{x_f}\right)_{i-\frac{1}{2}} P_{f_{i-1}}^{n+1} - \sigma V_i \left(\frac{k_m}{\mu}\right)_i \frac{P_{f_i}^{n+1}}{\sigma \frac{\Delta t \cdot k_m}{\mu \cdot (\emptyset c_t)_m} + 1} + \sigma V_i \left(\frac{k_m}{\mu}\right)_i \frac{P_{m_i}^{n}}{\sigma \frac{\Delta t \cdot k_m}{\mu \cdot (\emptyset c_t)_m} + 1} - WI\left(P_{f_i} - P_{well_i}\right) = \frac{(\emptyset c_t)_f V_i}{\Delta t} P_{f_i}^{n+1} - \frac{(\emptyset c_t)_f V_i}{\Delta t} P_{f_i}^{n}$$

Or,

$$\left(T_{x_f}\right)_{i+\frac{1}{2}} P_{f_{i+1}}^{n+1} - \left(T_{x_f}\right)_{i+\frac{1}{2}} P_{f_i}^{n+1} - \left(T_{x_f}\right)_{i-\frac{1}{2}} P_{f_i}^{n+1} + \left(T_{x_f}\right)_{i-\frac{1}{2}} P_{f_{i-1}}^{n+1} - P_{f_i}^{n+1} \frac{\sigma V_i \left(\frac{k_m}{\mu}\right)_i}{\sigma \frac{\Delta t \cdot k_m}{\mu \cdot (\emptyset c_t)_m} + 1} - \frac{(\emptyset c_t)_f V_i}{\Delta t} P_{f_i}^{n+1} - WIP_{f_i} = -\frac{(\emptyset c_t)_f V_i}{\Delta t} P_{f_i}^{n} - P_{m_i}^{n} \frac{\sigma V_i \left(\frac{k_m}{\mu}\right)_i}{\sigma \frac{\Delta t \cdot k_m}{\mu \cdot (\emptyset c_t)_m} + 1} - WIP_{well_i}$$

Or,

$$\left(T_{x_f}\right)_{i-\frac{1}{2}} P_{f_{i-1}}^{n+1} - \left(\left(T_{x_f}\right)_{i+\frac{1}{2}} + \left(T_{x_f}\right)_{i-\frac{1}{2}} + \frac{\sigma V_i \left(\frac{k_m}{\mu}\right)_i}{\sigma \frac{\Delta t \cdot k_m}{\mu \cdot (\emptyset c_t)_m} + 1} + WI + \frac{(\emptyset c_t)_f V_i}{\Delta t} \right) P_{f_i}^{n+1} + \left(T_{x_f}\right)_{i+\frac{1}{2}} P_{f_{i+1}}^{n+1} = -\left(\frac{(\emptyset c_t)_f V_i}{\Delta t} P_{f_i}^{n} + P_{m_i}^{n} \frac{\sigma V_i \left(\frac{k_m}{\mu}\right)_i}{\sigma \frac{\Delta t \cdot k_m}{\mu \cdot (\emptyset c_t)_m} + 1} + WIP_{well_i} \right)$$

Which is essentially the generalized equation for the solution matrix and can be written in the following format:

$$D_i P_{f_{i-1}}^{n+1} + E_i P_{f_i}^{n+1} + F_i P_{f_{i+1}}^{n+1} = R_i$$

Where,

$$D_i = \left(T_{x_f}\right)_{i-\frac{1}{2}}$$

$$E_i = -\left(\left(T_{x_f}\right)_{i+\frac{1}{2}} + \left(T_{x_f}\right)_{i-\frac{1}{2}} + \frac{\sigma V_i \left(\frac{k_m}{\mu}\right)_i}{\sigma \frac{\Delta t \cdot k_m}{\mu \cdot (\emptyset c_t)_m} + 1} + WI + \frac{(\emptyset c_t)_f V_i}{\Delta t} \right)$$

$$F_i = \left(T_{x_f}\right)_{i+\frac{1}{2}}$$

$$R_i = -\left(\frac{(\emptyset c_t)_f V_i}{\Delta t} P_{f_i}^n + P_{m_i}^n \frac{\sigma V_i \left(\frac{k_m}{\mu}\right)_i}{\sigma \frac{\Delta t \cdot k_m}{\mu \cdot (\emptyset c_t)_m} + 1} + WIP_{well_i} \right)$$

D.2 For the U&L Shale Layers

Diffusivity-equation for the fracture network

$$\nabla \cdot \frac{k_{f,eff}}{\mu} \nabla p_{gf} - \tau + q_f = (\emptyset c_t)_f \frac{\partial p_{gf}}{\partial t} \tag{D.6}$$

Equation for the Transfer term, matrix to fracture fluid transfer, Convective flow (Diffusive type)

$$\tau = \sigma D_{m,eff}\left(C_{ve}(p_{gf}) - C_{vm}\right) B_g(p_{gf}) \rho_s = \frac{\partial C_{vm}}{\partial t} \tag{D.7}$$

Rate term for the well-containing grid block

$$\hat{q}_g = q_g B_g(p_{gf}) \delta(\vec{x} - \vec{x}_o) \tag{D.8}$$

Langmuir isotherm equation

$$C_{ve}(p_{gf}) = C_{ve,max} {bp_{gf}}/{(1 + bp_{gf})} \tag{D.9}$$

Expression for the effective diffusion co-efficient

$$D_{m,eff} = D_{m,} {\emptyset}/{\tau} \tag{D.10}$$

Discretising equation D.7 gives

$$\sigma D_{m,eff}\left(C_{ve}\left(P_{gf_i}^{n+1}\right) - C_{vm,i}^{n+1}\right) = \left(\frac{C_{vm,i}^{n+1} - C_{vm,i}^n}{\Delta t}\right)$$

Or,

$$\sigma D_{m,eff} \Delta t \left(C_{ve}\left(P_{gf_i}^{n+1}\right) - C_{vm,i}^{n+1}\right) = C_{vm,i}^{n+1} - C_{vm,i}^n$$

Or,

$$\sigma D_{m,eff} \Delta t C_{vm,i}^{n+1} + C_{vm,i}^{n+1} = \sigma D_{m,eff} \Delta t C_{ve}\left(P_{gf_i}^{n+1}\right) + C_{vm,i}^n$$

Or,

$$\left(\sigma D_{m,eff} \Delta t + 1\right) C_{vm,i}^{n+1} = \sigma D_{m,eff} \Delta t C_{ve}\left(P_{gf_i}^{n+1}\right) + C_{vm,i}^n$$

Or,

$$C_{vm,i}^{n+1} = {\left\{\sigma D_{m,eff} \Delta t C_{ve}\left(P_{gf_i}^{n+1}\right) + C_{vm,i}^n\right\}}/{\left(\sigma D_{m,eff} \Delta t + 1\right)} \tag{D.11}$$

Substituting the value of τ from equation D.7 into D.6 and discretizing it gives

$$\begin{aligned} &\left(T_{x_f}\right)_{i+\frac{1}{2}}\left(P_{gf_{i+1}}^{n+1} - P_{gf_i}^{n+1}\right) - \left(T_{x_f}\right)_{i-\frac{1}{2}}\left(P_{gf_i}^{n+1} - P_{gf_{i-1}}^{n+1}\right) \\ &\quad - \sigma V_i D_{m,eff}\left(C_{ve}\left(P_{gf_i}^{n+1}\right) - C_{vm,i}^{n+1}\right) B_g\left(P_{gf_i}^n\right) \rho_s + q_{g_i} \\ &\quad = (\emptyset c_t)_f V_i \left(\frac{P_{gf_i}^{n+1} - P_{gf_i}^n}{\Delta t}\right) \end{aligned}$$

Substituting the value of $C_{m_i}^{n+1}$ from equation D.11 to get:

$$\left(T_{x_f}\right)_{i+\frac{1}{2}}\left(P_{gf_{i+1}}^{n+1}-P_{gf_i}^{n+1}\right)-\left(T_{x_f}\right)_{i-\frac{1}{2}}\left(P_{gf_i}^{n+1}-P_{gf_{i-1}}^{n+1}\right)$$
$$-\sigma V_i D_{m,eff} B_g\left(P_{gf_i}^{n}\right)\rho_s\left(C_{ve}\left(P_{gf_i}^{n+1}\right)-\frac{\sigma D_{m,eff}\Delta t C_{ve}\left(P_{gf_i}^{n+1}\right)+C_{vm,i}^{n}}{\left(\sigma D_{m,eff}\Delta t+1\right)}\right)+q_{gf_i}=(\emptyset c_t)_f V_i\left(\frac{P_{gf_i}^{n+1}-P_{gf_i}^{n}}{\Delta t}\right)$$

Or,

$$\left(T_{x_f}\right)_{i+\frac{1}{2}}\left(T_{x_f}\right)_{i+\frac{1}{2}}\left(P_{gf_{i+1}}^{n+1}-P_{gf_i}^{n+1}\right)-\left(T_{x_f}\right)_{i-\frac{1}{2}}\left(P_{gf_i}^{n+1}-P_{gf_{i-1}}^{n+1}\right)$$
$$-\sigma V_i D_{m,eff} B_g\left(P_{gf_i}^{n}\right)\rho_s\left(\frac{C_{ve}\left(P_{gf_i}^{n+1}\right)\left(\sigma D_{m,eff}\Delta t+1\right)-\sigma D_{m,eff}\Delta t C_{ve}\left(P_{gf_i}^{n+1}\right)-C_{vm,i}^{n}}{\left(\sigma D_{m,eff}\Delta t+1\right)}\right)$$
$$+q_{g,i}B_g\left(P_{gf_i}^{n}\right)=(\emptyset c_t)_f V_i\left(\frac{P_{gf_i}^{n+1}-P_{gf_i}^{n}}{\Delta t}\right)$$

Or,

$$\left(T_{x_f}\right)_{i+\frac{1}{2}}\left(P_{gf_{i+1}}^{n+1}-P_{gf_i}^{n+1}\right)-\left(T_{x_f}\right)_{i-\frac{1}{2}}\left(P_{gf_i}^{n+1}-P_{gf_{i-1}}^{n+1}\right)$$
$$-\sigma V_i D_{m,eff} B_g\left(P_{gf_i}^{n}\right)\rho_s\left(\frac{C_{ve}\left(P_{gf_i}^{n+1}\right)-C_{vm,i}^{n}}{\left(\sigma D_{m,eff}\Delta t+1\right)}\right)+q_{g,i}B_g\left(P_{gf_i}^{n}\right)$$
$$=(\emptyset c_t)_f V_i\left(\frac{P_{gf_i}^{n+1}-P_{gf_i}^{n}}{\Delta t}\right)$$

(D.12)

For Newton Rhapson Iteration, we define

$$P_{gf}^{n+1}\approx P_{gf}^{l+1}=P_{gf}^{l}+\partial P_{gf}^{l}$$

And

$$C_{ve}\left(P_{gf}^{n+1}\right)\approx C_{ve}\left(P_{gf}^{l+1}\right)=C_{ve}\left(P_{gf}^{l}\right)+\left[\frac{\partial C_{ve}\left(P_{gf}\right)}{\partial P_{gf}}\right]^{l}\partial P_{gf}^{l}$$

Therefore, from Eq. D.12:

$$\left(T_{x_f}\right)_{i+\frac{1}{2}}\left(P_{gf_{i+1}}^{l+1}-P_{gf_i}^{l+1}\right)-\left(T_{x_f}\right)_{i-\frac{1}{2}}\left(P_{gf_i}^{l+1}-P_{gf_{i-1}}^{l+1}\right)$$
$$-\sigma V_i D_{m,eff} B_g\left(P_{gf_i}^{l}\right)\rho_s\left(\frac{C_{ve}\left(P_{gf_i}^{l+1}\right)-C_{vm,i}^{l}}{\left(\sigma D_{m,eff}\Delta t+1\right)}\right)+q_{g,i}B_g\left(P_{gf_i}^{l}\right)$$
$$=(\emptyset c_t)_f V_i\left(\frac{P_{gf_i}^{l+1}-P_{gf_i}^{n}}{\Delta t}\right)$$

Or,

$$\left(T_{x_f}\right)_{i+\frac{1}{2}}\left(P^{l}_{gf_{i+1}}+\partial P^{l}_{gf_{i+1}}-P^{l}_{gf_i}-\partial P^{l}_{gf_i}\right)-\left(T_{x_f}\right)_{i-\frac{1}{2}}\left(P^{l}_{gf_i}+\partial P^{l}_{gf_i}-P^{l}_{gf_{i-1}}-\partial P^{l}_{gf_{i-1}}\right)$$
$$-\sigma V_i D_{m,eff} B_g\left(P^{l}_{gf_i}\right)\rho_s\left(\frac{C_{ve}\left(P^{l}_{gf,i}\right)+\left[\frac{\partial C_{ve}\left(P_{gf}\right)}{\partial P_{gf}}\right]^{l}\partial P^{l}_{gf_i}-C^{l}_{vm,i}}{\left(\sigma D_{m,eff}\Delta t+1\right)}\right)$$
$$+q_{g,i}B_g\left(P^{l}_{gf_i}\right)=\left(\emptyset c_t\right)_f V_i\left(\frac{P^{l}_{gf_i}+\partial P^{l}_{gf_i}-P^{n}_{gf_i}}{\Delta t}\right)$$

Or,

$$\left(T_{x_f}\right)_{i+\frac{1}{2}}\left(\partial P^{l}_{gf_{i+1}}-\partial P^{l}_{gf_i}\right)-\left(T_{x_f}\right)_{i-\frac{1}{2}}\left(\partial P^{l}_{gf_i}-\partial P^{l}_{gf_{i-1}}\right)$$
$$-\sigma V_i D_{m,eff} B_g\left(P^{l}_{gf_i}\right)\rho_s\left(\frac{\left[\frac{\partial C_{ve}\left(P_{gf}\right)}{\partial P_{gf}}\right]^{l}}{\sigma D_{m,eff}\Delta t+1}\right)\partial P^{l}_{gf_i}-\frac{\left(\emptyset c_t\right)_f V_i}{\Delta t}\partial P^{l}_{gf_i}$$
$$=-\left(T_{x_f}\right)_{i+\frac{1}{2}}\left(P^{l}_{gf_{i+1}}-P^{l}_{gf_i}\right)+\left(T_{x_f}\right)_{i-\frac{1}{2}}\left(P^{l}_{gf_i}-P^{l}_{gf_{i-1}}\right)$$
$$+\sigma V_i D_{m,eff} B_g\left(P^{l}_{gf_i}\right)\rho_s\left(\frac{C_{ve}\left(P^{l}_{gf,i}\right)-C^{l}_{vm,i}}{\left(\sigma D_{m,eff}\Delta t+1\right)}\right)-q_{g,i}B_g\left(P^{l}_{gf_i}\right)$$
$$+\left(\emptyset c_t\right)_f V_i\left(\frac{P^{l}_{gf_i}+\partial P^{l}_{gf_i}-P^{n}_{gf_i}}{\Delta t}\right)$$

Or,

$$\left(T_{x_f}\right)_{i+\frac{1}{2}}\partial P^{l}_{gf_{i+1}} + \left(T_{x_f}\right)_{i-\frac{1}{2}}\partial P^{l}_{gf_{i-1}}$$
$$-\left[\left(T_{x_f}\right)_{i+\frac{1}{2}} + \left(T_{x_f}\right)_{i-\frac{1}{2}} + \sigma V_i D_{m,eff} B_g\left(P^{l}_{gf_i}\right)\rho_s\left(\frac{\left[\frac{\partial C_{ve}\left(P_{gf}\right)}{\partial P_{gf}}\right]^{l}}{\sigma D_{m,eff}\Delta t + 1}\right)\right.$$
$$\left. + \frac{(\emptyset c_t)_f V_i}{\Delta t}\right]\partial P^{l}_{gf_i}$$
$$= -\left(T_{x_f}\right)_{i+\frac{1}{2}}\left(P^{l}_{gf_{i+1}} - P^{l}_{gf_i}\right) + \left(T_{x_f}\right)_{i-\frac{1}{2}}\left(P^{l}_{gf_i} - P^{l}_{gf_{i-1}}\right)$$
$$+ \sigma V_i D_{m,eff} B_g\left(P^{l}_{gf_i}\right)\rho_s\left(\frac{C_{ve}\left(P^{l}_{gf,i}\right) - C^{l}_{vm,i}}{\left(\sigma D_{m,eff}\Delta t + 1\right)}\right) - q_{g,i} B_g\left(P^{l}_{gf_i}\right)$$
$$+ (\emptyset c_t)_f V_i\left(\frac{P^{l}_{gf_i} + \partial P^{l}_{gf_i} - P^{n}_{gf_i}}{\Delta t}\right)$$

Which is essentially the generalized equation for the solution matrix and can be written in the following format:

$$D_i P^{n+1}_{f_{i-1}} + E_i P^{n+1}_{f_i} + F_i P^{n+1}_{f_{i+1}} = R_i$$

Where,

$$D_i = \left(T_{x_f}\right)_{i-\frac{1}{2}}$$

$$E_i = -\left[\left(T_{x_f}\right)_{i+\frac{1}{2}} + \left(T_{x_f}\right)_{i-\frac{1}{2}} + \sigma V_i D_{m,eff} B_g\left(P^{l}_{gf_i}\right)\rho_s\left(\frac{\left[\frac{\partial C_{ve}\left(P_{gf}\right)}{\partial P_{gf}}\right]^{l}}{\sigma D_{m,eff}\Delta t + 1}\right) + \frac{(\emptyset c_t)_f V_i}{\Delta t}\right]$$

$$F_i = \left(T_{x_f}\right)_{i+\frac{1}{2}}$$

$$R_i = \left(P^{l}_{gf_{i+1}} - P^{l}_{gf_i}\right) + \left(T_{x_f}\right)_{i-\frac{1}{2}}\left(P^{l}_{gf_i} - P^{l}_{gf_{i-1}}\right) + \sigma V_i D_{m,eff} B_g\left(P^{l}_{gf_i}\right)\rho_s\left(\frac{C_{ve}\left(P^{l}_{gf,i}\right) - C^{l}_{vm,i}}{\left(\sigma D_{m,eff}\Delta t + 1\right)}\right)$$
$$- q_{g,i} B_g\left(P^{l}_{gf_i}\right) + (\emptyset c_t)_f V_i\left(\frac{P^{l}_{gf_i} + \partial P^{l}_{gf_i} - P^{n}_{gf_i}}{\Delta t}\right)$$

Nomenclature**:**

k: permeability

μ: viscosity

p: pressure

τ: matrix − to − fracture fluid transfer fuction

q: production rate

∅: porosity

c: Total comressibilty

t: time

σ: Shape factor

WI: Well index

Δ: increment

z: z − axis lenght

r: radius

S: skin

T: fluid transmisivity of the grid face

V: Grid volume ($\Delta X \cdot \Delta Y \cdot \Delta Z$)

D, E, F, R: Msolution atrix elements

D: Diffusivity Coefficient

C: Molecular concentration

B: Formation fluid volume factor

ρ: Density

b: Langmuir Isotherm constant

Subscript**:**

f: fracture

eff: effective

t: total

m: matrix

i: x − axis index for gridding

w: well bottom hole

b: well drainage boundary

w: well

g: gas phase

ve: equilibrium concentation fracture

vm: equilibrium concentration matrix

S: Solid (Rock)

max: Langmuir′s maximum adsorption concetration

Newton − Rhapson Iteration Index

Superscript**:**

n: time discetization index

APPENDIX E

DUAL POROSITY FORMULATION IN GEM™

The GEM™ manual list the following formulations to model a dual-porosity media in the naturally fractured reservoirs. The governing equations are an extension of the single-porosity equations described by Nghiem and Li (1988). The representation of the matrix-to-fracture flow follows Kazemi et al (1976). The fractures are assumed orthogonal in the three directions and acts as boundaries to matrix elements.

E.1 Flow Equations

For hydrocarbon components matrix-to-fracture fluid transfer:

$$-\tau_{iomf} - \frac{V}{\Delta t}(N_i^{n+1} - N_i^n)_m = 0 \qquad i = 1, \cdots, n_c \tag{E.1}$$

For water phase components matrix-to-fracture fluid transfer:

$$-\tau_{wmf} - \frac{V}{\Delta t}\left(N_{n_c+1}^{n+1} - N_{n_c+1}^n\right)_m = 0 \tag{E.2}$$

Mass-balance in the matrix-blocks:

$$\sum_{i=1}^{n_c+1} N_{im}^{n+1} - \emptyset_m^{n+1}\left(\rho_o S_o + \rho_g S_g + \rho_w S_w\right)_m^{n+!} = 0 \tag{E.3}$$

Dual Porosity Formulation - Fracture Blocks:

$$\Delta T_{of}^S y_{iof}^S (\Delta p^{n+1} - \gamma_o^S \Delta D)_f + \Delta T_{gf}^S y_{igf}^S \left(\Delta p^{n+1} + \Delta p_{cog}^S - \gamma_g^S \Delta D\right)_f + q_i^{n+1} + \tau_{iomf} + \tau_{igmf} - \frac{V}{\Delta t}(N_i^{n+1} - N_i^n)_f = 0, \qquad i = 1, \cdots, n_c \tag{E.4}$$

$$\Delta T_{wf}^S (\Delta p^{n+1} - \Delta p_{cwo}^S - \gamma_w^S \Delta D)_f + q_w^{n+1} + \tau_{wmf} - \frac{V}{\Delta t}\left(N_{n_c+1}^{n+1} - N_{n_c+1}^n\right)_f = 0, \qquad i = 1, \cdots, n_c \tag{E.5}$$

$$\sum_{i=1}^{n_c+1} N_{if}^{n+1} - \emptyset_f^{n+1}\left(\rho_o S_o + \rho_g S_g + \rho_w S_w\right)_f^{n+!} = 0 \tag{E.6}$$

Where Ni, i = 1...nc +1 are the moles of i per unit of gridblock volume. The subscript i with i = 1...nc corresponds to the hydrocarbon components and the subscript nc+1 denotes the water component. Terms τ_{iomf} and τ_{igmf} are the matrix-fracture transfer in the oil and gas phases for component i, and τ_{wmf} is the matrix-fracture transfer for water. The superscripts n and n+1

denote respectively the old and current time level and the superscript s refers to n for explicit blocks and to n+1 for implicit blocks. The subscript f and m correspond to the fracture and matrix respectively.

E.2 Phase-Equilibrium Equations or flash calculations:

If the hydrocarbon system is in the two-phase region at a given p, T and N_i (i=1… n_c), the phase compositions and splits can be obtained by solving the thermodynamic-equilibrium equation:

$$\ln f_{ig} - \ln f_{io} = 0 \qquad i = 1 \cdots, nc \tag{E.7}$$

For N_{ig}, the moles of Component i in the gas phase. The moles of Component 'i' in the oil phase, N_{io}, can be obtained from:

$$N_{io} = N_i - N_{ig} \qquad i = 1 \cdots, nc \tag{E.8}$$

E.3 Saturation Equation

The saturations are related to Ni and m (m = o, g, w) through the following equation:

$$S_w = N_{n_c+1}/(\Phi \rho_w)$$

$$S_o = (1 - S_w)\frac{N_o/\rho_o}{N_o/\rho_o + N_g/\rho_g}$$

$$S_o = (1 - S_w - S_o) \tag{E.9}$$